DEVELOPMENT OF A THERMO-CHEMICAL MOVING BED REDUCTION REACTOR FOR CHARGING A PELLETIZED MATERIAL CAPABLE OF SHORT- AND LONG-TERM ENERGY STORAGE

By

Philipp Schimmels

A DISSERTATION

Submitted to
Michigan State University
in partial fulfillment of the requirements
for the degree of

Mechanical Engineering—Doctor of Philosophy

2024

ABSTRACT

Large-scale storage of renewable energy is necessary to increase reliability of this intermittently, but abundantly available resource. Of special concern is the storage of energy and its subsequent use in industrial processes requiring high temperature heat. A promising emerging technology is based on using redox reactions of metal oxides at high temperatures. The shelf-stable redox material MgMnO was identified as a potential candidate due to its high energy density, cyclic stability, high reaction temperature and good scalability. This work describes the conception, design, manufacturing, testing and improvement of a solid fuel reduction reactor used to charge the energy storage material MgMnO. The reactor enables continuous charging of the pelletized material via a packed bed moving through a 1500°C furnace. A counter-currently flowing sweep gas is used to separate the released oxygen from the charged material to prevent re-oxidation. It also acts as a heat recuperation carrier that cools charged particles and pre-heats particles before entering the reaction zone. This approach enables high thermal efficiency as the sensible heat is almost entirely recovered. A lab-scale reactor was built and tested successfully. Challenges such as particle flowability at high temperatures, fluidization of the bed, and low extent of reaction were encountered and solved by managing the counter-flowing gas and increasing the residence time of the particles in the reactor. The reactor output reached a maximum of 2500 W of charged chemical potential. Several models were developed and used to design experiments and validate the performance of the system. High energetic cost for separation of oxygen and sweep gas nitrogen was identified as a roadblock to improved efficiencies and potential scale-up of the system. This led to mathematical and experimental investigation of using water vapor as alternative sweep gas. Results show that water vapor is superior to nitrogen as a reducing agent and has a lower energetic cost of production. The proposed reactor can be scaled up and results of this study indicates that using the pelletized MgMnO pelletized material offers thermo-chemical energy storage at low-cost. The extraction of this energy at high temperature offers a path toward the decarbonization of a variety of industrial processes that are currently relying on the combustion of hydrocarbon fuels for high-grade heat.

Ut in omnibus glorificetur Deus

ACKNOWLEDGEMENTS

This work is the culmination of my academic efforts. While I feel proud of this accomplishment, I have recognized the tremendous impact of those that walked alongside me during my entire academic career. I have reflected deeply on your impact and want to thank those individual that have had profound impacts on my life and career.

- Dr. Benard, my final primary advisor and chair of my dissertation committee: We got to work together in my 4^{th} year at MSU after my previous advisor left the university. I am tremendously grateful for your capacity to quickly recognize where I was in my journey and what areas still had a growth-potential. I have learned and grown so much during this time of working together. Thank you for frequently making time in your busy schedule and for helping me recognize and overcome many challenges.

- Dr. Klausner, my first MSU advisor: Our meeting during my first semester of graduate school has put my academic life on the path that lead to this dissertation. Your trust in my abilities that led to my hiring onto the SoFuel project caused a change of plans from getting a Master's degree to pursuing my PhD while working on the cutting edge of renewable energy storage research. Thank you for trusting and challenging me with the responsibilities you gave me with this project and thank you for serving on my PhD committee.

- Dr. Randhir, lab supervisor and mentor: Without your help and support, I would not have been able to grow and learn this much during the time we worked together. Your innovative problem solving skills motivated me to find new solutions to the challenges I faced.

- Dr. Petrasch, my temporary advisor: I am grateful for your commitment to supporting me during my studies. I learned a lot from our interactions about project and time management, innovative problem solving and leadership.

- Dr. Engeda and Dr. Jaberi, my committee members: Thank you for serving on my committee, giving me helpful feedback and support during the development and defense of this work.

- Dr. Kaufmann, my undergrad advisor: You helped ignite my passion for scientific work through challenging me to go beyond the average undergraduate experience. The foundation I received with your help gave me the confidence and knowledge to tackle this PhD program.

- Michael Hayes, my lab-mate: Your work-ethic and kindness has been inspiring. I have grown so much as a student but also as a colleague thanks to your optimistic and friendly attitude and your ideas, comments, and feedback on my work have always been super helpful.

- Reishma Mathews, my wife: Your patience, love and support have been crucial. You helped me to keep the bigger picture in mind during times of success and helped get me back up when I was demotivated or frustrated. Your patience and trust and support helped more than I can put into words.

- My Parents: You always believed in me and supported my ideas with kind words, advice and help whenever I needed it. I am forever grateful for your help, love, and inspiration.

- My Friends and Siblings: Thank you for being my support system, for reliably helping me take the next step when things seemed too difficult and for distracting me and keeping my life interesting and engaging.

TABLE OF CONTENTS

LIST OF ABBREVIATIONS

PV	Photo-Voltaic
CSP	Concentrated Solar Power
IEA	International Energy Association
TCES	Thermo-Chemical Energy Storage
SETO	Solar Energy Technologies Office
DOE	U.S. Department of Energy
EERE	Energy Efficiency and Renewable Energy
MgO	Magnesium Oxide
MnO	Manganese Oxide
MgMnO	Magnesium Manganese Oxide
PVA	Polyvinyl Alcohol
TGA	Thermo-Gravimetric Analyzer
ECR	Electrical Conductivity Relaxation
Alumina	Aluminium Oxide, Al2O3
SLPM	Standard Liters Per Minute
HPCC	High Performance Computing Cluster
MoSi2	Molybdenum Disilicide
LCOS	Levelized Cost of Storage
PSA	Pressure Swing Adsorption
MVR	Mechanical Vapor Recompression

CHAPTER 1

INTRODUCTION

This thesis describes the efforts of developing a novel renewable energy storage reactor concept into a working prototype. The goal was to prove the feasibility of the concept and show that the use of the energy storage material MgMnO with this reactor is a potential solution to the challenges of reducing greenhouse gas emissions by the energy and industrial sectors. This chapter introduces the state of the art of energy storage and solar energy, following chapters give background on the energy storage material MgMnO, describe the reactor and path towards a functioning experimental prototype. Later chapters focus on improving the throughput of material and describe the work done to facilitate a continuous, efficient chemical charging reaction at high temperatures. The last chapter gives a summary of the progress to date and suggests future challenges and potential applications of this promising technology.

1.1 The Need for an Energy Storage Solution

The storage of renewable energy, especially solar, is key to deeper penetration of renewable energy into the power market [1]. The low reliability of direct solar power generation makes it difficult to invest in and also harms other power generation technology designed to run at full capacity. The intermittent availability of solar radiation depends on the cloud coverage, time of day and recurring changes such as seasonal differences caused by the rotational axis of the earth and its position on the orbit around the sun [2]. If renewable energy is given the priority, conventional power plants have to scale back on a sunny day to make room for the solar energy in the grid. Figure 1.1 shows how a sunny and windy day in California resulted in a large renewable energy influx into the power grid (red line). As a response to the quick increase in renewable power, the natural gas power generation had to be scaled back and electricity imports were reduced to the point where electricity had to be exported to protect the grid.

The curve that describes this rapid change in the power mix is often called a duck curve due to its loose resemblance to the animal (imagine the area between the yellow and green curve in Figure 1.1). This figure powerfully visualizes the problem of high solar power influx into the grid and a

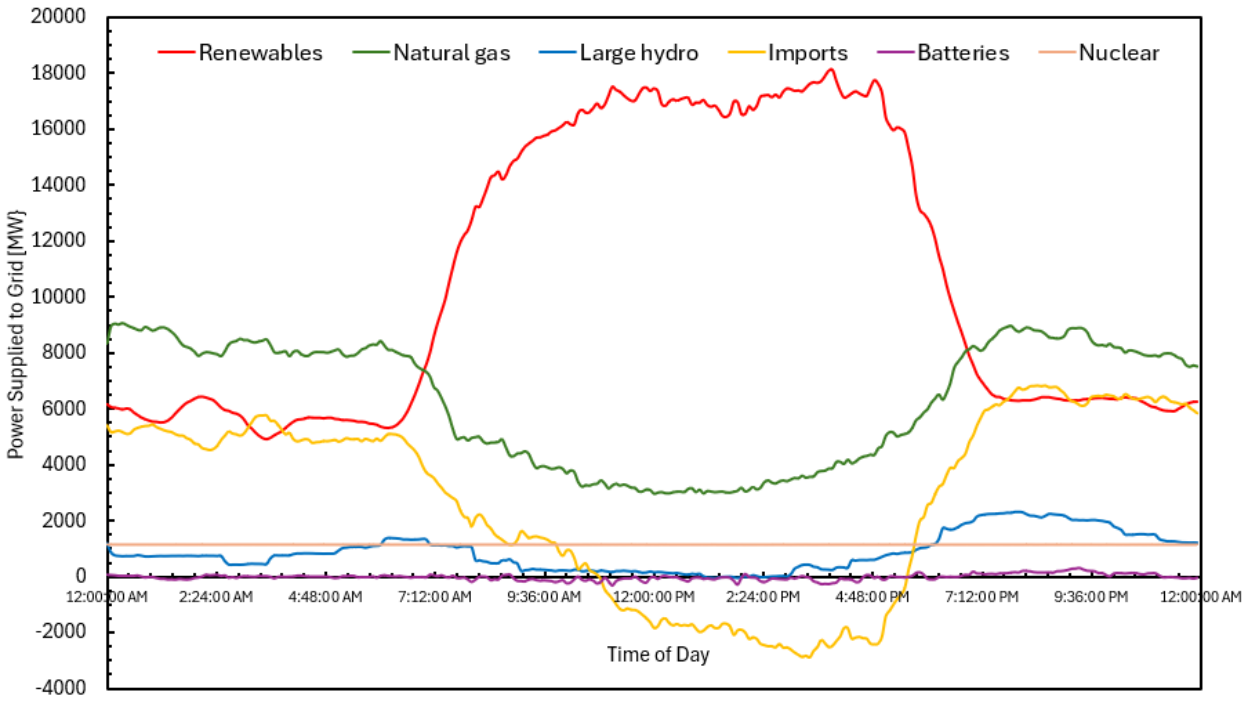

Figure 1.1 **Effect of PV on Other Energies** This plot shows the grid contributions in California on April 24th 2021. 95 % renewable energy was used at times. The timing of the large spike is correlating with the sunrise and sunset and it is clear that the fossil fuel power plants have to be throttled down to avoid overloading the grid. Some energy has to be sold (negative import) to protect the grid since the fossil fuel plants cannot be completely shut down as they are needed again after sunset. Figure data taken from CAISO [3].

reduced energy demand due to domestic Photo-Voltaic (PV) generation. The political push towards renewable energy usage and the difficulty of turning off PV units led to preferential treatment of renewable energy when available. The necessity for conventional fossil or nuclear power plants to provide stability at night is evident.

The priority of renewable power causes conventional power plants to run below full power during the day and hence run outside of the designed optimal operating conditions which often leads to reduced efficiency, higher emissions and higher cost of operation [4]. In 2023, California's Public Utilities Commission enacted two new regulations that were aimed at reducing the incentive for individuals to sell rooftop solar power to the utility companies. The mandates included reduced payment for day time energy sales to the grid from individual homes as well as apartment buildings, schools and businesses [5]. These points are brought up to show the current struggle of the

unreliability and prioritization of renewable electricity. Back-up power plants are needed to ensure availability of electricity at all times while the already installed PV in some areas exceeds the electricity demands during the day. A way to store the excess energy is desperately needed.

A helpful analogy might be to replace the power grid with a system of pipes. The power generation systems are pumps that pump water into the pipes, the consumers are valves that let the water out. If too many pumps put water into the pipes, they will burst, so it is important to only pump in as much water as is being taken out to maintain a safe pressure. In this analogy, solar power is represented by a pump that is very powerful but only turns on randomly. Currently all other pumps are throttled down when the solar pump kicks on which makes the other pumps less efficient but saves the pipes from bursting. It would be better to add a water tower to the solar pump, that way it can pump the water up in the tower when it is on and the tower can supply a constant flow of water to the pipes. This is the solution discussed here.

Since this solution is focused on storing solar power, a brief introduction to the main players in solar energy is given here. Concentrated Solar Power (CSP) has a long history of industrial power generation, reaching back into the 1800s in use with steam engines. The concept involves an array of mirrors that focuses the radiation of the sun on one spot and uses the heat for a process. Fast forward to the 21^{st} century, CSP plants across the globe had produced an impressive 14.5 TWh of power in the year 2021 [6]. A majority of this power was produced during sun hours, competing not only with conventional fossil fuel power generation but also with PV units which directly generate electricity from solar radiation. The international energy association (IEA) produced a roadmap in 2010 that proposes a path of utilizing CSP as a major electricity producing technology (11.3% of global energy by 2050).

There are major differences between CSP and PV: Firstly, there is the energy form that the process uses. CSP focuses the solar radiation on a cavity receiver. The heat from that radiation is then used to drive processes. To generate electricity, the heat must be transferred to a working fluid which can be used to power a generator through a Rankine cycle. PV on the other hand directly converts sunlight into an electrical potential through semiconducting materials [7]. A

second important point is the efficiency. The mirrors are very effective at redirecting the sunlight into the cavity and so most of the solar radiation that hits the area of the mirrors is used to heat the cavity. However, the process that uses the heat is always bound by the Carnot efficiency and other, more practical restrictions. In order to compare the two technologies, the thermal CSP efficiency of >90 % has to be multiplied with the efficiency of the process that is used to convert the heat into electricity, unless the heat is directly used in an industrial process. PV cells have an efficiency around 20-25 % which means that they convert about 1/5 of the radiation that hits the panel into electricity [7]. The usable scale of the technology is a third major difference. To produce electricity from CSP, a large steam Rankine power cycle is needed. This requires large financial investments and large areas to catch and reflect solar radiation. PV on the other hand is a small scale technology. PV panels can be found in wrist watches to charge tiny batteries or on top of a camper van or house. The scalability is much broader due to the small size availability that goes from < 1 W to big panel arrays that produce > 1 MW.

1.2 Current Energy Storage Systems

The water pipe example shows that it is imperative to find ways to store excess electrical energy that is being produced by intermittent sources immediately. Long-term goals should include enough renewable energy installation to produce and store energy for reliable around the clock use. Electrical energy storage systems are often categorized by the form that the energy is stored in. The following list gives an introduction to the most common electrical energy storage systems currently used:

- *Electrical*: Electricity is directly stored as electrical potential in a capacitor or coil. Double-layer capacitors use a dielectric gap between two conductors to store the electrical potential. The storage capacity depends on the voltage and capacitance of the capacitor and the energy density reaches between 5-15 Wh kg^{-1}. This method has a reported loss of about 5 % of the total energy per day [8].

  Superconducting magnetic energy storage utilizes a superconducting coil to store the electri-

cal potential. The technology has a fast response time of less than 100 ms but a lower energy density and very low operating temperature of −270 °C are downsides.

- *Electrochemical*: Secondary batteries and flow batteries. Secondary batteries are storage devices where the chemical potential of the storage media is directly converted to electricity. The technology is based on the electrochemical potential between two different materials. The anode and cathode are separated via an electrolyte and semi-permeable barrier and form the electrochemical cell. The potential depends on the material combination of anode and cathode. Lead-acid batteries are most wide-spread and have a high cell-voltage and low cost [9]. Nickel-Metal Hydride and Nickel-Cadmium batteries are more expensive but show better energy density and longer life cycle compared to lead-acid batteries. The next upgrade are lithium-ion batteries that boast faster charging and much higher energy density but are more expensive and require rare-earth metals [1].

  Flow batteries are a variation where the chemical potential is stored in two electrolytes that are stored separately and pumped through the system. The chemical reaction is a reduction-oxidation. They have a lower efficiency due to the need for pumps to move the electrolyte but have a fast response time and no self-discharge. Examples are regenerative fuel cell, vanadium redox, and zinc bromin batteries.

- *Chemical*: Hydrogen storage. The main use case for chemical potential storage is hydrogen. The potential is created by using electrolysis to split water into oxygen and hydrogen and storing the hydrogen. The stored potential can be released directly as electrical energy via a fuel cell. This device generates electricity by combining the hydrogen and oxygen from the air to form water [10]. Other energy release mechanisms include internal combustion engines and gas turbines, where the hydrogen is burned and the heat is turned into electricity via a thermodynamic process and a generator. The advantage of hydrogen over electrochemical battery storage is the higher energy density of hydrogen, but the downsides are lower efficiency due to high storage pressure and safety concerns connected with the high pressure vessel filled

with highly combustible gas.

- *Mechanical*: Different forms of storing electrical energy in the form of mechanical potential are pumped hyroelectric, flywheel, compressed air. Pumped hydro is the most used energy storage technology in the world with at least 150 GW installed, which meant that 99% of worldwide bulk stored energy in 2012 came from pumped hydro storage [11]. The operating principle is also the main drawback of the technology. Vast amounts of water need to be stored at a large height to provide a big storage potential. The water is pumped into a storage lake to store mechanical potential and it is released back down through a turbine to convert the potential into electrical energy. The technology has an impressive efficiency of 70-80% [11] and is expected to be further developed in the future. However, the total capacity is naturally limited by availability of potential water reservoirs at high altitude. Flywheel energy storage uses a spinning mass to store mechanical potential. They show a fast response time and long life cycle but friction leads to high energy losses over time [1]. Compressed air can be used to store electrical energy. The air is compressed to around 70 bar and stored in large sub-level cavities such as mines and caves. To retrieve the energy, the air is pre-heated and expanded through a turbine which is connected to a generator. This technology is able to store large amounts of energy for long times but the few systems that are operational have lower efficiency of around 30-70%.

- *Thermal*: Thermal heat energy storage methods are divided into two sections, sensible heat storage and latent heat storage. Sensible heat can be stored in materials with preferably high specific heat capacities. These materials are simply heated up and the amount of energy stored depends on the mass, specific heat and temperature difference. Storage medias are water, thermal oils, concrete, and molten salts [12]. This method can store heat at high temperatures, depending on the storage media, but the energy density is low compared to latent heat storage. Latent heat storage uses the phase change of the storage material to store large amounts of energy. Materials range from paraffin and alcohols to salts. The drawback

of many of these materials is poor heat conduction [12]. Both methods require insulation to minimize heat loss. Even with insulation, the thermal storage is not able to provide long-term energy storage.

This list gives a brief introduction into the current electrical energy storage methods. The diversity of approaches emphasizes the creativity in trying to find a solution to the energy storage problem at hand.

The state of the art CSP storage method is thermal energy storage. This is effective to extend the power generation for a few hours past sun down (short term storage) but is not able to mitigate power loss during shorter winter days or a cloudy week [13].

The reason is the energy loss due to heat loss of the storage medium through the insulation which prevents the technology form efficiently storing energy for more than a few hours/days. Another issue that comes with the need for an insulated storage is the capacity restriction. The liquid or solid storage medium must be kept in insulated and sometimes pressurized containers, therefore it is not economic to build CSP plants with very large thermal storage percentile for off sun power delivery [13].

Beyond electrical energy storage, many industrial processes require high temperature heat that is commonly provided via the combustion of fossil fuels [14, 15]. Many of these processes have been labeled "hard to decarbonize" due to the requirement of extensive amounts of high-grade heat. A storage solution that has the potential to store renewable energy in a form that makes it transferable into both, electricity and high-grade heat would be universally applicable across many fields and industries.

An emerging branch of energy storage that promises this capacity is thermo-chemical energy storage (TCES) . Here, an endothermic chemical process converts reactants at high temperature into a charged state. The energy used for that process can be released as high temperature heat in the exothermic reverse reaction. Most research can be categorized in hydride systems, organic systems, and metal oxide systems. None of these are at this point economically viable, and many have design restrictions that limit the heat to chemical efficiency values around 50% [16], [17],

[18]. However, the broad applicability of reliable, renewable high-grade heat drives many research projects in this area.

1.2.1 Hydride systems

There are many metal hydride and ammonia cycles being researched. The metal hydrides that have been studied are lithium hydride, calcium hydride, and magnesium hydride [19]. Magnesium hydride has gotten the most focus because it has a flexible operating temperature and pressure between 200-500 °C and 1-100 bar. Figure 1.2 shows the schematics of the reactions. There has been significant research invested in trying to overcome problems with low reaction kinetics of the reactants and poor cyclability. The potential solutions include increasing the surface area to improve reaction rate via nano-structures and improving the poor heat conductivity by investigating different geometries [20], [21].

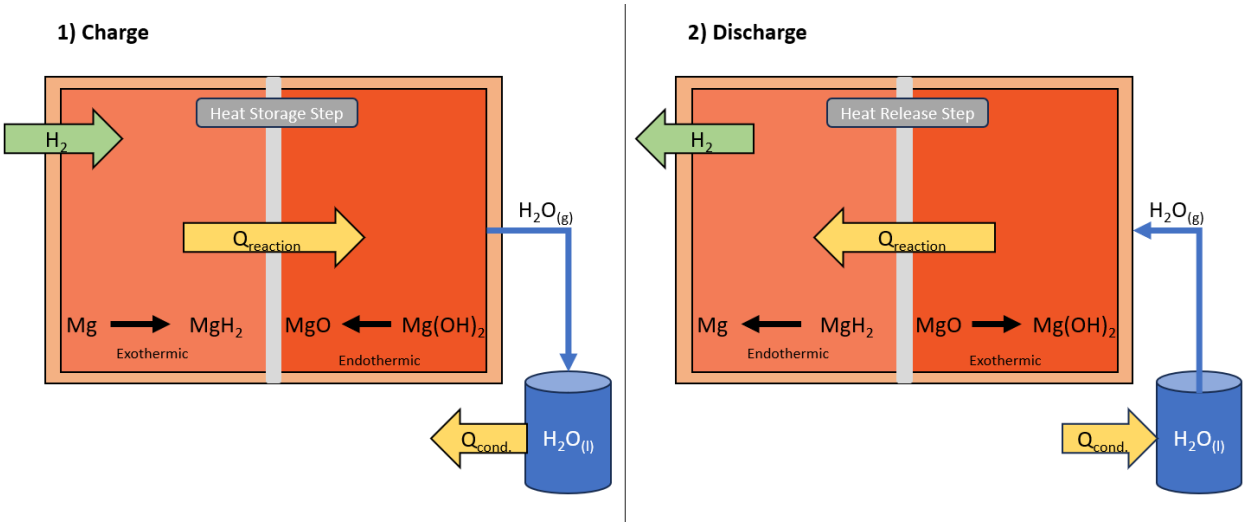

Figure 1.2 **Mg Hydride Schematics** Magnesium hydroxide energy storage schematics. Absorption of hydrogen is shown in the charging step on the left while the reverse process is shown on the right. The heat of the reaction of the exothermic reaction fuels the endothermic reaction in either step.

Ammonia cycles for energy storage are derived from the well-known Haber-Bosch fertilizer production process. The high energy density, experience with and availability of the reactants, and the reversibility are advantages of this approach. The main issue is the lack of an effective catalytic converter that can convert all the reactants which is needed for higher efficiencies.

1.2.2 Metal oxide systems

Metal oxide storage systems can be categorized in three different sub-categories: Carbonate, hydroxide, and redox systems.

For the hydroxide systems, two well performing materials are the calcium oxide and calcium hydroxide pair $CaO/Ca(OH)_2$ and the magnesium oxide and magnesium hydroxide pair $MgO/Mg(OH)_2$. Both have similar energy densities and reaction mechanisms. The $CaO/Ca(OH)_2$ system has a higher temperature and is therefore more interesting. The operating temperatures and pressures are 400-900 °C and 0-2 bar [17]. The material is charged by heating which leads the to the decomposition of $Ca(OH)_2$ to CaO and H_2O. The material releases energy when it is re-hydrated with steam [22]. Many different concepts have been designed to utilize the heat of reaction for energy storage [17]. A sample concept using separate reactors for the two reaction steps and can be seen in Figure 1.3. Criado et al. propose a system which has a calculated efficiency of 63% [22].

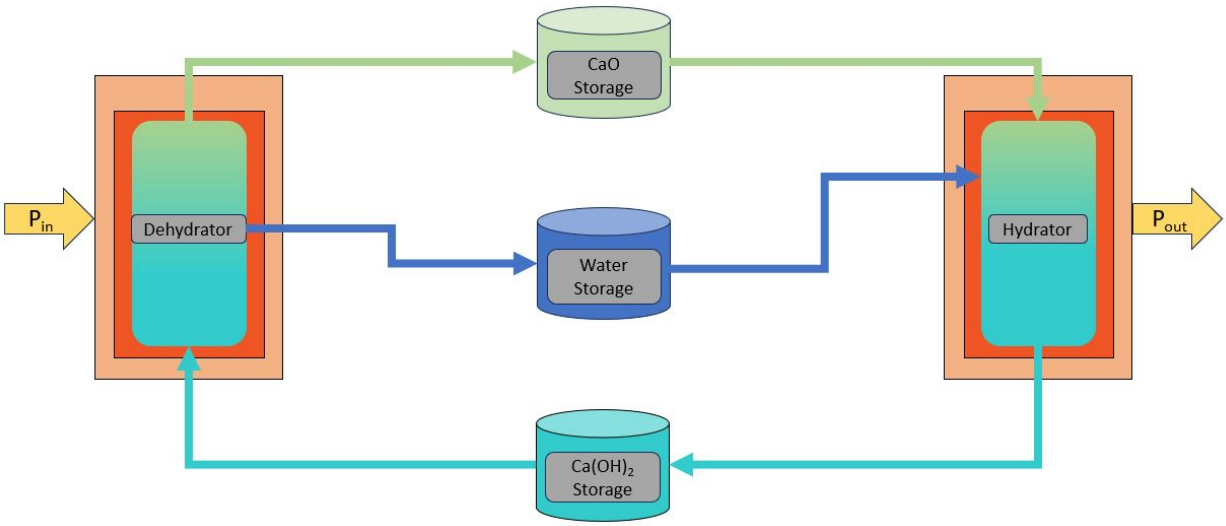

Figure 1.3 **CaOH Schematics** The hydration stage is shown on the right. The material bed is fluidized with steam and heat is released. The dehydration stage on the left shows how the material is charged by fluidizing the $Ca(OH)_2$ bed with heated air and removing the released water vapor.

For the carbonate systems, the most promising candidate is $CaO/CaCO_3$ because it has a high energy density and the material is abundantly available. The operating temperatures and pressures are 700-1000 °C and 0-10 bar [17]. A few systems with this concept have been developed, although

they struggle with cyclability and cost.

Redox systems are very promising because of the high energy density, temperature and cyclic stability. The process involves an endothermic reduction reaction where the reactant releases oxygen. When the charged material comes in contact with an oxidizer, heat is released as the oxygen is absorbed.

Some research is done in identifying potential powderized metals that can be oxidized to produce heat and reduced to recharge the chemical potential. A review has identified the lack of reactor designs to utilize the powdered metal for energy storage as the main technological barrier [23]. However, the Iron+ project in the Netherlands and researchers Baigmohammadi et al. claim successful utilization of iron powders in oxidation reactors to produce heat and steam with successive regeneration of the powder using renewable energy reduction [24].

Another redox process that has been researched is Co_3O_4/CoO. Karagiannakis et al. built an experimental reactor operating at temperatures of 700-1000 °C for the oxidation and reduction [22]. The material was extruded into a honeycomb structure to increase the surface area. A schematics of the setup is shown in Figure 1.4.

The struggles with this and other redox approaches lies in the unproven designs and often high costs as well as relatively low exergy in the heat released at <700 °C.

A focus for researchers has been the splitting of water and natural gas using perovskites as catalyst and concentrated solar power to provide the energy [16]. The process promises to produce hydrogen or even compounds that can be used to make synthetic liquid fuels. The problem with the concept is that the high temperature chemical reactors are designed to operate on a swing cycle principle. The catalyst reacts with a gas at high temperature and then is cooled down again to reset the catalyst and 'harvest' the chemical potential. Other processes require cooling of the high-temperature reactants for safe handling and storage. The sensitive heat difference between the reaction temperature and the storage temperature is a main cost driver for these systems. Costly secondary cycles are required to utilize the sensible heat and achieve high thermal efficiency. If the sensible heat is rejected into the environment, the low reported thermal efficiencies of 5-10 %

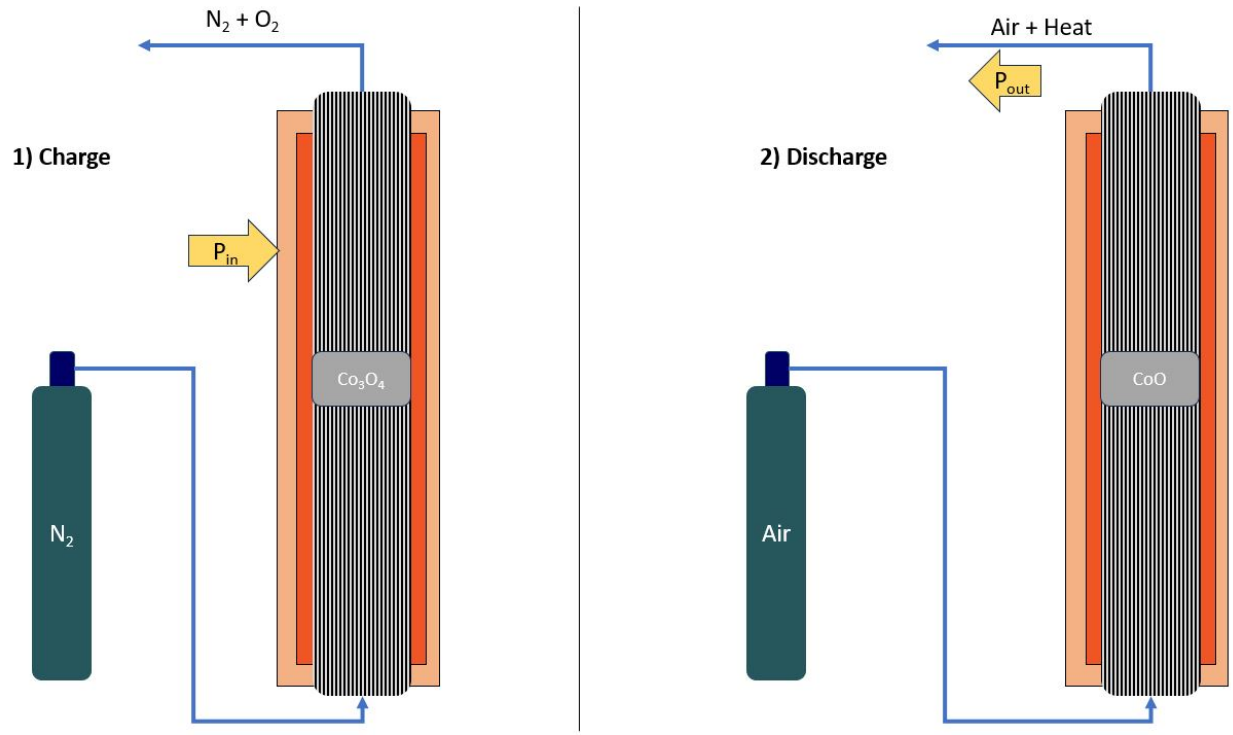

Figure 1.4 **CoO Schematics** An experimental setup described by Karagiannakis et al. [25] uses nitrogen to reduce the storage media which is extruded in a honeycomb structure. The reduction temperature is 1000 °C. For the oxidation step, air is blown through the reactor, the material reacts and releases heat around 700 °C.

result in a requirement for bigger solar collector fields to provide the additional heat that is wasted.

As previously mentioned, high-grade heat is a desirable product of renewable energy storage. A system that is able to provide high-temperature heat has a broad applicability for many industries. Most approaches mentioned here have a lower temperature of reaction on the discharge cycle, limiting the use the technology.

This work introduces a novel redox energy storage system that is competitive with fossil fuels and is as promising or more than the here mentioned technologies.

1.3 Problem Statement for this Project

This work was supported and inspired through my participation on the SoFuel project. The SoFuel project is funded by the Solar Energy Technologies Office (SETO) branch of the Department of Energy (DOE) Office of Energy Efficiency and Renewable Energy (EERE) . It started January 1^{st} 2020 and funding was granted for three years with quarterly reports and yearly go/no-go decisions.

The proposed project was to develop, manufacture, test and validate a system to charge and discharge zero-emission solid state fuel for long duration renewable energy storage.

The idea for the project arose from the previously developed and researched fuel consisting of a mix of Magnesium Oxide (MgO) and Manganese Oxide (MnO) .

Magnesium Manganese Oxide (MgMnO) releases oxygen when it is heated up in a low oxygen atmosphere [26]. This endothermic reduction increases the chemical potential of the material. This state is shown on the right hand side of Equation 1.1 and requires an environment of around 1500 °C with an atmosphere consisting of a shielding gas and less than 1% oxygen. The reverse reaction releases the chemical potential stored in the material as it oxidizes. This oxidation occurs when the reduced (charged) material is heated to temperatures around 1000 °C and exposed to air or an atmosphere consisting of >1% oxygen.

$$\mathrm{MgMnO_2} + \frac{\mathrm{y}}{2}\mathrm{O_2} \longleftrightarrow \mathrm{MgMnO_{2+y}} + \Delta \mathrm{H}_f \tag{1.1}$$

This material is a great candidate for an energy storage system. King et al. [27] demonstrated that the reaction of a 1:1 molar ratio mixture of the MgO and MnO material has an energy storage density of 1172 ± 110 $\mathrm{MJm^{-3}}$ using the bulk density of the pelletized material of approximately 2000 $\mathrm{kg/m^3}$. Electrochemical batteries are evaluated on the basis of an energy density with the unit of Wh/l or specific energy Wh/kg. The 1:1 MgMnO material has an energy density of 325.5 Wh/l or specific energy of 162 Wh/kg. These numbers are in the range of lithium-ion batteries (90-190 Wh/kg, [9]). This high energy density is even more impressive when considering the availability of the raw materials. While highly energy dense batteries need rare earth metals, MgO and MnO are abundantly available in the earth's crust. MgO and MnO are among the 10 most abundand molecules in the earth's crust [28]. A third desirable factor is great cycling stability. The supplemental information seciton of Randhir et al.[29] shows cycling data of 50 cycles of charging and discharging with negligible mass change difference after 10-15 cycles. The material also exhibits desirable storage stability, experiments proved no chemical potential loss of charged particles after 3 months of storage. These are reasons why multiple projects are working on technologies to use this material as an energy storage system [30, 31] (Also STORES, RedoxBlox,

SoFuel). As mentioned above, the material needs a low oxygen atmosphere and high temperature environment to release oxygen. The innovation that the SoFuel project proposes is the use of a moving bed reactor with a counter-currently flowing gas.

Figure 1.5 shows concept schematics of the charging reactor. The pelletized fuel moves downward through the reactor via gravity feed while the inert gas flows upwards through the tube.

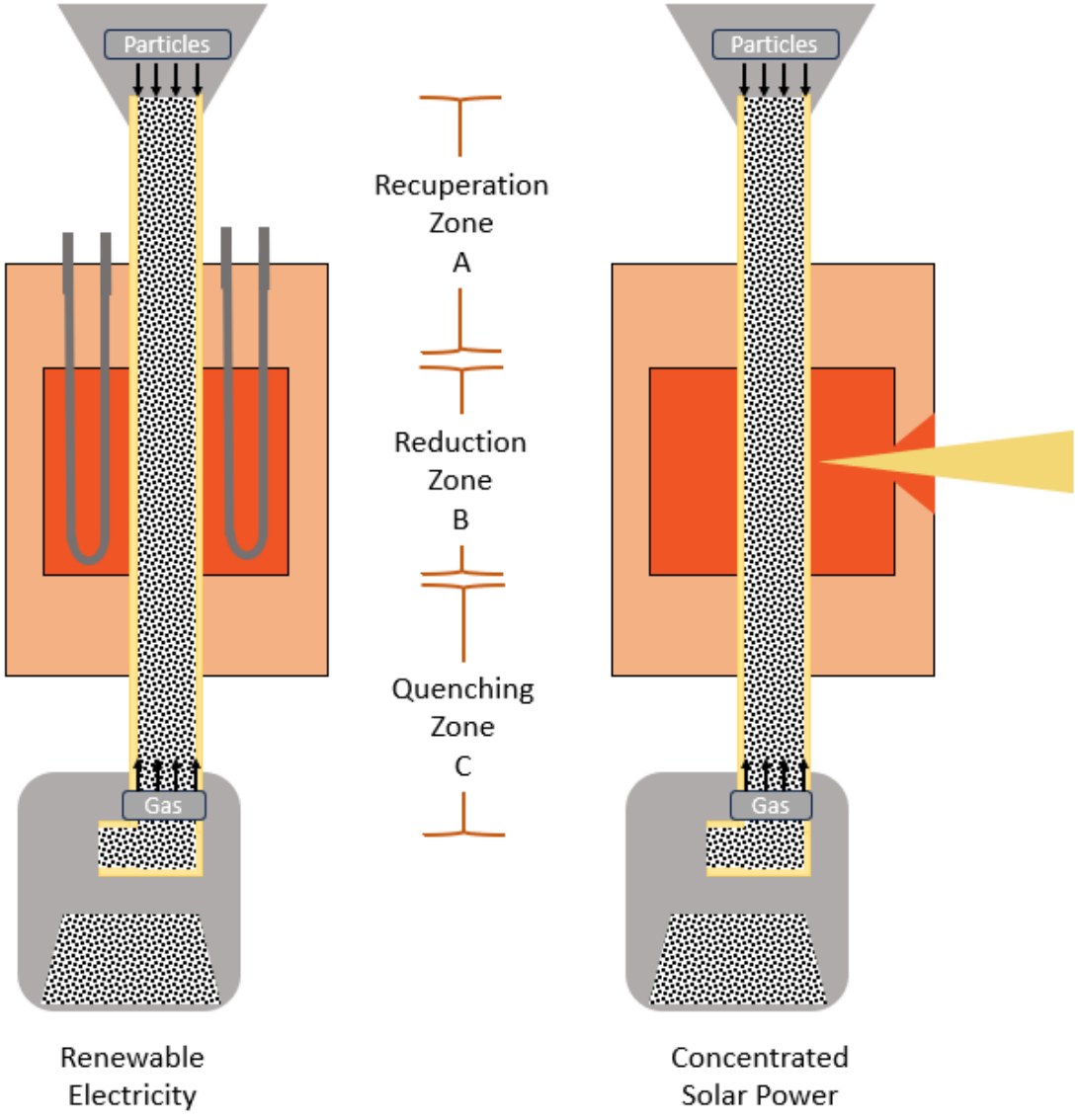

Figure 1.5 **MgMnO Moving Bed Reactor Concept** The schematics of the moving bed reactor concept. Renewable electricity (left) or CSP (right) can be used to provide the heat that charges the energy storage material MgMnO. The reactor consists of the feed hopper, reactor tube, heated cavity and particle control and collection unit.

The counter-flow approach has a number of advantages:

- The possibility of continuing operation without restrictions due to storage volume: Flowing the material continuously poses many challenges and pushes the boundary of high temperature bed flow but it is a key feature of this reactor concept. A static bed storage system is limited to the installed volume of particles, similar to a battery that has a maximum capacity. Having a continuous flow of particles through the reactor enables us to charge or discharge particles as long as there are reserves of discharged or charged particles available. This approach is therefore comparable to a fossil fuel power plant that is able to feed energy into the grid as long as fuel is available. This is beneficial for renewable energy storage as the supply is fluctuating greatly and so a limited volume system will likely oscillate between being below capacity and being full and unable to store energy that is available.

- Sensible heat recuperation: All mass streams enter and exit the reactor tube at or close to room temperature, ensuring low sensible heat loss and high efficiency. This solution makes the SoFuel project highly efficient and very competitive. The counter-flowing gas recuperates the heat of the particles by cooling the particles exiting the reactor and preheating the particles entering the reactor. This feature will be explained in detail and with mathematical and experimental proof in this thesis.

- Adaptable design: The reactor can be powered by CSP or excess renewable electricity. As the name So(lar)Fuel suggests, CSP is the focus of the SoFuel project. With trends in decentralized power plants and a big increase in urban PV installations, any system that wants to be competitive in such a diverse market needs to be adaptable. The charging reactor can be fueled by renewable electricity or CSP which makes this system versatile.

The following chapters of this thesis will describe the process of developing, testing and improving the charging reactor for this system.

CHAPTER 2

CHEMISTRY AND PHYSICS OF THE ENERGY STORAGE MATERIAL MGMNO

This thesis is focused on solving engineering challenges that arise when trying to facilitate the reduction reaction of the TCES material MgMnO. This chapter is aimed at introducing the reader to the important underlying chemistry and physics related to the problem.

2.1 Material Chemistry

The advantages of TCES systems are high energy density and the ability to store heat for extended periods of time [16]. In TCES, the highest energy densities are found among redox systems [32]. Redox is a term combining the abbreviations of reduction and oxidation and is commonly used to describe a reversible chemical reaction where a reactant absorbs and releases oxygen. The release of oxygen is the endothermic reduction reaction. The oxidation of the reactant is the reverse, exothermic reaction. For TCES, the energy is stored in the material via the reduction reaction. Hence, the reduced material represents the charged state. It has a chemical potential due to the absence of oxygen in the molecules. To release the stored energy, the material is submitted to oxidizing conditions, causing it to react with oxygen in the environment. This reaction releases heat which can be used in a secondary process. The metal oxides used for TCES systems generally require high temperature environments for the reduction and oxidation due to slow reaction kinetics at lower temperatures. This means that they can usually be stored at ambient conditions without losing stored chemical potential due to oxidation at ambient conditions [32].

The simplified non-stoichiometric reversible reduction reaction for the Mg-Mn-O redox system is introduced in Section 1.3 (Equation 1.1). A more accurate description of the process requires a dive into the structure of the molecules. When MgO and MnO are mixed and heated under oxidizing conditions, they form a crystal structure categorized as a spinel. The reduction and oxidation causes a phase change of the lattice structure which results in a high reaction enthalpy as mentioned by Randhir et al. [26]. Because high temperatures of at least 1000 °C are required for oxidation and reduction, the material is very stable at room temperature and can be stored in reduced (meaning charged) condition without any loss in chemical potential.

Recent publications have studied the properties of MgMnO as a TCES medium, see [27], [26], [33], [34]. From these publications we get a comprehensive thermodynamic equilibrium model and an understanding of the energy storage capacity and cyclability of the material.

King et al. used drop calorimetry as well as acid-solution calorimetry to determine the storage capacities of different MgMnO materials [27]. They demonstrated that the reaction of a 1:1 molar ratio mixture of the two powders has an enthalpy of formation (ΔH_f) of 1063.6 ± 7.9 kJ/mol for the oxidation and 989.5 ± 7.2 kJ/mol for the reduction. The difference in enthalpies is due to the different reaction temperatures that decrease the energy needed for the oxygen to diffuse out of the material. Through these calorimetry experiments, the chemical energy storage capacity was determined to be 586.3 ± 55 kJ/kg. From this value, the energy storage density of the 1:1 molar ratio material was calculated to be 1172 ± 110 MJm^{-3} using the bulk density of the pelletized material of approximately 2000 kg/m^3. Experiments mentioned later in this work suggest that the chemical energy storage density might be more in the range of 800 kJ/kg.

From their results we can also determine the specific heat $c_{p,s}$ of the particles. The enthalpy of the material and the temperature difference of the drop calorimetry experiment can be used to calculate $c_{p,s}$

$$c_{p,s} = \frac{\Delta H_{OX}}{\Delta T} \tag{2.1}$$

using the results from [27] where experiments show that ΔH_{OX} is approximately 927 kJ/kg and $\Delta T = 975$ K, we get $c_{p,s} = 0.95$ kJ/kgK. A drop calomeritry experiment from 1500 °C to 1000 °C was reported with a sensible heat of around 445 kJ/kg. This suggests that the heat capacity of the material decreases slightly at higher temperatures, as $c_{p,1000-1500} = 0.89 kJ/kgK$. More research is necessary to understand all thermodynamic properties of this material.

2.2 Particle Manufacturing

The first step towards experimental validation of this new TCES material and reactor was to solve the problem of how to use the material. The reactants, MgO and MnO are available as fine powders. These powders have very different densities (3.58 g/cm^3 MgO and 5.37 g/cm^3 MnO) [35][36]. If the raw powders were fed into the reactor, the downward movement of the powdered

bed in combination with the counterflowing gas would cause separation of the reactants. A second issue with using pure powders is that MgO is hydroscopic. This would require a more complicated storage solution to prevent the absorption of moisture. Lastly, the flowability of powders at high temperatures is poor and would likely lead to sintering which would clog the reactor and could damage it. For these reasons it is necessary to mix the materials and then form them into a matrix that enables easy storage, a constant molar ratio of the reactants, and promises good flowability through the high-temperature reactor.

A recent 2024 publication reviews TCES systems that have solved this problem by pelletizing their reactants [37]. This is the approach that was selected for this material as well. Other systems form porous matrices from their reactants or work with vaporized metals [38],[39].

For the amount of particles that were needed and with a scale up in mind, a disc-pelletization process was chosen for pelletization of the energy storage material. This process is widely used in applications ranging from pesticides to coal fines and produces spherical particles with good dimensional accuracy by combining powders with a binder in a turning drum. Using a lab-scale Eirich EL1 pelletizer, production of 1 mm diameter spherical particles was started. A water-based polyvinyl alcohol (PVA) binder was used to form particles and the finished pellets were calcined in ceramic crucibles at 1500 °C for 20 hours. During the calcining, the binder evaporates and the two powders are bonded together strongly. Even the individual particles are bonded together during the process and need to be separated by applying force to them. The final step is to sieve the particles to ensure an even size distribution. Figure 2.1 shows the particles at different stages during the manufacturing.

One important factor for the entire project was the particle size. The decision has powerful consequences that affect the manufacturing process, reaction kinetics and heat transfer among others. One crucial condition for most chemical reactions is that the reactants are in close proximity to exchange electrons, atoms or other processes that define the reaction. This rule restricts the particle size of the SoFuel material. Since the oxidation reaction requires the gaseous oxygen to be absorbed by the material, a smaller particle size results in larger cross-sectional area per mass and

Figure 2.1 **1mm Particles** 1mm diameter SoFuel particles after exiting the EL1 disc pelletizer (left) and after calcination (right)

increases the proximity of the material to the reactant oxygen.

This can be supplemented by forming porous particles with large internal surface area that is conductive to reaction.

A second limiting factor for the particle size is the radiative heat transfer. At reduction temperatures of 1500 °C, radiation becomes a major form of heat transfer between particles. The Stefan-Boltzmann law (see Equation 2.2) enables us to calculate the power that is emitted by a body of surface area A and temperature T [40]

$$q = A\epsilon\sigma T^4 \tag{2.2}$$

Since the surface of a spherical particle increases quadratically with the radius (see Equation 2.3), the emitted power is quadratic dependent on the particle diameter

$$A = 4\pi r^2 \tag{2.3}$$

Figure 2.2 shows the relationship between particle diameter and radiated power for a material with $\epsilon = 1$. It shows that a smaller particle diameter greatly reduces radiative heat transfer which has a major negative effect: The need for a longer residence time of the particles in the reduction zone as the heat transfer is the bottleneck to the quick conversion of the reactants.

The reason for this is that the reactor type that is investigated operates in a packed moving bed configuration. This means that the particles mostly stay in position relative to their neighbors as the entire bed moves downwards together, there is no heat convection in the radial direction. Therefore, the particles at the outer edge of the bed will be heated up quickly while the particles at the center are heated up depending on the heat transfer of the bed. Hence the benefit of larger particles as they carry the heat into the core of the bed more quickly.

As mentioned above, a larger particle needs more time to react compared to a smaller particle. The reaction time is explored in the following section as well as in Chapter 5. Equation 2.4 is used to calculate the reaction time necessary for reduction. Figure 2.3 shows the influence of particle diameter on the time scale of the reaction and the thermal diffusion. It emphasizes the optimization problem of particle size since an increase in diameter improves the thermal diffusion but also increases the reaction time.

Larger particles were produced after flowability problems (explained in detail in Chapter 3) with the 1 mm diameter particles. Figure 2.4 shows the bigger 3.5 mm diameter particles produced with the EL1. Spheronization, an extra manufacturing step was required to maintain a spherical shape as the disc pelletizer produced non-spherical pellets due to the small diameter of the mixing

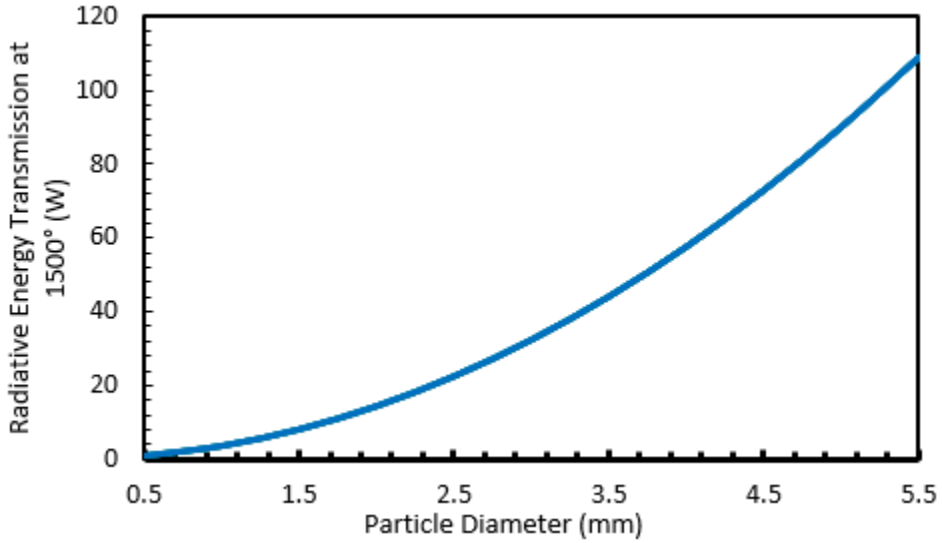

Figure 2.2 **Emissivity vs Particle Diameter** The theoretical radiated power of spherical particles with emissivity 1 and different diameters. This plot visualized the value of larger particles for increased heat transmission.

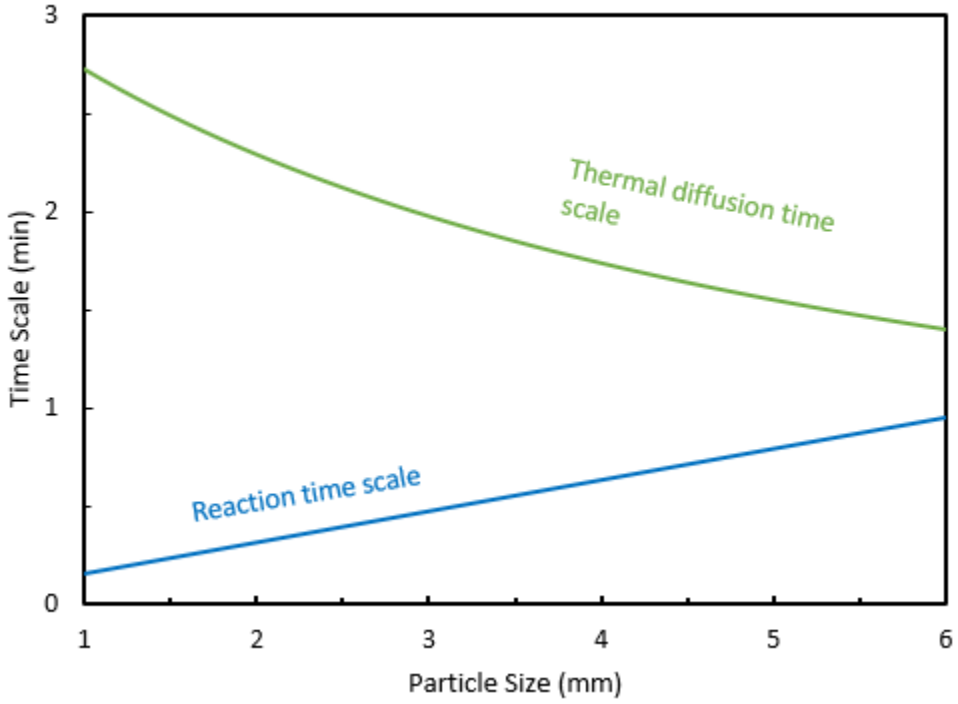

Figure 2.3 **Particle Diameter Influence on Thermal Diffusion and Reactivity** Calculated time scales of the thermal diffusion and the chemical reaction in relation to the particle diameter. This shows the need for optimization of the diameter to provide sufficient heat penetration into the bed and enough time for the reduction.

bowl of the EL1. The spheronization was accomplished by exposing the disc-pelletized particles to a quickly-spinning disc that rounded off the corners.

Adding a spheronization step to produce round 3.5 mm particles increased the production time significantly. As the project moved to even larger 5.5 mm particles due to flowability issues discussed in later chapters, the process of pellet production was out-sourced to a company specialized in disc-pelletization of powdered materials.

2.3 Chemical Kinetics Model

Any computational approach to investigating the redox reaction of the material in a reactor requires a model explaining the reaction kinetics of the material. However, understanding the reaction kinetics of a chemical compound is not trivial. In the case of MgMnO, there is no prior work that has analyzed the reduction or oxidation sufficiently to build a model. Hence our team designed experiments that produced enough data to enable us to build an accurate kinetics model

Figure 2.4 **3.5 mm Particles** 3.5 mm diameter MgMnO particles produced in the EL1 and post-processed using spheronization.

to be used in all simulations of the different use cases of the material.

The model is estimating the change in y in Equation 1.1. This was achieved by fitting an Arrhenius-type equation to a series of relaxation experiments. Relaxation-type experiments are used to study the response of a sample to a sudden change in chemical potential. To begin, the sample is brought to a thermodynamic equilibrium state where no changes in temperature or chemical composition occur. Then, while maintaining a constant temperature, a gradient in chemical potential is introduced. For oxidation and reduction, this is done via a rapid change in oxygen partial pressure p_{O_2} in the atmosphere surrounding the sample. The sample responds to the gradient by either absorbing or releasing oxygen, which results in a change in mass and electrical conductivity. A thermo-gravimetric analyzer (TGA) can be used to measure the mass change during relaxation experiments. The method of electrical conductivity relaxation (ECR) focuses on the conductivity change during a relaxation experiment. This method is more sensitive to changes in p_{O_2} due to the higher mobility of the electronic defects compared to the ionic defects [41] but

needs a carefully prepared sample. The advantage of using a TGA, which is a highly precise scale connected to a high-temperature furnace, is that no special sample preparation is necessary. Hence, the spherical particles can be analyzed before and after being charged in the experimental reactor.

An Arrhenius-type equation was chosen as the governing equation. It describes the change of concentration of a reactant in a sample that is exposed to a gradient of reactant concentration outside of the sample. In other words, it describes the reaction of a sample that is exposed to a change in atmosphere at its surface. In choosing this as the governing mechanism, the assumption must be made that the reaction of the sample and the reactant at the surface is much slower than the diffusion of the reactant into the bulk of the sample. Equation 2.4 is used as the governing equation of the kinetics model.

$$\frac{de_p}{dt} = A_0 e^{-\frac{E_\alpha}{RT}} \left(e_{p,eq}(T, P_{O_2}) - e_p(t)\right) \tag{2.4}$$

Here, the change in oxygen concentration is given by $\frac{de_p}{dt}$. The expression $e_{p,eq}(T, P_{O_2})$ represents the oxygen concentration in the material at the given conditions of temperature and oxygen partial pressure in the atmosphere. The value is calculated from the comprehensive thermodynamic model developed and published by Bo et al. [33]. $e_p(t)$ is the current oxygen concentration in the material. The Arrhenius expression on the right hand side of the equation includes the gas constant R and the temperature T as well as two constants, A_0 (Arrhenius constant) and E_α (activation energy). Those two constants are fitted using the TGA relaxation experiments.

The model is validated with reaction data from randomized TGA experiments. In these experiments, three different sized samples (1 mm, 3 mm, and 5 mm diameter spherical samples) are fully oxidized and then exposed to random atmospheres for random times until they are fully reduced. Afterwards, they are fully oxidized again. The model is able to accurately predict these experiments as shown in Figure 2.5. The accuracy of the model for the differently sized samples shows that the assumption of very fast bulk diffusion is correct. If the bulk diffusion had an impact on the reaction kinetics, the model would perform worse for the larger samples which is not the case.

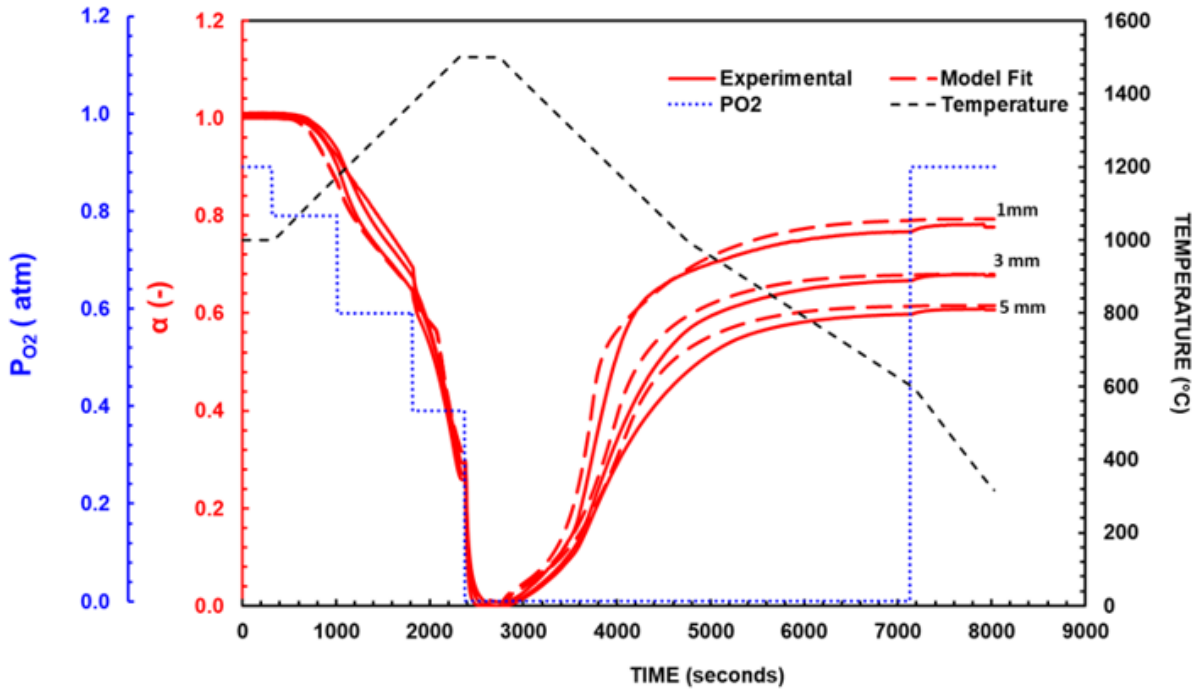

Figure 2.5 **Validation of Kinetic Model** The model (dashed red line) follows the experimental TGA data (solid red line) closely and accurately predicts the state of the sample at the end of the validation experiment. Three different sample sizes were produced and tested to prove the assumption that the bulk diffusion is irrelevant for the kinetics. Reproduced with permission from [29]. Copyright 2022 Joule.

2.4 Conclusions of Chemistry Considerations

The physics and chemistry of the material have been studied in light of a recent push to use MgMnO as an energy storage material. The high energy density, reaction temperatures and cyclability make it a desirable candidate for renewable energy storage. The chemical kinetics model developed is used in all simulation efforts that try to model the reactors using MgMnO as an energy storage material. It is often referred to throughout this thesis. The chemistry presented in this chapter is referred to similarly in the following chapters that explain the novel reactor concept and show numerical and experimental efforts towards charging the material efficiently.

CHAPTER 3

EXPERIMENTAL REACTOR DESIGN

After producing a pelletized energy storage material, the next goal was to build and use a lab-scale reactor for reducing the material. This chapter shows the steps taken and the lessons learned on the path to demonstrating the potential of a counter-flow moving bed charging reactor.

Considerable research has gone and continues to go into the manipulation of movement of particulate materials. Entire journals like Powder Technology are dedicated to this branch of process engineering. Despite many great advances in the field of high temperature packed bed flow in the past, this TCES reactor concept aimed at breaking a proverbial sound-barrier in packed bed flow experiments. Previous research by the Sandia national laboratory in the US and the German DLR set the benchmark for high temperature particle flows around 700-900°C [42, 43]. Both projects were geared towards heating particles to high temperatures by flowing them through a CSP cavity.

As previously mentioned, the MgMnO reduction (charging the particles) happens at temperatures >1400 °C which was an ambitious goal compared to the published state of the art for temperatures of moving particle reactors of <1000 °C.

3.1 The Idea of the Counterflow

An obvious issue with reaction temperatures of up to 1500 °C is that few materials are able to withstand prolonged exposure to these conditions. Fortunately, there are ceramics that have impressive properties even at these high temperatures. However, manufacturing and tolerances of ceramics such as zirconia (ZrO_2) and alumina (Al_2O_3) are much less desirable than those of metals [44]. Furthermore, as explained in Section 1.1, the sensible heat of the reactants accounts for a large portion of the total energy and must be recuperated to achieve high efficiency. So for the material selection and the a higher efficiency, it is beneficial to keep the heat in the center of the reactor. As stated before, the central innovation of the SoFuel project is the counter-flow principle of the high temperature reactor. The benefits of this idea will be explained here.

Some of the biggest innovations in the history of the modern world were impactful because

of their simplicity. The simple step of automating looms to weave fabrics more easily was a core driver of the industrial revolution in England and the conceptually small step of improving the steam engine by burning a liquid fuel inside the cylinder rather than burning coal and transferring the energy via steam are two examples of conceptually small changes to existing technologies that changed industries and the world.

To understand the simplicity of the novel approach of the high temperature counter-flowing moving bed reactor, the principle of operation will be explained in detail. Figure 3.1 visualizes the different steps explained here. The material releases oxygen at temperatures >1400 °C in an oxygen depleted atmosphere. This means that merely heating the particles up to very high temperatures is not enough to charge them as the released oxygen would quickly enrich the atmosphere and stop the reaction before the material is fully charged (reduced). Hence a continuous flow of an inert gas is necessary to maintain the atmosphere that keeps the reactants wanting to release more of their oxygen. To facilitate this reaction, a reactor with a moving bed operating principle was chosen. This makes the concept highly scalable and flexible when it comes to storing as much renewable energy as is available. With the particles moving through the reactor there are two options for flowing the inert gas: co-currently or counter-currently to the particles. The obvious choice is to flow counter-currently because then the gas flow that is necessary for the reaction can be used to solve another problem: the big temperature difference between the reduction temperature and the storage temperature.

Refer to Figure 3.2 for the temperature profile and the three different zones in the reactor tube. For ease of visualization, the reactor is shown horizontally while the tube would usually be installed vertically. The elegance and simplicity mentioned above becomes obvious when one follows the particle and gas flows through the reactor tube. The discharged (oxidized) particles are loaded into a hopper at room temperature. The hopper feeds the particles into the ceramic reactor tube where they enter the Recuperation Zone A and flow down towards the high temperature reduction zone B (in Figure 3.2, they enter on the right and flow to the left, following the black arrow).

As the particles get closer to the heated Reduction Zone B, they come in contact with the warm

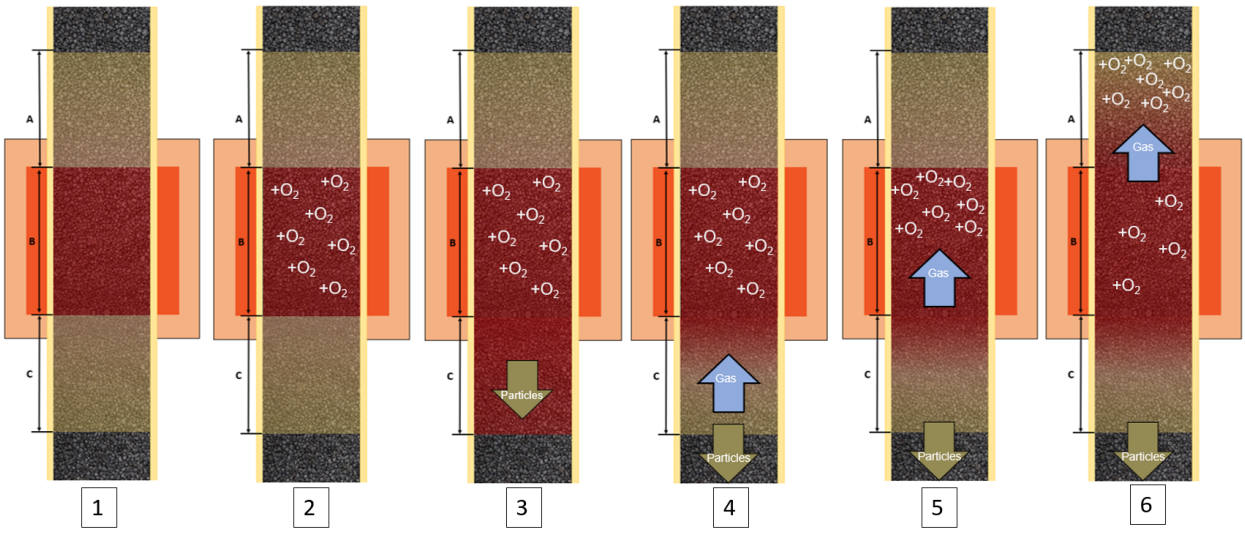

Figure 3.1 **Counterflow Concept** Schematics visualizing the counterflow principle. The reactor is heated up, causing the material to release oxygen. When the material bed is moved down, it carries sensible heat down into Zone C. In order to cool down the particles, gas is pushed through the reactor. The gas quenches the particles in Zone C, pushes the released oxygen up and out of the reactor and pre-heats the particles in Zone A.

gas exiting the reduction zone and interstitial heat transfer heats the particles up while cooling down the gas. The opposite process happens in the Quenching Zone C below the reduction zone. Here, the hot particles exit and are cooled down by the gas while the gas heats up. Figure 3.1 shows a step by step schematics of the recuperation gas flow.

The two mass flows can be matched such that almost all the heat is contained in the reduction zone. The sensible heat moving out of the reactor can be described by Equation 3.1 where $\dot{Q}_{solid}$ is the sensible heat of the stream in kW, $\dot{m}_{solid}$ is the mass flow rate of the particles in kg/s, $c_{p,solid}$ is the specific heat of the particles in kJ/(kgK) and the temperature difference is around 1450 °C.

$$\dot{Q}_{solid} = \dot{m}_{solid} c_{p,solid} (T_2 - T_1) = \dot{m}_{solid} c_{p,solid} \Delta T \tag{3.1}$$

This equation can be used to demonstrate the importance of recuperating the sensible heat of the particles. Taking an example from a later chapter, where a flow rate of 2.5 g/s of the energy storage material at a furnace temperature of 1500 °C was demonstrated, we find that the sensible heat in the moving particles is

$$\dot{Q}_{solid} = 0.0025 \frac{kg}{s} * 0.95 \frac{kJ}{kgK} * 1475K = 3.5kW \tag{3.2}$$

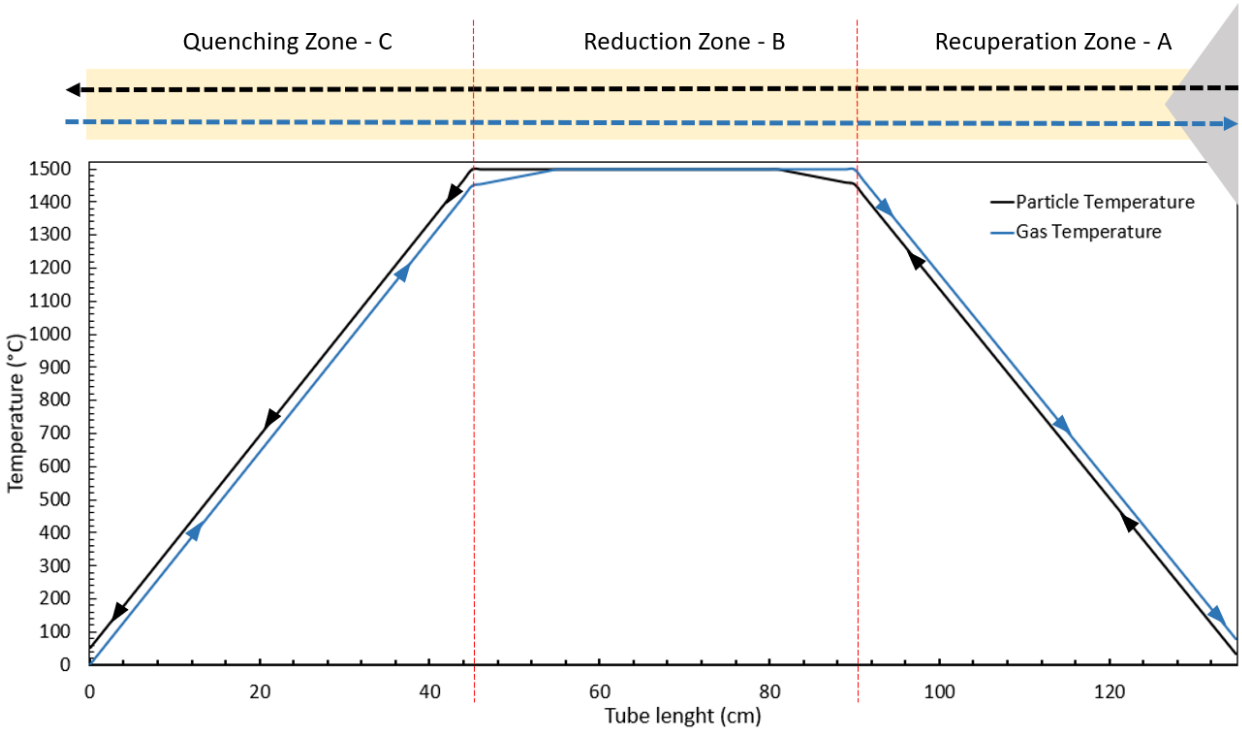

Figure 3.2 **Particle vs Gas Temperature** The particle and gas temperature through the reactor tube in a counter-flowing scheme. The tube is shown above the graph, particle flow and temperature are in black and gas flow direction and temperature in blue. The red dashed lines indicate the position of the heated reduction zone.

A particle flow rate of 2.5 g/s results in a chemical energy storage rate of approximately 2 kW. Not recovering the sensible heat of 3.5 kW would mean that the reactor would be unable to achieve a thermal efficiency over 40% because a majority of the energy provided to the material in the reactor would be lost as waste heat to the environment.

In order to recuperate all of the sensible heat, the heat of the particles flowing down needs to be equal to the amount of heat of the gas flowing up.

$$\dot{Q}_{solid} = \dot{Q}_{gas} \tag{3.3}$$

Since both mass flows are around room temperature at the bottom and around 1500 °C at the reduction zone, the temperature difference is equal.

$$\Delta T_{solid} = \Delta T_{gas} \tag{3.4}$$

Therefore Equation 3.5 describes the relationship of the two mass flows needed to recuperate the maximal sensible heat.

$$\dot{m}_{solid} c_{p,solid} = \dot{m}_{gas} c_{p,gas} \tag{3.5}$$

As mentioned in Chapter 2, the heat capacity of the material is approximately 0.95 kJ/(kgK). For nitrogen, the thermodynamic properties are much more well-known. The heat capacity depends on the temperature of the gas. It ranges from 1.04 kJ/(kgK) at ambient conditions to 1.25 kJ/(kgK) at 1500 °C [45]. The resulting mass ratio required for heat recuperation is approximately $1.045 \frac{g_{MgMnO}}{g_{N_2}}$.

To summarize, the gas that is needed to provide the oxygen depleted atmosphere also takes the heat of the particles that are charged and puts it into the particles that are about to be charged. This means that all mass flows into and out of the reactor are close to room temperature and there is very low sensible heat loss. Therefore, a system that is sufficiently big and well insulated has the potential of storing the vast majority of the heat that is put into it as chemical potential. High efficiency is of great importance as a lower storage efficiency would mean that a facility of the same output would need to be bigger and therefore more expensive.

Apart from the increase in efficiency, handling relatively cool mass streams is much easier than handling very hot ones so the counter-flow approach is universally beneficial. The main disadvantage will be discussed in Chapter 4. It evolves around the inertial forces of the upward flowing gas on the particles overcoming the gravitational forces on the particles, effectively stopping the flow of particles.

The following section will introduce the scheme used to control the movement of the particle bed while facilitating a counter-current flow of the heat recuperation gas.

3.2 Bed Flow Control

Figure 1.5 shows the SoFuel reduction reactor design. Central part is the ceramic tube running through the setup containing the packed particle bed. Controlling the particle flow of the column is achieved by letting particles exit the tube at the bottom. This creates a cavity that is filled by the particles above it, allowing all particles to move down. The amount of particles pushed out over

time constitutes the solid mass flow of particles. This mass flow needs to be controlled precisely since the heat recuperation principle is based on matching the mass flow rates.

There are a number of particulate flow controllers available, most of which work by physically restricting an orifice through which particles escape. Augers and an oscillating gate that closes the particle exit hole for a short amount of time were tested as candidates for particle flow controllers. A disadvantage of both methods is the physical movement of parts of the assembly. The tests revealed that both methods resulted in abrasion of both the particles and the valves.

Some systems work on blowing particles out of a horizontal hole with compressed air. These l-valves are traditionally used for high volume flows [46]. The experimental charging reactor was designed to target precisely controlled, low flow rates around 0.5-3 g/s. Through experimentation it was found that high-velocity gas pulses worked well to control a wide variety of flow rates in an l-valve. The novel particle flow controller that was conceptualized and build from those tests is shown in Figure 3.3. It consists of the pulsing l-valve, a catch can, and a load cell.

The l-valve had to be designed to allow no particle flow when the gas pulsing was off. This serves as a fail-safe and prevents the hot particle bed from accidentally discharging into the collection tank. Since the l-valve is mounted at the bottom of the particle bed, the dimensions need to be appropriate to prevent unwanted particle movement. This was done by investigating the angle of repose of the bulk particles [47].

When particles are expelled from the l-valve (2) in Figure 3.3, they land in the catch-can (3), which is suspended in the collection tank via a load-cell (4). The catch can has a capacity of about 1.5 kg of particles and is equipped with a pneumatic dump valve to empty the caught particles into the bottom of the collection tank. This design allows for the use of a precise, low-capacity load-cell which is elemental for precise control of the particle flow. The load-cell signal is processed by a LabView VI that compares the change in mass per time interval with the calculated set-point and increases, decreases, or stops the l-valve gas pulsation amplitude to achieve the flow-rate set-point. This amplitude change is realized via a flow-controller (6) that is pulsing with a set frequency and changing amplitude.

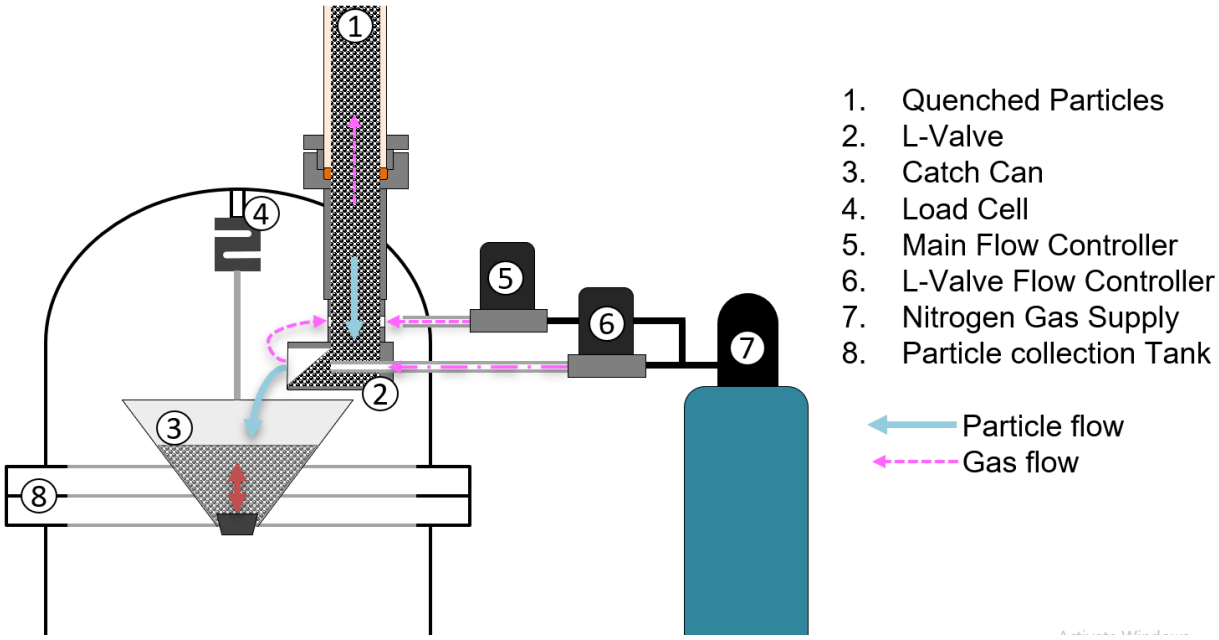

Figure 3.3 **L-Valve Schematics** Schematics of the solid and gas flow controls. The pulsing l-valve is installed at the bottom of the particle column and acts as a flow restriction. A pulsed flow that is set by a computer connected to a flow controller ejects small amounts of particles per pulse and enables a precise flow of the bed with minimal particle attrition in the valve. The closed particle collection tank ensures that the gas moves up through the particle bed.

The l-valve uses very little gas to control the solid flow rate. Hence, a second flow controller is connected to the nitrogen gas supply and provides the nitrogen mass flow required for full heat recuperation. To prevent this gas from interfering with the l-valve operation, the tube above the l-valve is meshed to allow the nitrogen to enter the tube and flow up towards the top. The entire system is encased in a pressure vessel to force the gas up through the bed.

Figure 3.4 shows a section of measured mass data from an experimental run. A straight line (orange) is included for the reader's convenience to visualize the slope of mass gain that the controller was set to. It can be seen that the blue measured mass gain only differs on some occasions, but that the controller corrects divergence from the set-point and the gradients of both curves are identical.

3.3 Reactor Tube and Heating

With very high temperatures of >1400 °C the material choices for the reactor tube containing the particles and going through the reactor are limited. Most metals are liquid or approach a phase

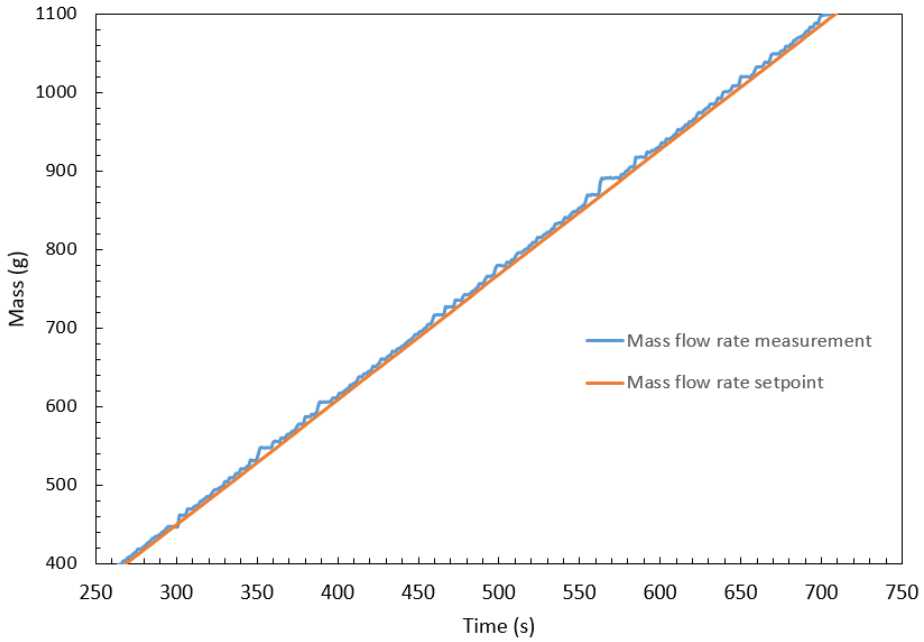

Figure 3.4 **L-Valve Flow** Mass measurement from a reduction experiment (all data shown in Figure 5.4). During this section of the experiment, the flow rate setpoint was 0.75 g/s (see orange line). Despite a few small clogs, the l-valve control is able to follow the setpoint very closely.

change at those temperatures and are hence disqualified. However, decreased tensile strength and stiffness are not the only challenges that the materials face at high temperatures in the reactor. They must also be inert and cannot react with the energy storage material or the oxygen that is released. At such high temperatures, even some inert ceramics start to oxidize [48]. Other material requirements are good heat conduction and abrasion resistance. Out of the materials that were considered, Aluminium Oxide (or alumina, Al_2O_3) was chosen for its excellent strength and inertness at high temperatures as well as the high melting point. All alumina tubes used in experiments were purchased through AdValue Technology.

To heat the reactor and provide the energy for the reduction of particles, a SentroTech STT-1700-12 vertical tube furnace with a 305 mm heated length was purchased and installed with the alumina tube running through it. The installation required the removal of the furnace cavity from the original stand and fabrication of a frame holding the cavity and the particle collection tank as well as the reactor tube. Figure 3.5 shows the frame, furnace, collection tank, and tube on the left and the setup with instrumentation on the right.

Figure 3.5 **Assembly of the Reduction Reactor** Left: The main components of the bigger experimental reduction reactor in a first mock-up installation: The modified pressure tank containing the particle control system, the high-temperature furnace and the alumina tube. Right: The system is wired up to the furnace, gas flow meters and thermocouples.

3.4 Particle Flowability

As mentioned in Section 2.2, it was decided to synthesize particles with a diameter of 1 mm for the first trials. Using these particles in a smaller test reactor shown in Figure 3.6 proved that the l-valve was an effective and precise particle flow controller and the sensible heat recuperation via the inert gas worked as expected. Exit temperatures of gas and particles were measured below 200 °C in first trials at lower temperatures. Flowing the particles through the reduction zone proved difficult, as expected, and was one of the main challenges throughout the project. The small particles got stuck in the reduction zone during the first trials at lower temperatures. The particles

were found to consistently clog around 1200 °C during experiments where the temperature of the furnace was slowly increased while continuously running the particle bed and counter-flow gas.

In order to rule out that the reduction reaction and the resulting mass change was the reason for the clogging, the reactive MgMnO particles were replaced with inert 1 mm diameter porous alumina spheres. These particles similarly clogged in the typical way: The particles in the reduction zone seize and block the movement of the bed downwards. The particles below the clog are able to move down, creating a cavity underneath the clog. Due to the lack of downward bed movement in the Recuperation Zone A, the zone overheats as the gas carries the heat of the charged particles up into that zone. The moving bed clogs due to two main mechanisms:

- Particle to particle attrition and particle to wall attrition, which is governed by the contact points between the particles.
- Expansion clogging, which is caused by cold particles entering the Reaction Zone B with insufficient preheating. The result is a rapid temperature change and thermal expansion of the particles which can cause the bed to lock up.

The two mechanisms often compound each other. When the particles clog in the reduction zone for some time (2-5 minutes), it can happend that the clog slides down into the now empty quenching zone. In turn, this causes particles from the recuperation zone to rush into the reactor where they heat up quickly and cause an expansion clog. Figure 3.7 shows a clog that slid down into the quenching zone and Figure 3.8 is a picture from a reactor tube inspection. The empty tube has particles stuck to the wall which is a sign of an expansion clog.

Figure 3.6 shows the result of a clog in the first test reactor built for 1 mm particles. The clog had formed minutes before undetected and so the Quenching Zone C was empty as no more particles were in the tube underneath the clog. The glowing in the picture comes from hot particles breaking off of the clog and falling down the alumina tube into the l-valve. The temperature shock caused by hot particles falling down into the quenching zone or the sliding of a big conglomeration of hot particles has caused tube fractures and l-valve issues on more than one occasion.

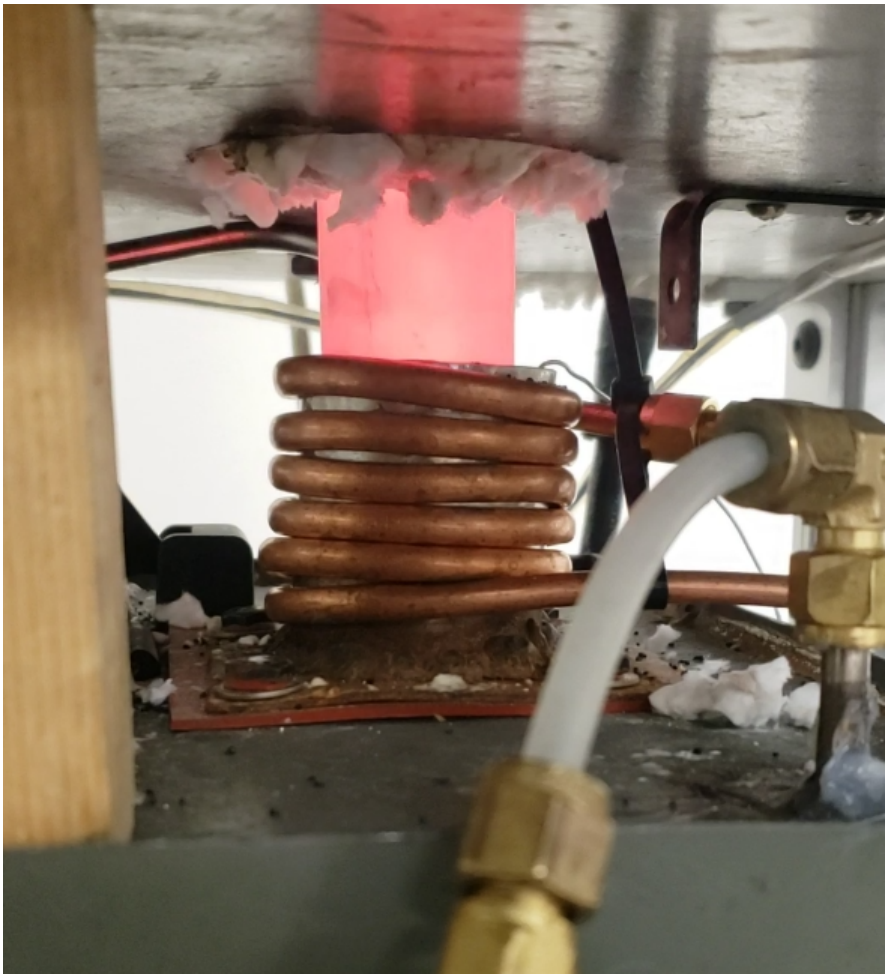

Figure 3.6 **1 mm Particle Clog** The first test setup consisted of a small pressure chamber and a 20 mm diameter alumina tube. Shown here is the result of a clog at around 1200 °C. The particles in the quenching zone flow down into the particle collection tank but the clog stops particles from flowing through the reduction zone, leaving the quenching zone empty. The glow in the picture comes from hot particles falling down which causes damage to the system.

The struggles with flowing inert particles showed that high contact area, caused by the small particle size was stopping the bed from moving beyond temperatures of 1200 °C

A bigger reactor was designed and built to investigate the hypothesis of improved flowability with bigger particles. This purpose-built reactor shown in Figure 3.5 accomplished a major milestone when it successfully flowed a bed of 3 mm diameter inert alumina spheres at 1500 °C. The reactor has longer recuperation and quenching zones to allow sufficient time for heat transfer between the particles and the gas as well as a longer reduction zone for increased residence time (see Section 3.3).

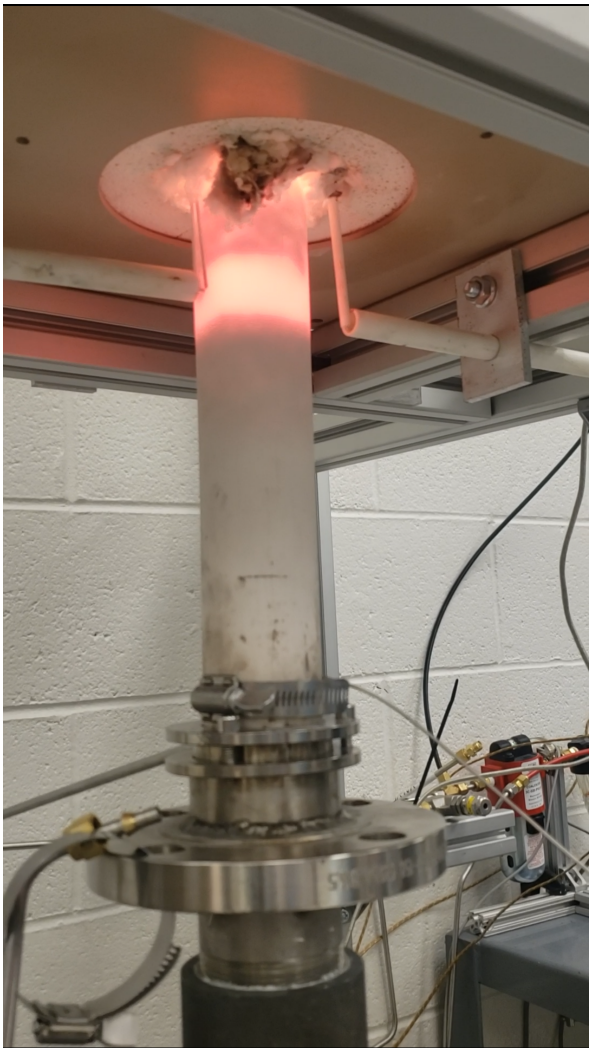

Figure 3.7 **3.5 mm Particle Clog** Clog in the main setup using 3.5 mm particles at 1450 °C. The clog slid down from the reduction zone into the quenching zone. As the particles cool down, the clog starts breaking apart.

Replacing the inert spheres with 3.5 mm diameter MgMnO particles yielded a first high-temperature moving bed success with the energy storage material. Once it was established that the particles are able to flow at high temperatures, an extensive experimental campaign was started to determine the capabilities of the system.

3.5 Experimental Procedure

To quantify the effectiveness of a given experiment, a new metric was established: chemical energy storage flux. Q_{chem} is defined as the amount of chemical potential (stored power) exiting the reactor at a given time. The unit is $[Q_{chem}] = \frac{kW}{m^2}$.

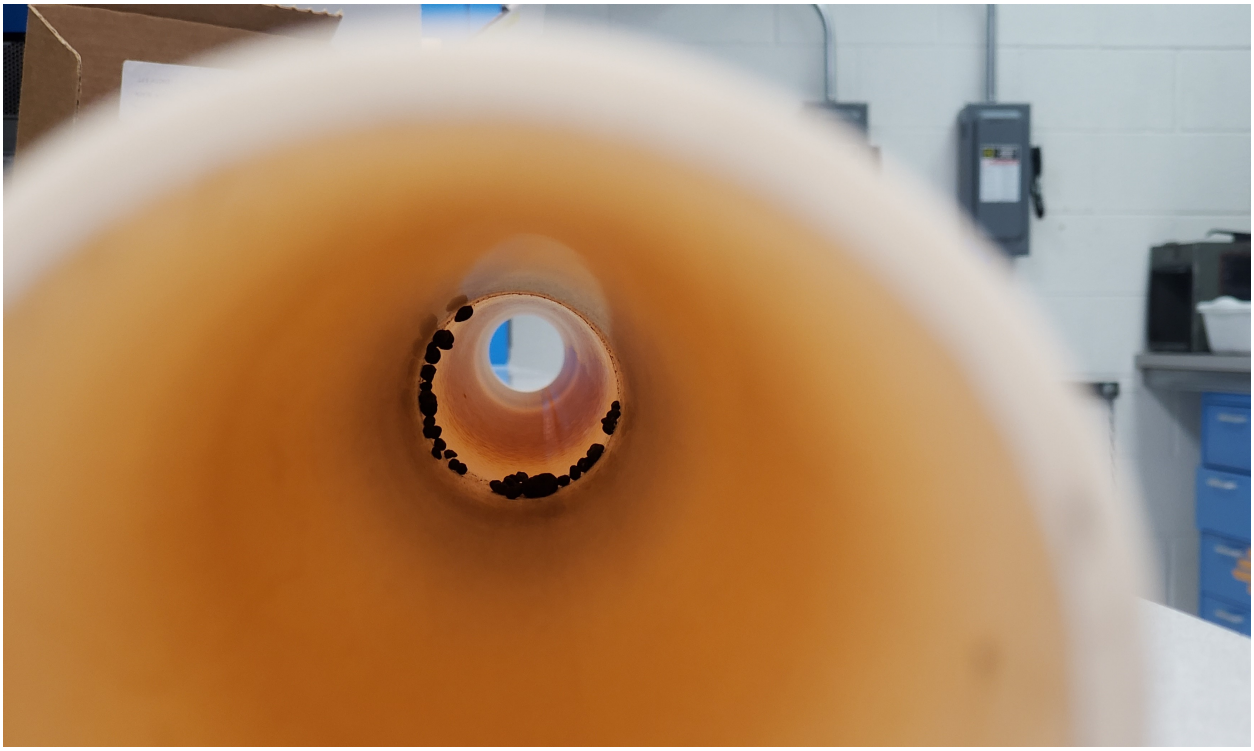

Figure 3.8 **Wall Attrition** Reactor tube removal and inspection shows particles stuck to the wall, causing a clog. The location of the particles is at the beginning of the reduction zone where the tube enters the furnace cavity. This suggests that the particles were insufficiently preheated and expanded upon rapid temperature increase, causing particles to stick to the wall.

To calculate Q_{chem} for any experiment, the average oxygen flow rate needs to be known. The experimental setup uses an AMI 201LC oxygen analyzer to record the oxygen percentage of the exhausted gas. This value needs to be multiplied with the reaction enthalpy of the reduction reaction. From those values, the particle bed energy storage power or the chemical potential flux is calculated:

$$P = \frac{\dot{V}_{O2}}{60 V_m} \Delta H_f [kW] \tag{3.6}$$

Here, $\dot{V}_{O2}$ is the measured volumetric flow rate of oxygen in standard liters per minute (SLPM). V_m is the molar volume of Oxygen (which is 22.4 L/mol at standard conditions, same as for every gas derived from the ideal gas law). ΔH_f is the enthalpy of formation which is $346 \frac{kW}{mol_{O_2}}$ for the MgMnO particles [33]. Q_{chem} is calculated by dividing the storage power P by the cross-sectional

area of the reactor tube A_{tube}.

$$Q_{chem} = \frac{P}{A_{tube}} \tag{3.7}$$

Q_{chem} is an effective metric because it can be calculated from the experimental oxygen data with Equation 3.7 and validated by analyzing the particles after a run using a TGA. A TGA is a highly accurate scale that has a high-temperature furnace to heat samples up while weighing them. It is also equipped with precise flow meters and can control the atmosphere in the furnace. We use a Netsch STA 449F5 Jupiter TGA. Three reduced samples are taken from the bed and are oxidized under 1000 °C and 0.9 atm oxygen in the TGA. The change in weight is monitored as the material absorbs oxygen in the atmosphere. The extent of reduction e_p can be determined from the measured weight gain. e_p can be used as an indicator of how charged the particles are after a reduction run. This can be used to compare the chemical efficiency of different experiments.

$$e_p = \frac{\Delta m}{(\Delta m + m_{initial})\beta_{red}} \tag{3.8}$$

here, Δm is the measured mass of oxygen that was absorbed by the samples (recorded by the TGA). β_{red} is a dimensionless number unique to the material and the reduction:

$$\beta_{red} = \frac{m_{1000°C,0.9atm} - m_{1500°C,0.01atm}}{m_{1000°C,0.9atm}} = 0.0698 \tag{3.9}$$

this dimensionless number describes the ratio between the total possible difference in mass of a fully oxidized and a fully reduced sample and the fully oxidized state of that sample from the thermodynamic investigation published by Bo et al. [29, 33].

Samples are taken before and after the reduction. Using the TGA analysis, the chemical state of the particles before and after the experiment is determined. With data of both states, the exact amount of oxygen released during the reduction experiment can be calculated. An average value of three analyzed samples is then extrapolated to the entire bed and compared to the measured oxygen in the exhausted gas to validate the oxygen sensor and data taken during the experiment.

In order to have repeatable and reliable results, a standard procedure was implemented that ensured flowability when operating the reduction reactor. Starting with an empty reactor tube,

oxidized particles are filled in the tube from the top using a hopper while the system is at ambient temperature. The furnace temperature is then increased from ambient to 1000 °C using an increase of +5 °C per minute while the particle bed is at rest. When the furnace is heated up to 1000 °C, the particle bed is set in motion and moves downward at a rate of 0.75 g/s. It was found that bed movement was required during the temperature increase from 1000 °C to the targeted reduction temperature. A stationary bed at temperatures beyond 1000 °C lead to expansion clogging and a resulting seizure of the bed.

To prevent damage from overheating to any of the components, the counter-flowing gas is always turned on when the particles are moving. This keeps the heat in the reduction zone. When the reactor temperature exceeds 1350 °C, the solid flow rate is increased to the faster targeted flow rate. The reactor continues to heat up to the experimental temperature between 1400 °C and 1500 °C. When the furnace reaches the target temperature, the experimental conditions are kept at steady state for at least 60 minutes or until the oxidized particles have run out. After the steady state portion of the experiment, the particle and gas flows are halted. The furnace is cooled down with a ramp rate of -5°C per minute. Samples can be extracted from the sample extraction port (see (9) in Figure 3.9).

To prepare the particles for a new reduction experiment, they are moved through the reactor in an oxidizing environment at a flow rate of 0.75 g/s at 1000 °C with a counter flow of air for two consecutive times. This ensures that the particles spend enough time in a favorable environment to be fully oxidized (discharged). This preparation is very time-consuming and takes about 10-15 hours which means that preparation and experiment take at least two to three days.

3.6 Fluidization Problems

Once a consistent experimental procedure was established, it was clear that the reactor worked better on low solid flow rates. There were no issues with bed clogging at solid flow rates <0.75 g/s. When running faster than that, the particle bed would stop flowing through the reduction zone. This was a big problem as the chemical energy storage flux Q_{chem} is very low for small solid flow rates. This is due to the fixed chemical potential of the particles. If the particles are being fully

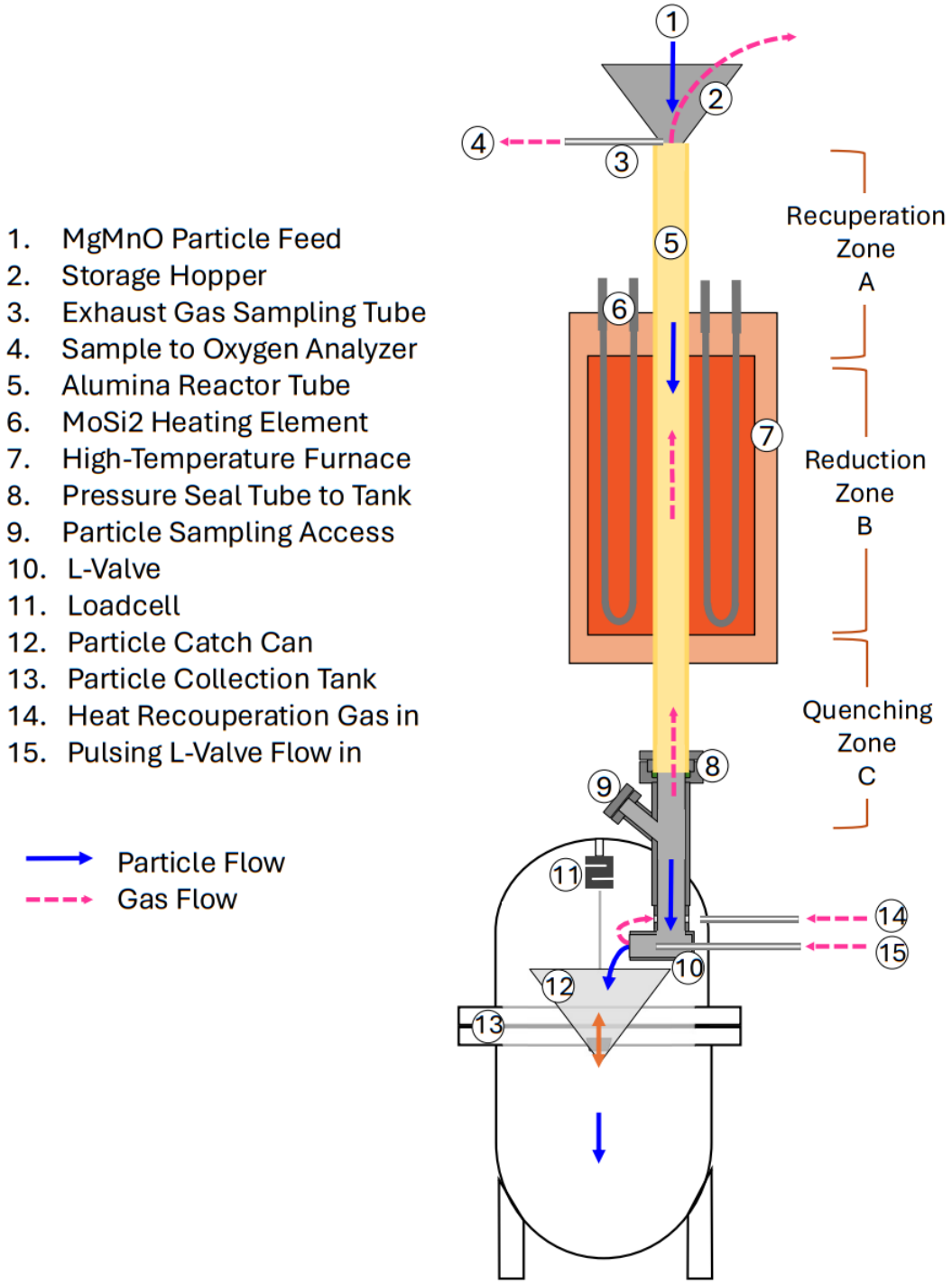

Figure 3.9 **Reduction Reactor Schematics** The schematics visualize the details of the reduction reactor, including the particle collection tank and control system, the reactor tube, and the furnace.

charged during reduction, Q_{chem} can only be further increased by increasing the mass flux of the particles through the reactor.

One consideration was that the bed was being fluidized by the counter-flowing gas needed to provide the sensible heat recuperation. Matching the heat capacity streams means that a higher solid flow rate of particles requires a higher flow rate of the gas. The problem identified was that as the gas density decreases at high temperatures of 1450 °C in the reduction zone, its velocity is significantly increased. Similarly, the viscosity of the gas increases at those temperatures [49]. As a result, inertial and viscous forces of the gas acting on the particles increase to a point where the gas fluidizes and lifts the particle bed, stopping the flow of particles.

The minimum fluidization velocity u_{mf} can be calculated using the dimensionless Archimedes number Ar. It describes the ratio of gravitational and viscous forces. To get the minimum fluidization velocity, a correlation between the Ar number and the Reynolds number at the onset of fluidization Re_{mf} is needed.

$$Ar = \frac{\rho_g d_p^3 (\rho_p - \rho_g) g}{\mu} \tag{3.10}$$

This is achieved using the gas density ρ_g, particle diameter d_p, particle density ρ_p, dynamic viscosity μ and gravitational acceleration g. Wen and Yu have proposed a correlation between the Archimedes number Ar and the Reynolds number at the onset of fluidization, Re_{mf}[50]:

$$Re_{mf} = \sqrt{33.7^2 + 0.0408 Ar} - 33.7 \tag{3.11}$$

With Re_{mf}, one can then calculate the velocity at the onset of fluidization:

$$u_{mf} = \frac{Re_{mf} \mu (1 - \epsilon)}{d_p \rho_g} \tag{3.12}$$

Figure 3.10 visualizes the onset of fluidization at various temperatures for different solid flow rates using correlation 3.11. The three lines represent the dimensionless ratio of gas mass flux over solid mass flux for a constant particle mass flux (0.75 g/s, 1 g/s, and 1.25 g/s) that causes fluidization. The solid horizontal line is the gas-to-solid mass flux ratio required for heat recuperation. The figure conveys that as temperatures increase, less gas flow is required to start fluidization. The intersection of the solid green line with the fluidization limit curves at a given solid flow rate indicates the temperature at which fluidization will occur within the reactor.

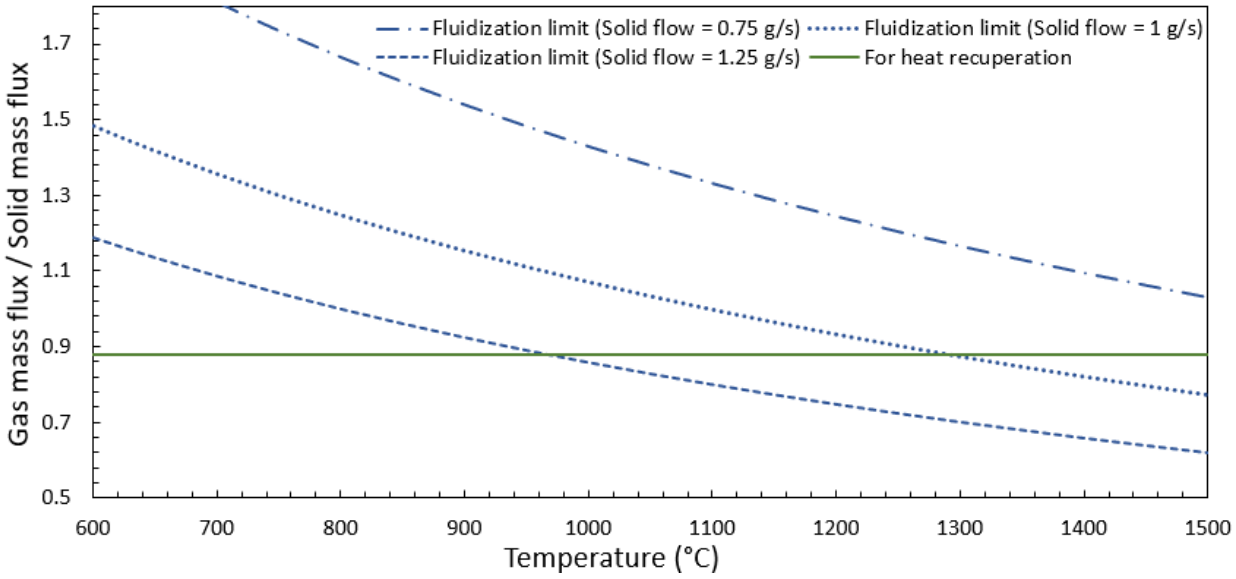

Figure 3.10 **Fluidization Limit Nitrogen** Theoretical fluidization onset for different ratios of nitrogen gas and MgMnO particle flow rates at increasing temperature. It can be observed that the recuperation principle induces fluidization at high temperatures above solid flow rates of 0.75 g/s which explains flowability issues at higher particle flow rates.

As can be observed, the bed may start fluidization above temperatures of 950 °C for a solid flow rate of 1.25 g/s. The ratio of gas to solids is calculated using the specific heat of both streams and the masses, compare Equation 3.5. These fluidization calculations validate the hypothesis of fluidization stopping the solid flow through the reactor. They match the experimental observations where a solid flow rate of 0.75 g/s was the maximum flow rate achievable.

The first solution to the bed fluidization problems at high temperatures was achieved by pulsing the recuperative gas flow. This enabled a batch flow through the reaction zone where the bed lifts during the recuperation phase of the pulse. When the recuperation flow is pulsed off, the particle bed moves downward through the reactor tube. An optimization of the frequency, amplitude, and duty cycle of the pulsing was required to achieve flow and heat recuperation using the pulsed recuperation flow.

3.7 First Charging Success

The pulsing gas method allowed for an increase of the particle mass flow rate while maintaining full recuperation of the sensible heat. Data from a successful run at 1.25 g/s are shown in Figure 3.11. As per the standard experimental procedure, the reactor filled with particles was heated up

to 1000 °C, then the bed flow and the counter-flowing gas was started at 0.75 g/s as the furnace continues to heat up to the target temperature of 1450 °C. The particle flow rate is increased to the target flow rate of 1.25 g/s, causing a change in the slope of the green mass curve. Note how initially the oxygen sensor (red line) confirms very low oxygen partial pressure in the gas exiting the reactor. As the temperature increases, the material slowly starts releasing oxygen until at 1450 °C the oxygen signal is at a steady 6 %. Using equations 3.7 and 3.6 gives a storage flux of $Q_{chem} = 455 kW/m^2$. Note that the gas temperatures at the inlet and outlet of the tube are below 100°C, showing that the heat recuperation works as designed by keeping both ends of the reactor around ambient conditions while the center is at reduction temperatures of 1450°C.

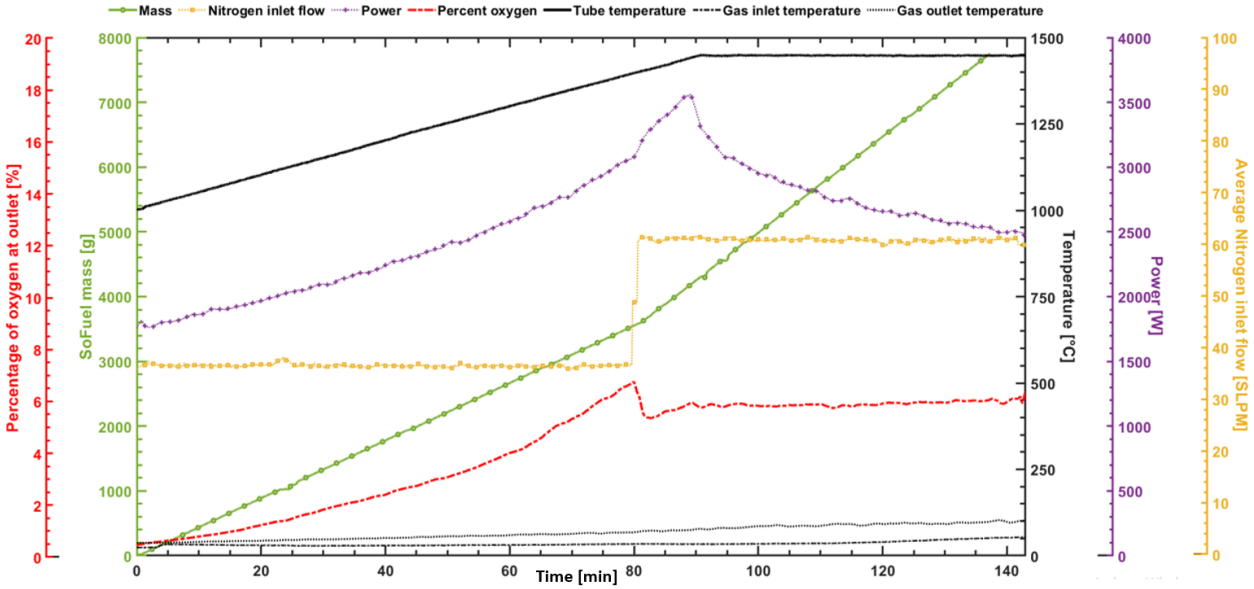

Figure 3.11 **Experimental Data 1.25 g/s run** Experimental data from a run using the pulsed counter-flow concept. The particle flow rate was increased from 0.75 g/s to the target flow rate of 1.25 g/s as evident in the change in gradient in the green line (per standard experimental procedure, refer to Section 3.5). The furnace temperature was increased to 1450 °C and the storage flux Q_{chem} reached 455 kW/m^2. Reproduced with permission from [51]. Copyright 2023 American Chemical Society.

3.8 Summary of the Experimental Reactor Design

This chapter explained the reactor concept and introduced the experimental reactor as well as first experimental successes. The counter-current flow scheme enables high sensible heat recuperation

and promises high thermal efficiencies. These first results prove the viability of the concept. They show that the new energy storage medium MgMnO can be continuously thermo-chemically charged using a moving bed reactor with full heat recuperation using a counter-currently flowing gas.

In order to be competitive, the chemical energy storage rate needs to be increased. A Q_{chem} of around 1.2 MW/m^2 was set as a target that could prove this concept as a contender for large-scale energy storage. The following chapters show the steps taken to achieve a peak Q_{chem} of 1.2 MW/m^2.

CHAPTER 4

INCREASING THE SOLID FLOW RATE

Materials in this chapter are an extension of the work reported in [51]. This chapter introduces improvements to the experimental reactor that allow a higher mass flow rate of MgMnO.

4.1 Overcoming the Fluidization Problem

Chapter 3 explains the problem that the recuperative gas flow starts to fluidize the bed at higher flow rates and temperatures. A solution was needed that would enable higher mass flow rates while maintaining the sensible heat recuperation.

An observation of the counter-flowing gas recuperation mechanism lead to a promising idea. The gas serves a different purpose in each of the zones (see Figure 3.9 for zones). The particles enter the reactor at the top and flow down towards the reaction zone. They enter the Recuperation Zone (A) where they are heated up by the hot gas flowing up out of the reduction zone. When they enter the Reduction Zone (B), they start to reduce and release oxygen. The sweep gas picks up the released oxygen and carries it out of the reactor, maintaining a low oxygen partial pressure for the reduction. As the particles travel down out of Zone B, the cold gas that enters the system through the particle collection tank and flows upwards quenches the particles. The sensible heat that the gas picks up in Zone C is transferred to the fresh particles in Zone A.

The bed lifting caused by high gas velocities happens in Zone B. This is where the temperatures are the greatest. In this zone, a lower gas flow rate would be sufficient to sweep the released oxygen. The coupling of gas and solid flow is necessary in the recuperation and quenching zones only.

4.2 Gas Bypass to Solve Fluidization

To solve the problem, part of the gas needs to be bypassed through the reduction zone. This has the potential of ensuring bed flowability for higher solid flow rates. As mentioned, the gas is needed to maintain a low oxygen partial pressure in the reduction zone. This is because the reaction kinetics favor a low oxygen partial pressure atmosphere. Hence it is important to maintain some gas flux through Zone B to remove oxygen released by the particles during reduction.

Multiple methods of bypassing gas around the reduction zone were considered. Risks of leaks

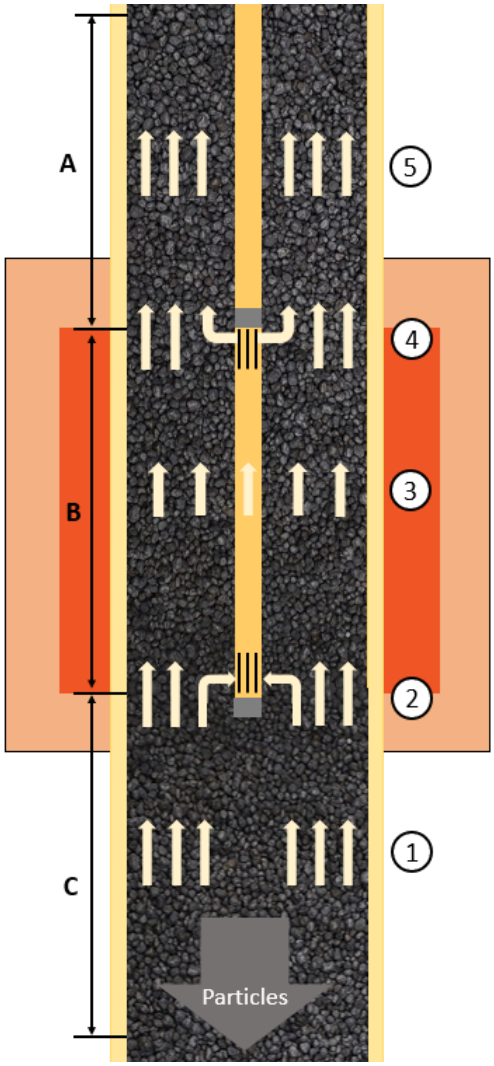

Figure 4.1 **Bypass schematics** A slotted alumina tube is installed in the reactor to allow some of the counter-flowing gas to bypass the bed. Particles flow downwards (grey) while gas flows upwards (orange). 1: Gas cools reduced particles in Zone C. 2: Gas enters reduction Zone B, some enters into bypass tube. 3: Gas moves through Zone B, some bypassing the bed through the bypass tube. 4: Gas exits Zone B, bypass gas re-enters the particle bed. 5: Gas preheats incoming particles in recuperation Zone A. Reproduced with permission from [51]. Copyright 2023 American Chemical Society.

and stress-induced cracks deterred any concepts that included having to alter the structural integrity of the reactor tube by drilling holes or slits to vent or bypass the gas. The only feasible way that prevented leaks or cracks in the reactor tube was an internal bypass mechanism. The schematics of the modification is shown in Figure 4.1 including a step by step visualization of the gas flow.

A 9.5 mm diameter Al_2O_3 tube is installed in the reactor. Figure 4.1 does not show that the

tube extends up beyond the hopper where particles are filled in and is secured to the frame above the hopper. This secures the vertical and radial position of the bypass tube. The inlet is made of 0.5 mm wide slits over the lenght of 4 mm. To prevent particles from entering the tube, the bottom hole is closed with alumina cement. The inlet slits are vertically situated in line with the bottom of the Reduction Zone B. The gas exits the bypass tube through similar slits made 305 mm above the inlet, at the upper end of Zone B. The tube acts as a parallel flow path to the particle bed. This parallel path has no obstructions compared to the pores in the particle bed. Part of the recuperation gas enters the tube and flows upwards. Since the tube is blocked above the exit slits, the gas is forced to join with the rest of the gas that went through the bed and has collected the released oxygen. Then, all the gas flows through the Zone A. As it encounters the cold incoming particles, interstitial heat transfer recuperates the sensible heat that the gas picked up in Zone C.

4.3 Experimental Validation

The previous maximum solid flow rate of 1.25 g/s in the reactor was achieved using the pulsing main flow technique, see Figure 3.11 in Chapter 3. The maximum chemical energy storage flux of $Q_{chem} = 455 kW/m^2$ (Equation 3.7) was deemed too low to warrant any investigation in scaling up the system.

To test the hypothesis of an internal bypass tube preventing fluidization and bed lifting, the bypass tube was installed in the reactor and several experimental runs were conducted. After initial troubles with the tube attachment, an increased solid flow rate of 2.5 g/s was achieved. The effect of the tube on the operations is a measurable pressure difference in the particle collection tank. This indicates that the moving bed has a higher pressure gradient without the tube compared to with the tube. Figure 4.2 shows pressure data from two similar experiments. The solid blue line shows the pressure peaks of the pulsing main flow averaging 100 SLPM nitrogen in the reactor prior to installing the bypass tube. The green dashed line shows the pulsing main flow at a higher 120 SLPM nitrogen flow rate with the bypass tube installed in the reactor. Despite the higher flow rate, the chamber pressure in the bypass experiment is much lower than in the experiment without the bypass tube. This shows how effective the bypass is at reducing the overall pressure gradient of

the moving bed reactor. The reduced pressure is caused by less gas interacting with particles on the way up through the reduction zone. This allows for higher flow rates before fluidization becomes an issue.

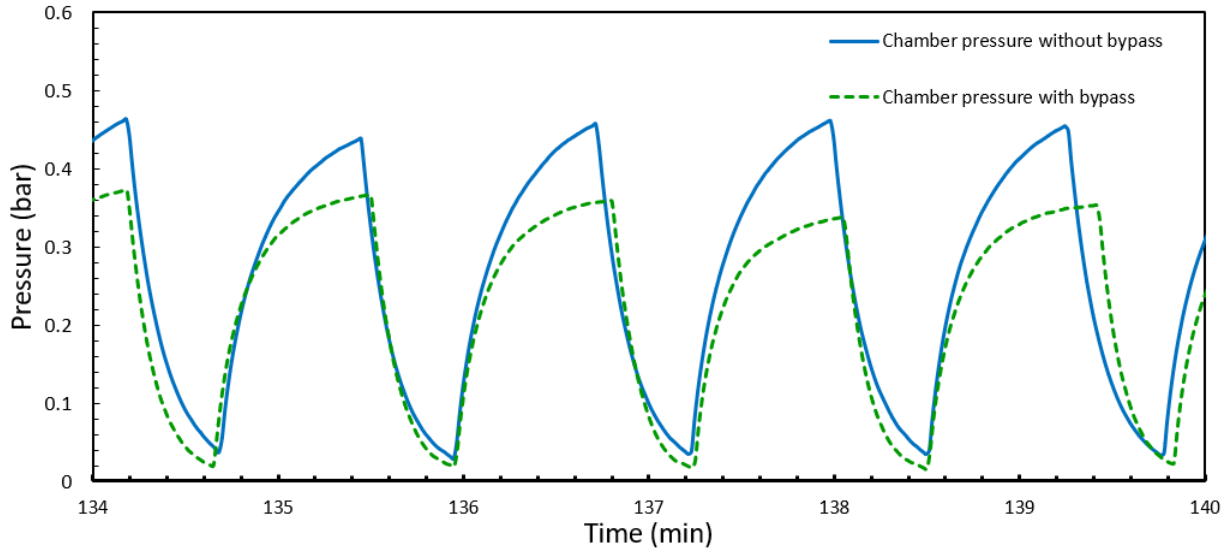

Figure 4.2 **Pressure Difference Bypass** The chamber pressure measurement shows the impact of the bypass tube on the pressure gradient. Both curves are taken from experiments at 1400 °C and nitrogen flow rates of 100 SLPM (without bypass, blue solid line) and 120 SLPM (with bypass, green dashed line). The data shows that the pressure in the chamber is lower despite a higher nitrogen input for the bypass experiment. This shows that the bypass tube reduces the pressure gradient across the particle bed. Reproduced with permission from [51]. Copyright 2023 American Chemical Society.

Experimental runs showed that the bypass tube enabled a doubling of the solid flow rate from 1.25 g/s as the maximum possible flow rate without a bypass tube to 2.5 g/s with a 9.5 mm diameter bypass tube inserted into the bed as shown in the schematics in Figure 4.1.

The baseline experiment with 1.25 g/s solid flow is shown in Figure 3.11 in Chapter 3. The recuperative gas flow rate was 60 SLPM and the reduction temperature was 1450°C. During reduction, the material released an average of 3.83 SLPM of oxygen which calculates to a $Q_{chem} = 455 kW/m^2$.

Figure 4.3 shows data from a run with the bypass tube. The solid flow rate of 2.5 g/s was matched with a pulsed recuperation gas flow of 120 SLPM. The oxygen flow rate increased to 4.63 SLPM which equates to $Q_{chem} = 670 kW/m^2$. This is lower than expected. Intuition suggests that

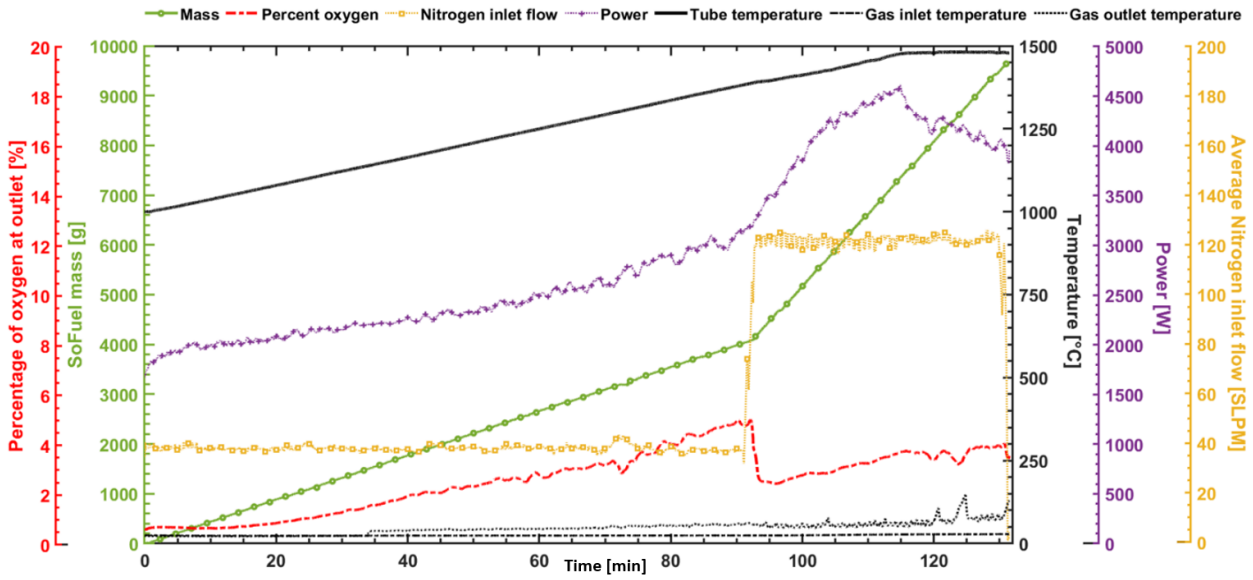

Figure 4.3 **Experimental Data 2.5 g/s Bypass Run** Experimental data from a run using the pulsed counter-flow concept with a bypass tube. The particle flow rate was increased from 0.75 g/s to the target flow rate of 2.5 g/s as evident in the change in gradient in the green line. The furnace temperature was increased to 1500 °C and the storage flux Q_{chem} reached 670 kW/m^2

doubling the particle mass flow rate would also double the chemical energy storage flux to around 900 kW/m^2.

4.4 Investigation of Low Chemical Energy Flux

The TGA analysis of the reduced samples, as described in Chapter 3, can be used to explain the difference in expected and found energy storage flux. Figure 4.4 shows the mass gain in percent of the starting sample weight of one of three samples for both experiments. The solid blue line represents the earlier experiment with a flow rate of 1.25 g/s, while the dashed green line was taken from the faster-flowing bypass experiment. Clearly, the 2.5 g/s particle sample did not absorb the same amount of oxygen during the oxidation in the TGA as the other samples.

The hypothesis is that the increased solid flow rate decreases the residence time of the particles in the reduction zone. At 2.5 g/s, the residence time of each particle in the 305 mm reduction zone calculates to about 8 minutes. This seems to be too short for full conversion, causing the particles to exit the reactor only partially reduced. Using the TGA results and Equation 3.8 one finds that the extend of reduction for the 1.25 g/s samples is $e_{p,1.25} = 0.92$ while the extend of reduction for the 2.5 g/s samples is $e_{p,1.25} = 0.83$.

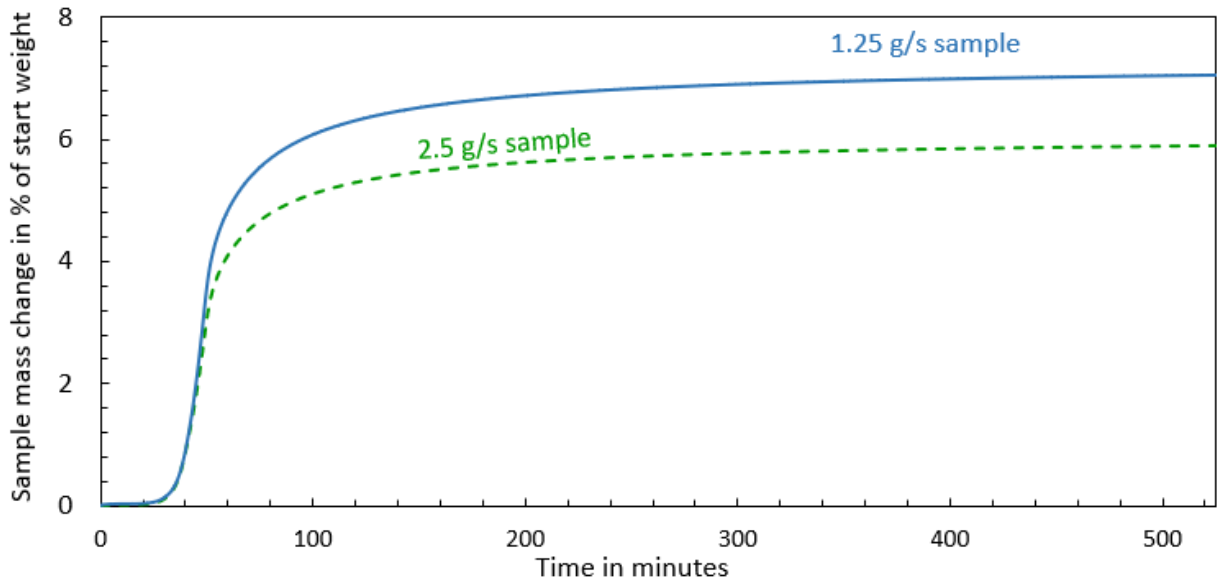

Figure 4.4 **TGA Sample Analysis** TGA data from oxidation analysis of two samples. The samples take from the 1.25 g/s show a greater mass change percentile compared to the samples taken from the 2.5 g/s run. Reproduced with permission from [51]. Copyright 2023 American Chemical Society.

The TGA data is shown in Table 4.1 The lower average mass change for the 2.5 g/s samples when the samples are oxidized shows the lower conversion during the experiment.

This data indicates that while the bypass tube overcomes the issues with fluidization and enables higher solid flow rates through the reactor, a new limiting factor for Q_{chem} is the residence time of the particles in the reduction zone.

The residence time hypothesis will be discussed in Chapter 5. The following sections introduce

Table 4.1 TGA results from 2 sets of 3 samples reduced in the reactor

Experiment	Sample	Initial mass (mg)	Mass change (mg)	change/inital (%)
1.25g/s	1	7577.3	523.0	6.90
	2	7786.2	534.2	6.86
	3	7950.8	552.1	6.94
	avg	7771.4	536.4	6.90
2.5g/s	1	7730.9	479.1	6.20
	2	7998.5	494.1	6.18
	3	7950.2	475.8	5.98
	avg	7893.2	483.0	6.12

a model used for computational validation of experiments.

4.5 Modeling the Reduction Reactor

Experiments are effective because the controlled environment allows for observation of principles and easy troubleshooting. However, building or modifying an experimental setup can be expensive and time intensive and therefore it is sometimes preferable to build a mathematical model and investigate hypothesis that would be more difficult to try in an experiment. It can also be a helpful exercise to formulate equations describing the problem as this offers a different perspective and can lead to a better understanding of the principles that are being investigated. This chapter discusses a 1-D model developed to simulate the reduction reactor.

4.5.1 Scope and Methods

Computational analysis of a system needs to follow the principle of "as detailed as necessary but as general as possible". It would be foolish to try and build a model that aims at being as detailed as the real-world experimental setup. This would likely take more resources than doing the experiment. So a selection process is necessary when building a mathematical model to include only those parameters that are important for the correct function and to achieve the goal of the study. Therefore, a selection must be made for the modeling of the reduction reactor. This model should be used to predict the effectiveness of the setup and should be able to evaluate the effect of changing different parameters on the particles. With this in mind, it makes sense to include the reaction kinetics and fluid dynamics as well as the temperatures into the model. These governing principles allow investigation of the response of the system to changes in flow rate, temperature and residence time. Since the reactor bed is 50 mm wide and over 1500 mm long, continuity was assumed in the width-dimension (radial) and only changes that happen in the height dimension are investigated. This allows for a simple but accurate 1-D model.

4.5.2 The mathematical approach

The following section explains the governing equations of the model. This model was developed and published by Dr. Huang et al. [52] and is used here to investigate the reduction reactor analytically.

4.5.3 Governing Equations

The governing equations are derived from the mass balances and energy balances of the counter-flowing gas the and solid particles. The reaction kinetics are included by using a source term that references the kinetics model.

The volume-averaged mass conservation equation for the gas is written as

$$\frac{\partial(\epsilon\rho_g)}{\partial t} + \frac{\partial \rho_g u_g^s}{\partial z} = \frac{\partial}{\partial z}\left(D_g \frac{\partial \rho_g}{\partial z}\right) - (1-\epsilon) r_{O_2} \tag{4.1}$$

where ϵ represents the total porosity of the bed and ρ_g the density of the gas. t is time and z is the vertical dimension, going from 0 mm at the particle outlet to 1506 mm at the top where the particles enter the tube through the hopper. The superficial gas velocity u_g^s is calculated by dividing the volumetric flow rate by the cross sectional area of the tube without taking the particles into account. D_g stands for the diffusivity of the gas and r_{O_2} is the oxygen production source term. It is calculated by

$$r_{O_2} = -(\rho_{ox} - \rho_{red}) \frac{\partial e_p}{\partial t} \tag{4.2}$$

In Equation 4.2, the oxygen production rate is calculated using the density difference of the oxidized and reduced particles multiplied with the rate of change in e_p which is the extent of reduction. This is calculated through the chemical kinetics model introduced in Chapter 2 (Equation 2.4).

The following equation can be derived from the O_2 mass conservation

$$\epsilon \frac{\partial C_{O_2}}{\partial t} + \frac{\partial}{\partial z}\left(C_{O_2} u_g^s\right) = \frac{\partial}{\partial z}\left(D_{O_2} \frac{\partial C_{O_2}}{\partial z}\right) - \frac{\partial}{\partial z}\left(D_{O_2} \frac{C_{O_2}}{\rho_g} \frac{\partial \rho_g}{\partial z}\right) + r_{O_2} \tag{4.3}$$

here, C_{O_2} is defined as the mass concentration which is calculated by $C_{O_2} \equiv \rho_g \xi_{O_2}$, where ξ_{O_2} is the oxygen mass fraction.

Deriving the energy balance for the gas phase yields

$$(\epsilon\rho_g c_{p,g})\frac{\partial T_g}{\partial t} + \left(\rho_g c_{p,g} u_g^s\right)\frac{\partial T_g}{\partial z} = \frac{\partial}{\partial z}\left(\epsilon_b k_g \frac{\partial T_g}{\partial z}\right) + h_{gs}a_{gs}(T_s - T_g) + h_{gw}a_w(T_w - T_g) \quad (4.4)$$

$c_{p,g}$ represents the specific heat of the gas, T_g is the gas temperature and T_s the solid temperature. ϵ_b is the bulk porosity and k_g denotes the thermal conductivity of the gas. hgs, hgw, hsw, hr, and hw are heat transfer coefficients from the different phases to each other and to the wall (subscript g for gas, s for solid and w for wall) while a_{gs} and a_w denote the interstitial area of the heat transfer.

From the energy balance of the solids one gets

$$\begin{aligned}(1-\epsilon)\rho_s c_{p,s}\frac{\partial T_s}{\partial t} + \left(\rho_s c_{p,s} u_s^s\right)\frac{\partial T_s}{\partial z} = \frac{\partial}{\partial z}\left(k_{s,eff}\frac{\partial T_s}{\partial z}\right) + h_{gs}a_{gs}(T_g - T_s) \\ +(h_{sw} + h_r)a_w(T_w - T_s) + (1-\epsilon)r_{O_2}\Delta H\end{aligned} \quad (4.5)$$

where ρ_s represents the density of the particles, $c_{p,s}$ is the specific heat of the particles, u_s^s is the superficial velocity of the particles and T_s is the temperature of the particles. $k_{s,eff}$ is the effective thermal conductivity of the particles and ΔH denotes the change in enthalpy that comes with the release of oxygen into the gaseous phase. The final governing equation looks at the tube energy balance

$$\begin{aligned}(\rho_w c_{p,w})\frac{\partial T_w}{\partial t} = \frac{\partial}{\partial z}\left(k_w\frac{\partial T_w}{\partial z}\right) + h_{gw}a_w(T_g - T_w) + (h_{sw} + h_r)a_w(T_s - T_w) \\ +(h_w + h_{rw})a_q(T_{amb} - T_w)\end{aligned} \quad (4.6)$$

ρ_w and $c_{p,w}$ are the density and heat capacity of the alumina tube, T_w denotes the temperature of the tube and k_w represents the heat conductivity of the alumina while a_q is the surface area of the tube.

The governing equations are then made dimensionless, a step that is explained in detail in the publication by Dr. Huang et. al on this model [52].

4.5.4 Boundary Conditions

The boundary conditions are implemented as follows

$$
\begin{aligned}
at \quad \textbf{t=0}: \quad & \overline{\rho}_g(z,0) = \overline{\rho}_0 \\
& \overline{C}_{O_2}(z,0) = \overline{C}_0 \\
& \overline{T}_g(z,0) = \overline{T}_w(z,0) = \overline{T}_0(z)
\end{aligned}
\tag{4.7}
$$

which means that at $t = 0$ the gas density, oxygen concentration and the gas and wall temperatures are set to specific start values using Dirichlet-type boundary conditions.

$$
\begin{aligned}
at \quad \textbf{z=0}: \quad & \left.\frac{\partial \overline{p}}{\partial \overline{z}}\right|_{inlet} = -\frac{Re_{E,inlet}\left(\overline{u}^s_{g,inlet}\right)^2 + \overline{u}^s_{g,inlet}}{Re_{D,inlet}} \\
& \overline{C}_{O_2} = \overline{C}_{O_{2,inlet}} \\
& \overline{T}_g = \overline{T}_{g,inlet} \\
& \left.\frac{\partial \overline{T}_s}{\partial \overline{z}}\right|_{out} = 0
\end{aligned}
\tag{4.8}
$$

The boundary conditions in 4.8 describe the bottom of the tube where Neumann-type boundary conditions address the pressure at the gas inlet and the temperature of the exiting solids while Dirichlet-type boundary conditions are used to describe the oxygen concentration and gas temperature at the inlet.

$$
\begin{aligned}
at \quad \textbf{z=H}: \quad & \overline{p}_{out} = \overline{p}_\infty \\
& \left.\frac{\partial \overline{C}_{O_2}}{\partial \overline{z}}\right|_{out} = 0 \\
& \left.\frac{\partial \overline{T}_g}{\partial \overline{z}}\right|_{out} = 0 \\
& \overline{T}_s = \overline{T}_{s,inlet}
\end{aligned}
\tag{4.9}
$$

Finally, 4.9 uses Neumann-type boundary conditions to prescribe the oxygen concentration and gas temperature at the top of the tube and Dirichlet-type boundary conditions for the pressure and particle temperature.

4.5.5 Simulation Setup and Results

The very small time steps of $\Delta T = 2e^{-4}s$ for the partial differential equations are solved via Crank-Nicolson finite-difference scheme. The computational domain that is being simulated is shown in Figure 4.5. The heated zone is 305 mm long, representing the experimental setup. The figure shows the location of thermocouples T_1 through T_6 which will be used to visualize the temperatures during the simulation compared to experimental data. Huang et al. used a grid-independence study and determined that a division of the computational domain into 241 nodes in the axial direction were sufficient for numerical stability [52].

Since the simulation domain replicates the experimental reactor, the simulation is designed to follow the experimental procedure as closely as possible to improve the comparability of the numerical results with experimental data. To achieve this, the initial conditions match the beginning of the experiments where the reduction zone is at 1000 °C and the material is fully oxidized. Then, the reduction zone is heated with a rate of 5 K per minute while the particle flow is started at 0.75 g/s and the nitrogen counter-flow at 0.75 g/s. Analogue to the experiment, once the furnace temperature reaches 1350 °C, the particle and gas flows are increased to the target flow rates while the reduction zone continues to heat up. The total simulated time is 180 minutes and the time step size is $\Delta t = 0.002$ s

The model was run on the MSU high performance computing cluster (HPCC) . Each simulation took about 30 hours on a single node.

Figure 4.6 shows a comparison of the simulation results and an experimental run at 1.25 g/s. The solid lines represent the simulation data while the dashed lines show the experimental data. The comparison shows that the model is able to predict the temperatures T3-T5 with good accuracy while the simulated T2 is much hotter than the experimental data. This can be explained by the convection cooling of the quenching zone section of the reactor tube in the experimental setup that was not implemented in the model. T1 agrees mostly, except for some bumps in the experimental data and T6 is simulated too cool. However, the model works sufficiently well.

Figure 4.7 shows the comparison of a simulated 2.5 g/s run with an experiment. Here, some

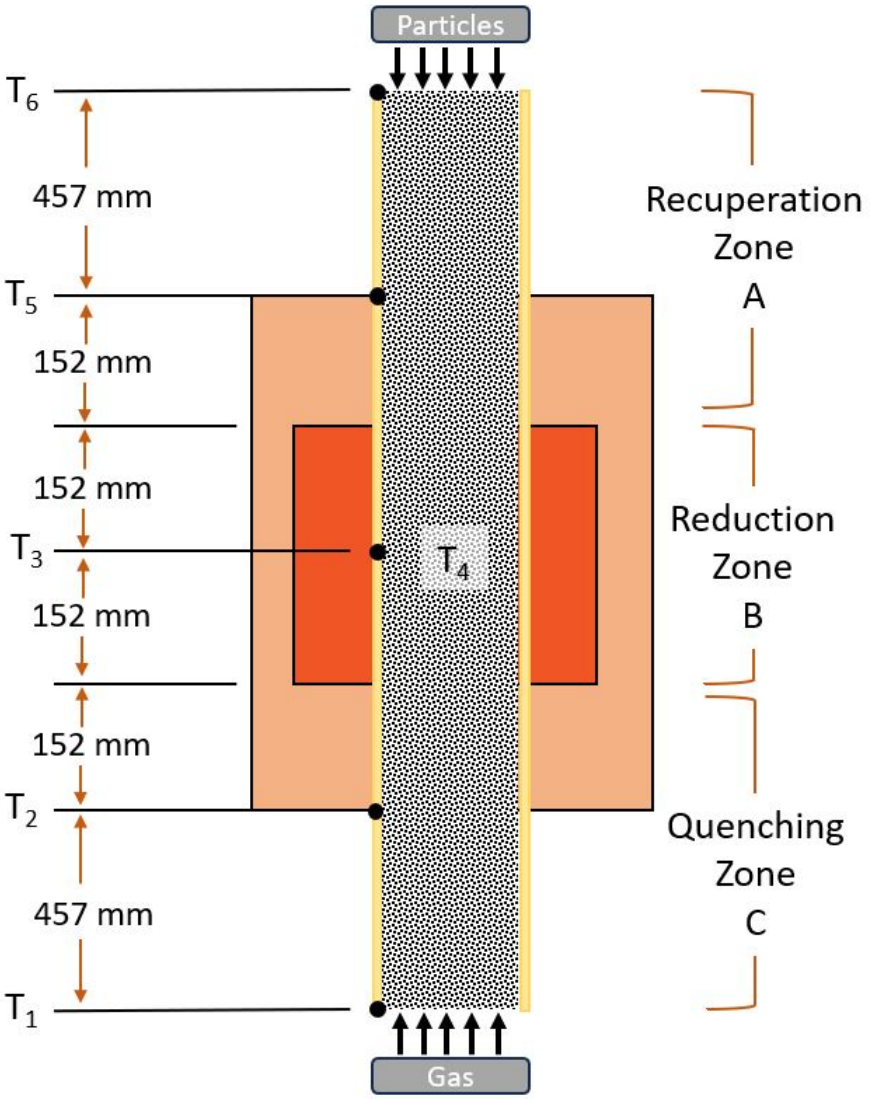

Figure 4.5 **1D Simulation Geometry** The model geometry includes the tube, insulation, the reduction zone. All thermocouple locations correspond to the location in the experimental setup [52]. The geometry is divided into 241 nodes in axial direction.

disagreements between the experiment and simulation show up. While the furnace temperatures (T3 and T4) and the upper and lower temperatures T1 and T6 are in good agreement, the recuperation temperature T5 and the quenching temperature T2 are not captured well by the simulation (however, later experiments saw similar trends in those temperatures). The simulated values follow the experiment reasonably well during the heat up process but once the particle flow rate is increased from 0.75 g/s to 2.5 g/s, the simulation shows a temperature shift towards the recuperation zone, as the quenching zone cools down and the recuperation zone heats up. The experiment shows good

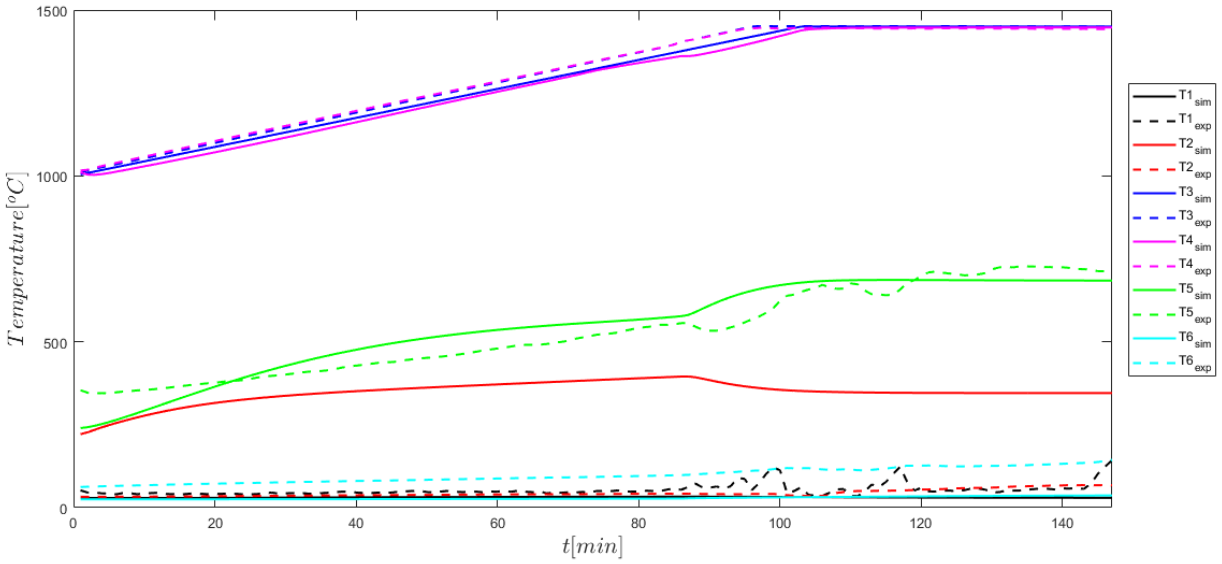

Figure 4.6 **Simulation and Experimental Comparison 1.25g/s Run** The simulation is stable and reaches the target temperature of 1450 °C and 1.25 g/s of solid flow. Dashed lines show experimental data from a 1.25 g/s of solid flow run. The furnace and tube temperatures match well and T5 is in great agreement. T2 in the simulation is too hot, however this could be due to convection cooling of the quenching zone section of the reactor tube in the experimental setup which is not considered in the model. The inlet and outlet temperatures match reasonably well.

heat recuperation as both ends of the reactor remain close in temperature despite both heating up.

The biggest surprise from the simulation is visualized in Figure 4.8. It shows the extent of reduction, e_p over time at different spots in the tube. It is evident that the particles start reducing as the temperature increases. However, around 90 minutes into the simulated experiment, the particle flow rate is increased from 0.75 g/s to 2.5 g/s and the particles are quickly fully reduced. This is a very different result from the experiments. Section 4.3 shows sample analysis results from experimental reduction runs that show values of conversion of around $e_p = 0.83$ instead of 1.

The red curve in Figure 4.8 shows that according to the model, when steady state is reached at around 100 minutes of simulated run, the particles that are at the center of the reduction zone are already fully reduced. This would mean that after a residence time of just 4 minutes, the particles are fully reduced and no more reaction is taking place in the bottom half of the reduction zone. In the experiments, we saw the opposite effect where the particles are not fully reduced, even after 8 minutes in the reaction zone.

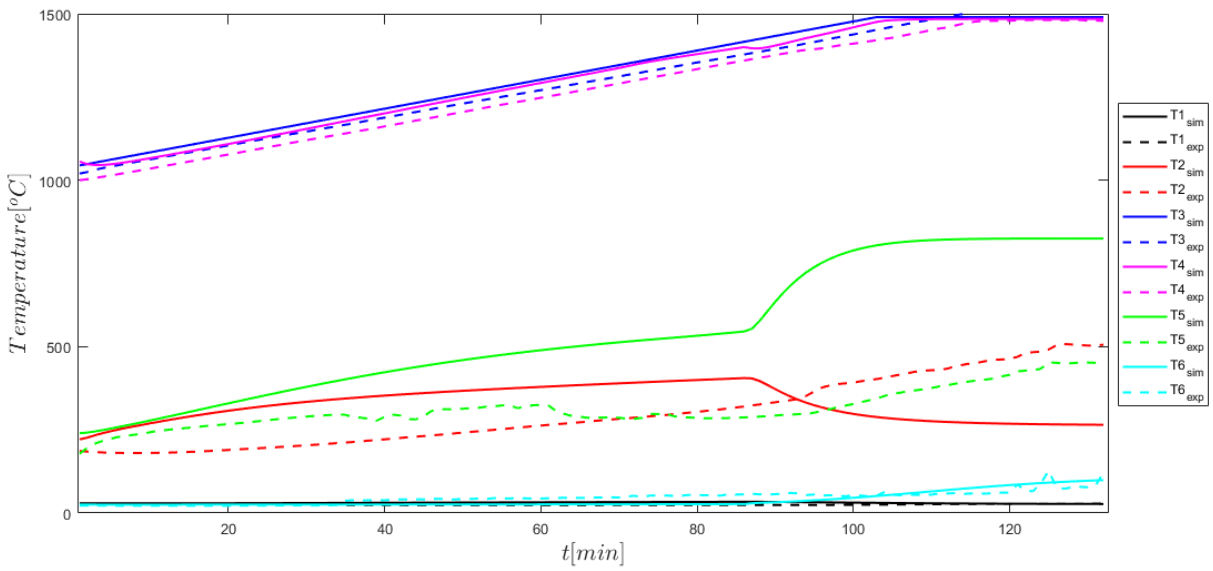

Figure 4.7 **Simulation and Experimental Comparison 2.5g/s Run** The simulation is stable and reaches the target temperature of 1450 °C and 2.5 g/s of solid flow. Compared to the 1.25 g/s run, the temperature T5 is less accurate, however T2 is closer in this simulation. The experimental data shows that both temperatures should remain equal, pointing at good heat recuperation. In the simulation, the gas flow rate seems to be too high when the solid flow rate is ramped up as T5 and T6 increase and T2 decreases, indicating that the heat is pushed up by the gas.

4.6 Conclusions from Bypass Experiments and 1D Model Validation

Analytical and experimental investigations showed that bypassing a part of the counter-flowing gas helped prevent bed fluidization and allowed for a significant increase in solid throughput while maintaining full sensible heat recuperation.

A 1D model proved effective at predicting temperatures and extend of reduction for lower solid flow rate experiments. A discrepancy between the extend of reduction in the model and experimental samples shows the need for an optimization of the reaction conditions in the reduction reactor. The following chapter investigates these discrepancies and resolves issues, resulting in higher conversion and chemical energy flux.

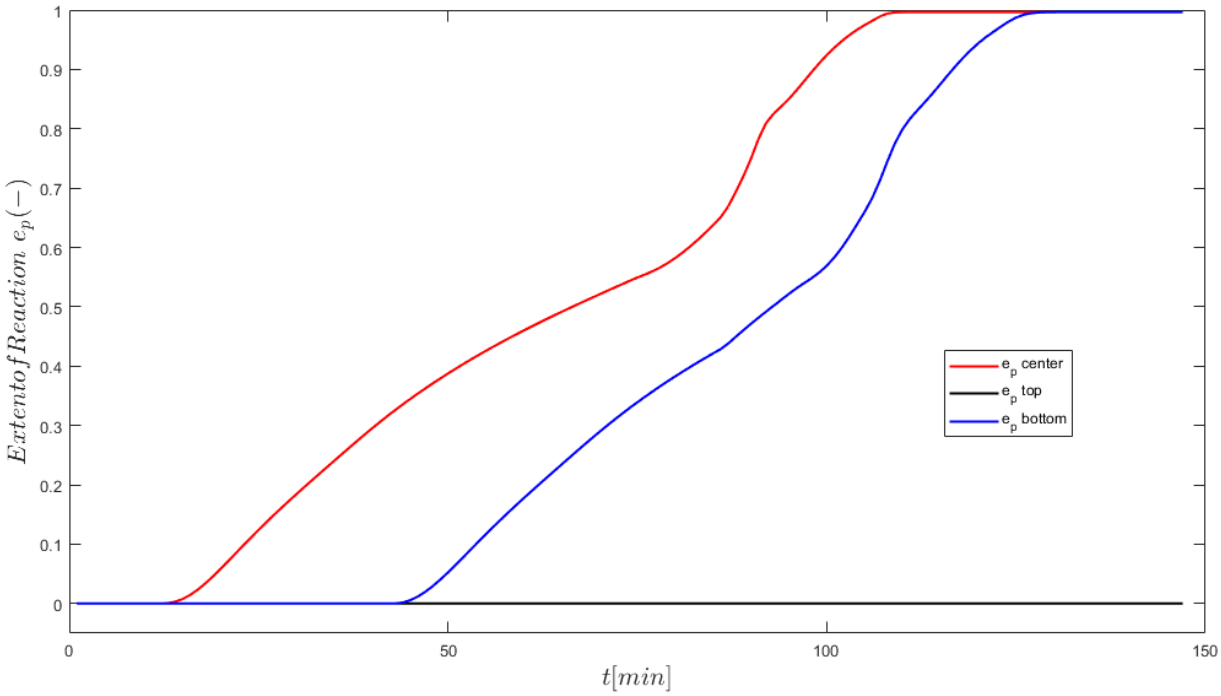

Figure 4.8 **Simulation Extent of Reduction** The extend of reduction e_p of the particle bed at three different locations over time for a solid flow rate of 2.5 g/s. The particles at the top are outside of the reduction zone and remain oxidized (black line remains at 0). The extend of reduction in the center begins to increase as the furnace heats up. As the reduced particles move down, the extend of reduction quickly increase at the bottom checkpoint, resulting in the fast increase in the blue line.

CHAPTER 5

RESIDENCE TIME INVESTIGATIONS

This chapter describes mathematical and experimental analysis of the effect of the residence time in the reduction zone on the energy storage material MgMnO. This was done to investigate discrepancies between expected extend of reduction from a 1D simulation and early experiments compared to later experimental results.

5.1 Problems with Residence Time

The previous Chapter 4 described the effects of increased bed flow rates on the extend of reduction of the storage material. Sample analysis showed that particles that spent 8 minutes in the reactor were only 83% reduced while samples spending 16 minutes in the reactor were 92% reduced (see Table 4.1, Equation 3.8). The difference in extend of reduction warrants an investigation since the energy density of the material decreases if the chemical potential is not fully utilized during charging.

Residence time is an important metric for chemical reactors. Sufficient reaction time is a challenge for continuously operating reactors [53], [54]. The optimization of this factor is important since an insufficient residence time leads to incomplete reaction, as in this example, while excessive residence time points to an inefficient reactor design which can lead to overheating among other things. Halder et. al and Abanades et al. have studied residence time of metal oxides in reactors experimentally and numerically [55], [56].

The required residence time depends on multiple factors. The complete conversion of the material requires that the reactants are available, the reaction conditions are suitable and that the reaction kinetics are taken into account. For this reactor, two possible issues are looked into to improve the conversion of the energy storage material using a continuous flow reduction reactor. It is possible that the reaction kinetics are too slow for the residence time. Another point of interest is the temperature penetration into the particle bed.

5.2 Mathematical Considerations of the Residence Time Problem

Firstly, the reaction kinetics will be examined. As Chapter 2 explained, the MgMnO material is a metal oxide with a spinel lattice structure. For those, there are two known mechanisms governing the interaction between oxygen and the solid.

The surface of the material which is exposed to the surrounding atmosphere absorbs or releases oxygen based on the oxygen chemical potential gradient between the atmosphere and the material. This can be mathematically described by an Arrhenius-type equation [57]. The other oxygen transport mechanism entails the bulk diffusion of the ionic oxygen into the lattice. This is governed by factors like the mobility of ionic and electronic defects in the material and the lattice structure and has been studied extensively for many different materials. Resources for the study of oxygen diffusion into and out of a crystal lattice can be found here [41, 58, 59, 60, 61, 62].

As mentioned, a thermodynamic equilibrium model for MgMnO at different temperatures and atmospheres has been published previously [33]. A model describing the reaction kinetics was developed using that data (See Section 2.3). An assumption of this model is that the bulk diffusion is orders of magnitude faster than the surface absorption of oxygen. Therefore, it uses an Arrhenius-type equation as the governing equation. A series of TGA relaxation experiments of pelletized material samples were conducted to find constants A_0 and E_a that accurately describe the interaction of the material with oxygen in the atmosphere [52]. A validation of the kinetics model can be found in Chapter 2, Figure 2.5.

The governing equation of the chemical kinetics (Equation 2.4) can be modified to calculate the reaction time of a sample under specific conditions:

$$t_{ch} = \frac{d_p T}{\Delta\mu} A_0 e^{\frac{E_a}{RT}} \tag{5.1}$$

The time for complete reaction t_{ch} depends on the particle diameter d_p, which is 5.5 mm for the particles used in this round of experiments, the reactor temperature T, which is 1500 °C, $\Delta\mu$ which denotes the change in chemical potential, $(150 kJ/mol_{solid})$. The fitted constants are $A_0 = 294.9 Js/(mol_{solid} Km)$ and $E_a = 113.7 kJ/mol_{gas}$, which is interpreted as the activation

energy for the reaction. These constants are for reduction conditions of 1500 °C and an inert atmosphere with 0.01 atm oxygen. The ideal gas constant is $R = 8.314 J/(mol_{gas} K)$.

From Equation 5.1 we see that the scale of reaction time for the MgMnO material at a temperature of 1500 °C and in an atmosphere of 0.01 atm O_2 is around 1 minute. The experimental reactor has a heated length of 305 mm. Particles moving through that reduction zone at a flow rate of 2.5 g/s have a residence time of around 8 minutes. This should be more than enough time to react under reducing conditions. This excludes the reaction kinetics as the limiting factor for the extend of reduction in the faster-flowing experiments.

If the kinetics at ideal reduction conditions are very fast, the particles must not be at ideal reduction conditions inside the reactor. To investigate the particle and fluid dynamics inside the reactor, a transient finite-difference model was designed. The details of the model are described by the authors Korba et al. [63]. It accounts for the gas and solid phases of the sweeping gas and the energy storage material. The ideal gas law is applied to the gas phases. Ergun's equation [64] is used to calculate the pressure drop across the particle bed. A uniform axial velocity is assumed for the particles as they move down the tube. The model solves the following equations: mass conservation, momentum equation, energy balance for the gas and solid phases. The chemical reaction is included using the chemical kinetics model (Equation 2.4). To simplify the boundary conditions, axis symmetry of the reactor design is assumed. The boundary conditions describe the conditions on the inlet and outlet of the reactor tube for both streams. They also set the heat provided to the system by the furnace and heat losses.

An important finding from simulating the reduction reaction is the radial and axial temperature distribution in the counterflow reactor at steady state conditions. Figure 5.1 shows results of the simulation of a run with a solid flow rate of 2.5 g/s and a reduction temperature of 1450 °C. The radial temperature distribution (left) points towards a major problem with the reactor design. The gradient of temperature between the particles at the tube wall and in the center of the tube is extreme and explains the lower extent of reduction of the particles. Using Equation 5.1 it shows that the particles would need to spend over 10 minutes in the center due to the lower temperature of

approximately 1000 °C compared to one minute at the tube wall. The temperature gradient seems to be a result of the limited heat flux into the core of the particle bed. Since the particles at the wall are reacting and consume heat to power the reduction, they shield the particles at the core from being heated up further. The center and right plot in Figure 5.1 show the extent of reduction and oxygen content in the gas. Both support the hypothesis that the boundary layer particles are consuming the majority of the heat that is transferred into the bed through the wall.

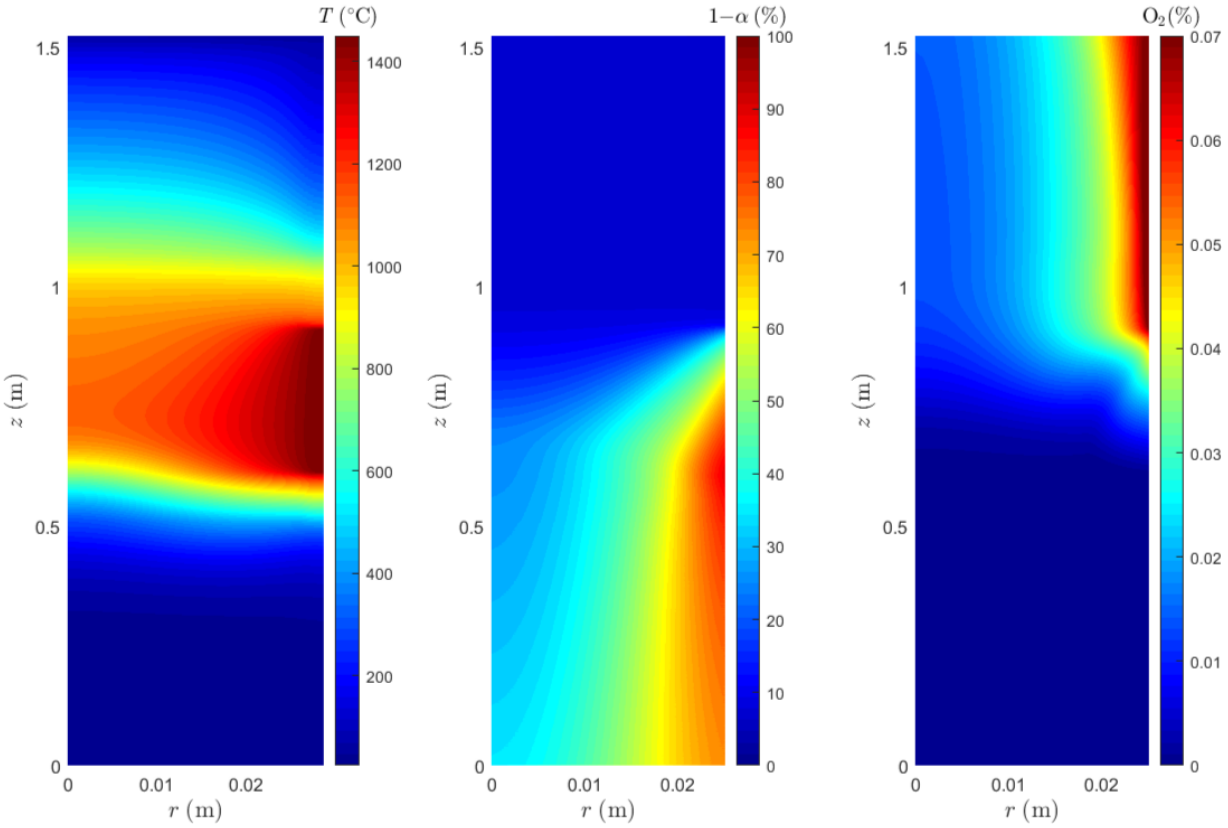

Figure 5.1 **Transient Model Results for 2.5 g/s Reduction** Results of the 2D model 2.5 g/s 1450 °C and heated length of 305 mm. The left plot visualizes the radial and axial temperature distribution and it can be seen that the temperature differs from the tube wall (r=0.025 m) to the center (r=0 m). The resulting decrease in chemical reaction of the particles in the center is visualized by the figures of the extent of reduction (center) and the radial oxygen concentration in the gas (right). I gratefully acknowledge the contribution of producing and visualizing these results by Dr. David Korba.

Two ideas were discussed to try and expose the particles in the center of the tube to the temperatures necessary for quicker reaction kinetics. A fluidized bed design can be used to mix

the particles and equalize the temperature of the bed. However, the packed bed is too dense to be fluidized effectively. Particles would need to be stopped from entering the reaction zone while particles move down out of the zone for space to be present for the particles to fluidize. A second option is to increase the heated length: in a long reaction zone, the particles at the wall react fully and once the reaction potential of that boundary layer is reached, they allow heat to penetrate deeper into the bed.

To investigate the longer heated zone hypothesis, the transient model was modified to accommodate a longer reaction zone. Figure 5.2 shows the comparison of the simulation between a 305 mm and 450 mm heated zone. The two plots on the left visualize the radial heat penetration in the regular compared to the longer heated zone simulation. The results look promising as the temperature of the center of the bed, which is at r=0, is much higher in the longer reactor compared to the shorter reactor. The right side of the figure shows a visualization of the predicted extend of reduction of the particles.

This predicted improvement warrants an experimental investigation.

5.3 Experimental Validation of Residence Time Simulation Findings

To increase the residence time of the particles, a modification to the system was necessary. A first approach was an additional furnace to add heated length to the setup and therefore increased the residence time. For budgetary reasons a bigger furnace was out of the question. The furnace design poses a challenge to using consecutive furnaces instead of one large furnace with sufficient heated length. Conventional high-temperature furnaces use resistive Molybdenum disilicide ($MoSi_2$) heating elements. The $MoSi_2$ is an ideal candidate because at high temperatures it forms an oxide layer of silicon dioxide which protects the heating element from further oxidation and allows for operation in regular air. The "U"-shaped heating elements are hung down into the furnace cavity. This design is necessary since the elements quickly lose stiffness at temperatures above 1400 °C. If the elements were installed horizontally or vertically standing, they would bend under their own weight, risking damage to the element and insulation. This design restriction makes a two-furnace reduction zone unfeasible since the heating element contacts on top of the furnace are made of

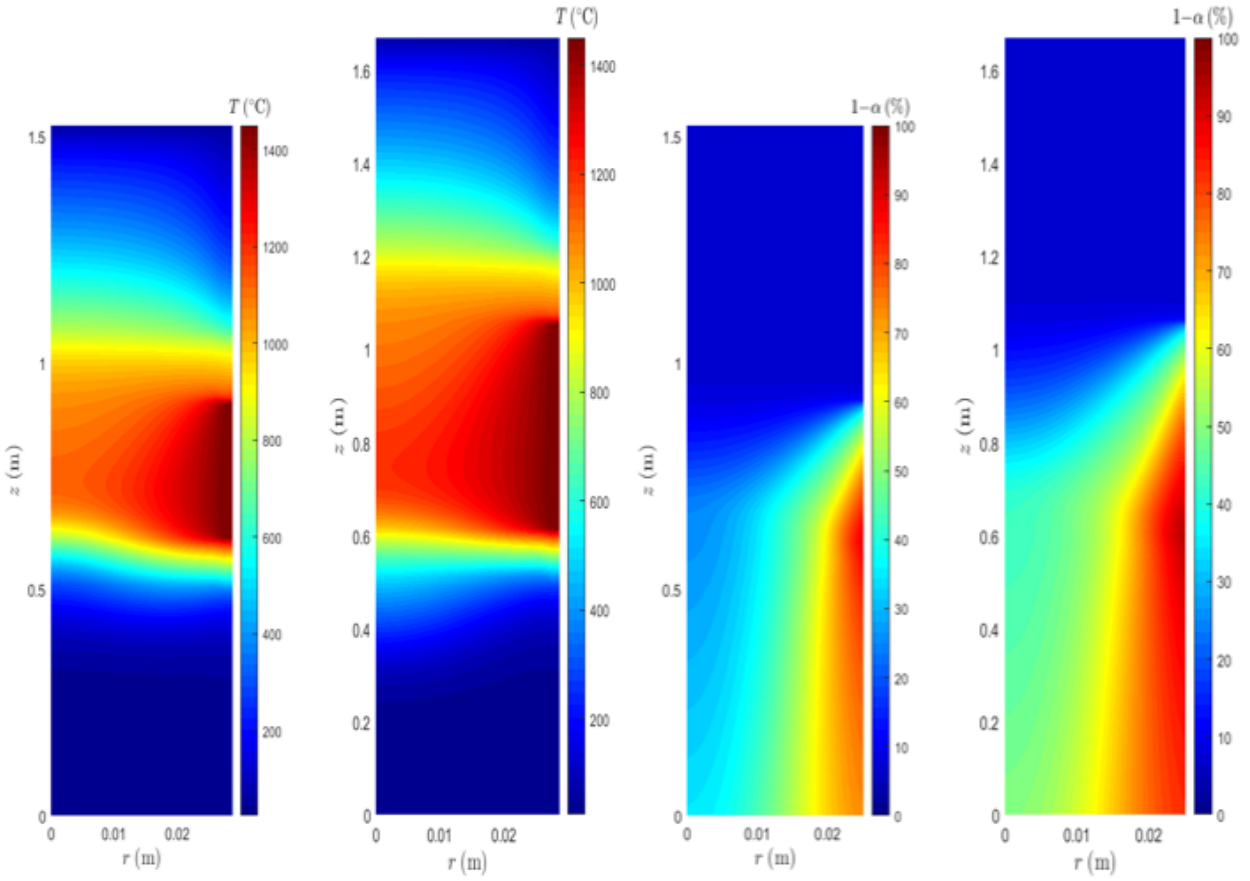

Figure 5.2 **Simulation Comparison of Different Residence Times** Results of the 2D model 2.5 g/s 1450 °C. The shorter plots show the heated length of 305 mm in comparison to the longer 450 mm zone. The temperature plots (left) and extent of reduction plots (right) show that the longer residence time increases the temperature of the particles in the center which results in a greater extend of reduction. I gratefully acknowledge the contribution of simulating and visualizing these results by Dr. David Korba.

aluminium and need to be exposed to natural convection conditions to prevent overheating. A long insulated section between the two furnace was considered. The length needed to protect the electrode connections is approximately 350 mm. At this length, the particles would cool down to oxidizing conditions and likely react with the oxygen in the sweeping gas that is flowing up from the bottom reduction zone. This would reduce the efficiency of the bottom reduction zone.

Instead, it was decided to experiment with building a furnace that uses vertical standing $MoSi_2$ heating elements. To prevent the elements from bending and breaking, alumina sheathes were manufactured from tubes and applied using alumina-based high-temperature refractory cement.

Figure 5.3 shows the results of a first trial for the modified heater. The heating element succeeded in bringing a cavity up to 1500 °C and inspection showed no damage to the element and good adhesion of the supportive sheaths.

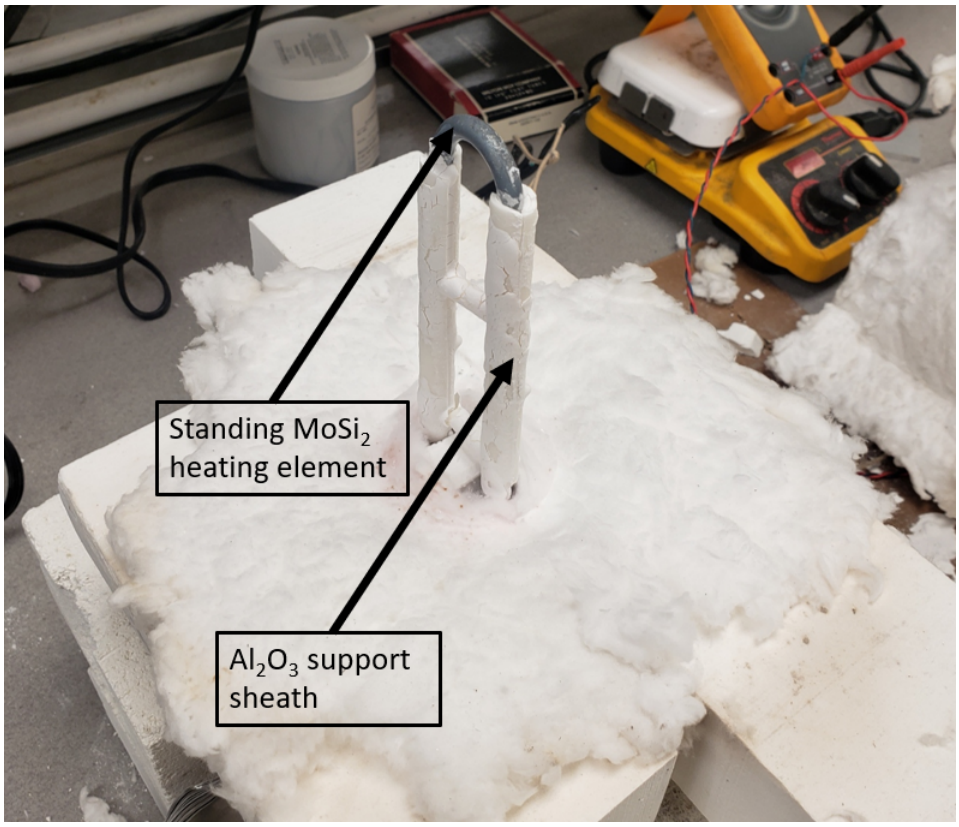

Figure 5.3 **Modified MoSi2 Heating Element** A $MoSi_2$ heating element with Al_2O_3 support sheaves after a successful 1500 °C test. The heating element stayed straight and there was no sign of reaction with the sheaths or the refractory cement.

The next step after proving that the modified $MoSi_2$ heating elements are able to operate in a vertical standing installation at high temperatures was to build the furnace cavity. The internal dimensions were chosen to ensure sufficient heated length and distance from heating elements to the tube. The cavity has a height of 200 mm and width and depth of 150 mm. Insulation of the cavity is made up of different layers. The inner-most insulation layer is made up of alumina AL-25/1700 type boards from Zircar Zirconia and were bonded with alumina rods and refractory cement. The space between the core insulation and the steel shell (see the center image in Figure 5.4) was stuffed with fibrous alumina insulation from McMaster. The insulation thickness exceeds 100 mm in all

directions except for the top, where a thinner insulation is beneficial as it decreases the time the particles spend between the two reduction zones.

To provide the power and the controls, a leftover SentroTech tube furnace controller was connected to the heating elements. A test run proved the furnace operational at 1500 °C, however, the two heating elements that were initially installed were not able to reach the heating rate of 5 K targeted by the furnace controller. After installing an additional 2 heating elements, the furnace was installed underneath the SentroTech STT-1700-12. Figure 5.4 shows the reduction setup with the two stacked furnaces as well as details during the manufacturing of the second furnace.

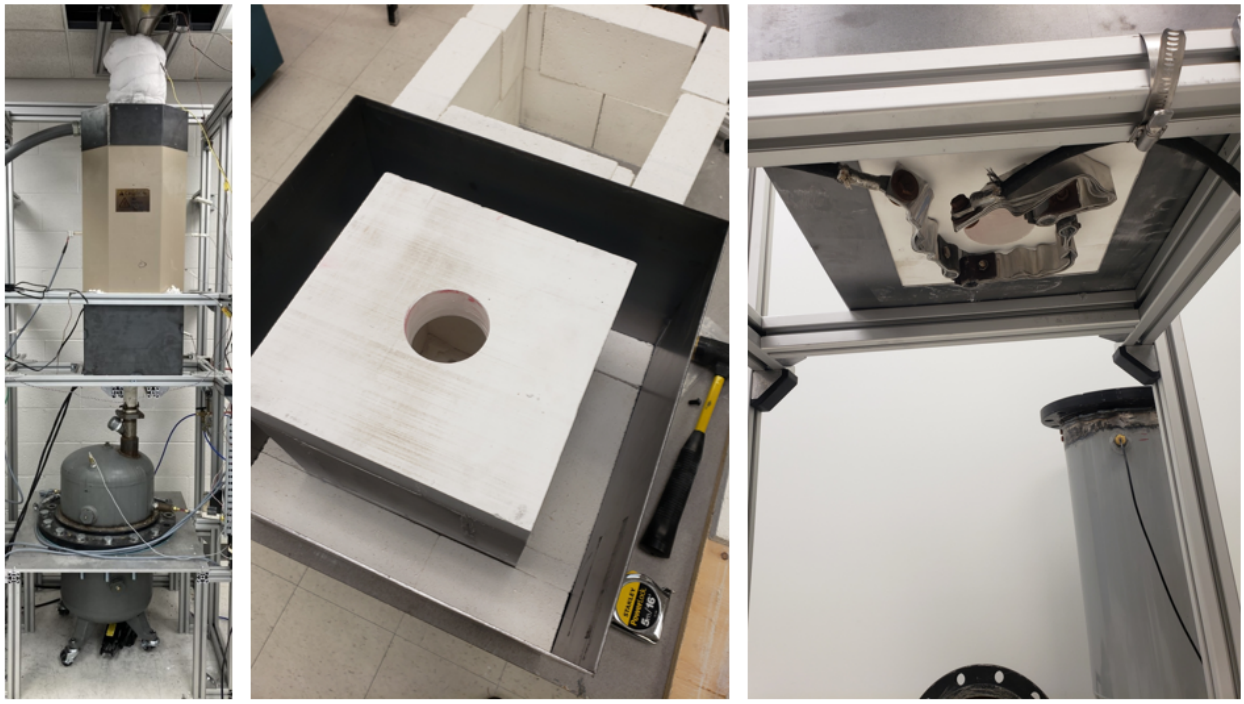

Figure 5.4 **Adding Heated Length to the Reduction Reactor** Pictures of the manufacturing and installation of a second furnace to extend the heated length of the reduction setup.

The second furnace added 200 mm heated length, but including the insulation on the top and bottom, the bed height was increased by 350 mm. A side effect of the increase in bed height was an increase in pressure gradient in the bed. This brought the chamber pressure back up to peak between 0.4 bar and 0.5 bar after being lower due to the bypass tube. Figure 4.2 shows that those pressure levels were problematic and that only through installing the bypass tube, we were able to bring the

pressure peaks down below 0.4 bar. However, with the extended bed height, the pressure peaked above 0.4 bar even after installing a bigger diameter bypass tube. This led to failed experiments due to the same bed lifting and clogging issues that were seen before installing a bypass tube in the original setup. Multiple tests with different diameter bypass tubes were unsuccessful in maintaining flowability in the new reactor.

The solution to the flowability issues was to again increase the particle size from 3.5 mm to 5.5 mm. Bigger particles have two advantages; As Figure 2.2 shows, the heat transfer at reduction temperatures increases with particle diameter. In addition to that, the ratio of density over surface area increases which favors flowability as larger particles have a much higher fluidization velocity (see Equations 3.10 - 3.12). These larger particles were the first not made in house. The manufacturing was outsourced to an external company due to the inability of the lab equipment of producing spherical particles of that size. The company used large-scale disc pelletizing and sieving equipment to produce a big quantity of particles.

System adaptations to use bigger particles included design and manufacturing of a bigger l-valve and different catch-can operation. Figure 5.5 shows the new l-valve compared to the one used for the smaller particles.

The larger particles finally enabled bed flow in the dual-furnace configuration at 1500 °C and 2.5 g/s. Figure 5.6 shows experimental data from a test run where the furnace temperature was increased to 1450 °C to ensure flowability before increasing the temperature to 1500 °C. The oxygen evolution relates to a storage flux Q_{chem} of 1000 kW/m^2. This was the highest storage flux achievable with this reduction reactor setup. Any increase in temperature or particle flow rate resulted in bed clogging. Even the presented experiment was cut short due to clogging after a short period of steady-state reduction.

5.4 Single Furnace Heated Zone Extension

After continued flowability issues with the two furnace setup, a second approach to increasing the residence time of the particles was pursued. For this, the cavity of the main furnace, the SentroTech STT-1700-12 was extended as shown in Figure 5.7. The original heated zone length

Figure 5.5 **Modified L-Valves** The l-valve used to run 3.5 mm particles (bottom right) compared to the new l-valve for the bigger 5.5 mm particles. The two valves are used to control the flow of particles and are installed at the bottom of the particle bed. The bigger valve is made from stainless steel and has an outlet diameter of 50 mm while the smaller valve is machined from a billet of aluminum and has an outlet diameter of 25 mm.

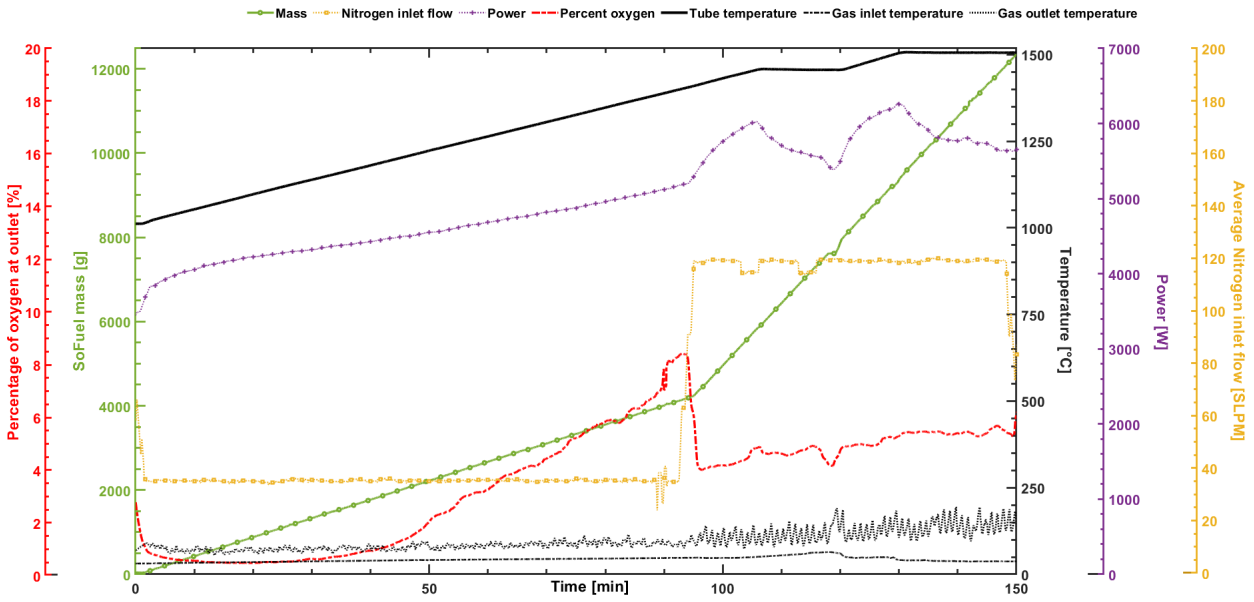

Figure 5.6 **Experimental Data from dual furnace run** Experimental data from a run using the pulsed counter-flow concept with a bypass tube and dual furnace setup. The particle flow rate of the 5.5 mm diameter particles was increased from 0.75 g/s to the target flow rate of 2.5 g/s as evident in the change in gradient in the green line. The furnace temperature was increased to 1500 °C and the storage flux Q_{chem} reached 1000 kW/m^2

was increased from 305 mm to 455 mm. A single heated zone enabled the use of a shorter tube as the thick insulated section between the two furnaces of the previous two furnace setup was removed. The shorter tube reduces the bed height which in turn reduces the pressure gradient and improves bed flowability. The total bed height from the l-valve to the particle hopper was reduced by 25% compared to the dual furnace setup while the heated zone was increased by 50% compared to the single furnace setup.

The extension of the heated zone was accomplished by removing the $MoSi_2$ heating elements as well as the top insulation. The steel body was extended and extra insulation was added to increase the height of the system. Afterwards, the top insulation was added and the original heating elements were installed. The heating elements are now shorter than the cavity which leads to an undesired temperature gradient inside the cavity, however due to time and budget restrictions the experiments were conducted with this setup.

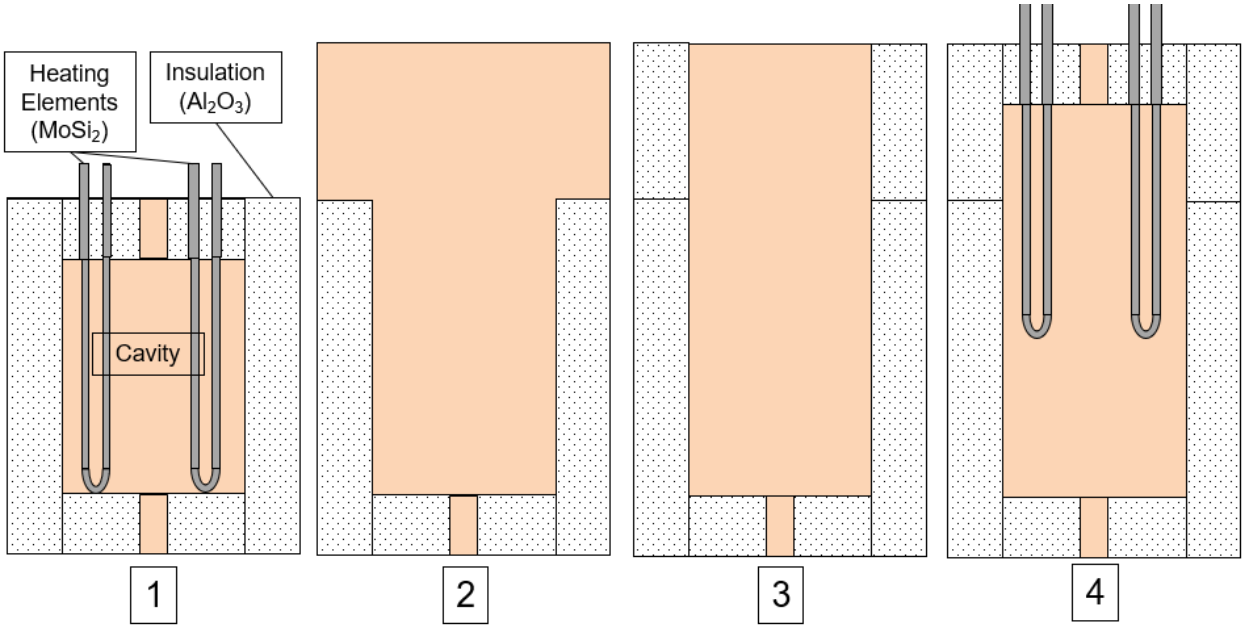

Figure 5.7 **Schematics of Furnace Modification** Schematics of the modifications done to the furnace in order to increase the heated length. The original heating elements made from $MoSi_2$ are not long enough to reach down into the last third of the heated cavity.

After establishing that the modified furnace was able to heat up to the reduction temperature and that a flow rate of 3 g/s was attainable with the particle bed, the first experiment to produce a

maximum chemical energy flux was conducted.

Two sets of samples are taken from the particles for each experiment to validate the chemical energy stored and the storage rate Q_{chem}: Approximately 30 g of particles are taken from the particles prior to the experiment. These represent the discharged state and starting point for the reduction reaction. After the reduction is concluded, approximately 30 g of particles are sampled from the particle bed. From the sampled particles, three sets of approximately 5 g are then taken for thermogravimetric analysis. A 5 g sample is loaded into a Netzsch STA 449F5 where it is heated up to 1000 °C. The sample dwells at that temperature and in an atmosphere consisting of 90 % oxygen for 8 hours before being cooled to room temperature. For both states, discharged and charged, three samples each are analyzed to determine the mass of oxygen absorbed by the sample. From the difference in oxygen absorbed one can extrapolate the amount of oxygen that the bed released during reduction which is then compared to the amount of oxygen measured in the exhausted gas.

5.5 Results and Discussion

Two experiments were conducted to prove the effects of residence time on the conversion of particles and increase in chemical energy flux (Q_{chem}) which were found in the simulation. The goal was to show repeatable results when running the reactor under similar conditions. Hence, the solid flow rate was set to 3 g/s and the reduction temperature was set to 1500 °C for two experiments. The nitrogen gas counterflow was pulsed between 0 SLPM and 190 SLPM with a frequency of 0.06 Hz and a duty cycle of 0.73 resulting in an average flow of 139 SLPM. The first experiment was run for approximately 80 minutes at steady state conditions before the prepared particles were all reduced. The second experiment exceeded 2 hours of steady state run time and proved no problems of the experimental setup with longer reductions. The temperature profiles for both runs are shown in Figure 5.9.

Figure 5.8 visualizes the location of the thermocouples in the experimental setup for the convenience of the reader. The temperatures of runs 1 and 2 are labeled following the pattern Tx.1 and Tx.2 where x refers to the location of the thermocouple from Figure 5.8 and the decimal refers to the run. The first run has solid lines with markers whereas the second run is shown in dashed

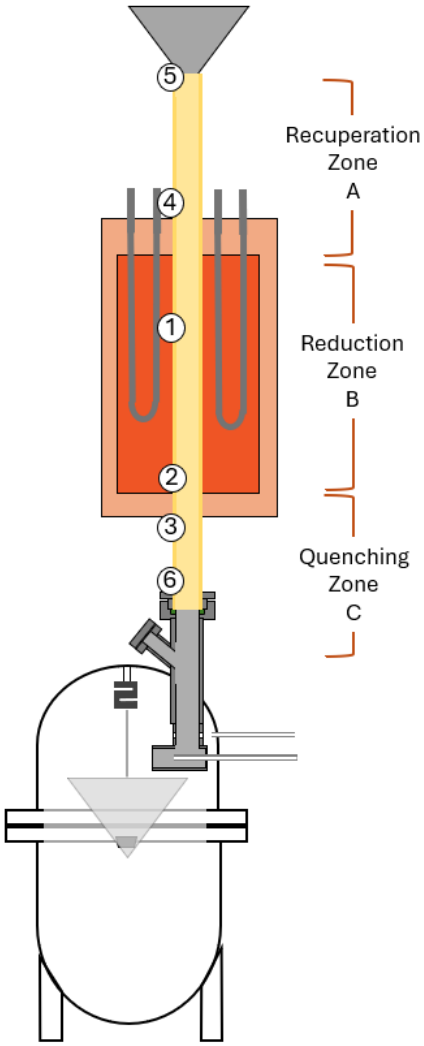

Figure 5.8 **Reactor Schematics with TC Locations** Schematics of experimental reduction reactor with thermocouple locations (T1)-(T6)

lines. The locations are colored consistently to ease the comparison of the same location between the runs.

Notable is that as expected, the temperature of the furnace is not constant across the length of the reduction zone. The bottom section (T2) is colder than the top (T1) because the heating elements are not as long as the heated zone. A more equal temperature across the length of the furnace would be preferable. The Figure also shows that the temperatures are quite similar between the two runs. The biggest difference is that in the first run T3 and T4 were very close together while during the second run there was a discrepancy of approximately 200 °C between them. The consistent gap

throughout the entire second run suggests that this difference was possibly introduced during the heatup stage and didn't have a major effect on the results. The same temperature difference of the tube above and below the furnace is also found in the 1D simulation results shown in Figure 4.7. An explanation could be that the higher gas mass flow rate in the recuperation zone, caused by the released oxygen, pushes more heat up into Zone A.

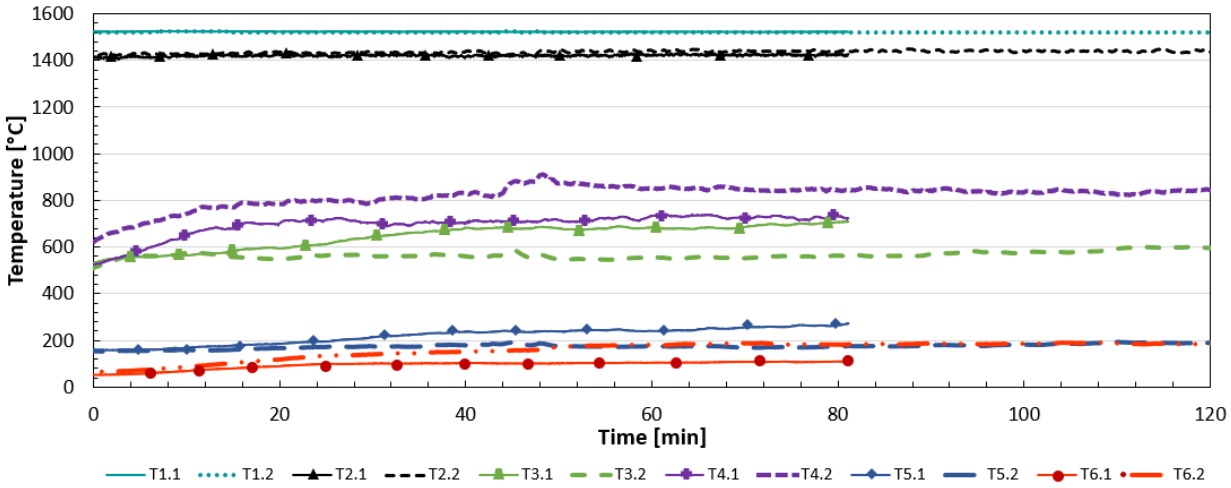

Figure 5.9 **Temperature Data from 3 g/s Experiment** Two sets of temperature data collected from experimental setup. Particle flow rates were 3 g/s, reduction temperature was 1500 °C. The first run temperatures are denoted as T x.1 and have solid lines with markers. The second run which lasted longer, is denoted by T x.2 and the dashed lines. The plot shows that the temperatures vary slightly between the two runs but approach a steady state.

As mentioned above, the oxygen release determines the quality of the experiment. Figure 5.10 shows the oxygen percentage (black) and nitrogen flow rates (blue, with markers) for both runs. The signals run parallel, showing good repeatability of the experiment. The fluctuations in both signals are caused by the pulsing gas flow which is necessary to avoid bed clogging [51].

The oxygen released for the first run from minute 10 to minute 80 is averaged to 8.03 SLPM. The chemical energy flux for that time is calculated to be $Q_{chem} = 1096 kW/m^2$. For the second run, the average oxygen flow from minute 10 to minute 130 is 8.61 SLPM which calculates to $Q_{chem} = 1179 kW/m^2$.

The previously mentioned sample analysis validates these results. The samples taken before the experiments show a different extend of oxidation. The three samples from before run 1 gained

an average of 0.52 % of weight during the oxidation in the TGA while the three samples of the particles prepared for run 2 only gained 0.18%. This explains the higher Q_{chem} in the second run where all setpoints were the same, except for the particles having more capacity to react. Analyzing the reduced samples from run 1 reveals that the particles gained an average of 300.5 mg per sample or 6.5% of the sample weight. This value is extrapolated on the entire bed and suggests an oxygen flow rate of 7.54 SLPM and $Q_{chem} = 1029 kW/m^2$. This is a good validation of the experimental oxygen measurements. Since the samples are taken from a single spot in the particle bed and the experimental oxygen data shows fluctuations in the oxygen signal, some discrepancy between the two methods is expected. Unfortunately, the samples taken after the second run were accidentally mixed with oxidized particles during the collection process. The analysis shows a much lower average mass gain of 251 mg and a high variance between the samples (standard deviation 33.8 in run 2 vs 19 in run 1). The average suggests a $Q_{chem} = 995 kW/m^2$ for run 2 which is much lower than the oxygen analyzer data claims. This difference is easily explained by the contamination and does not suggest problems with the reliability of the oxygen analyzer.

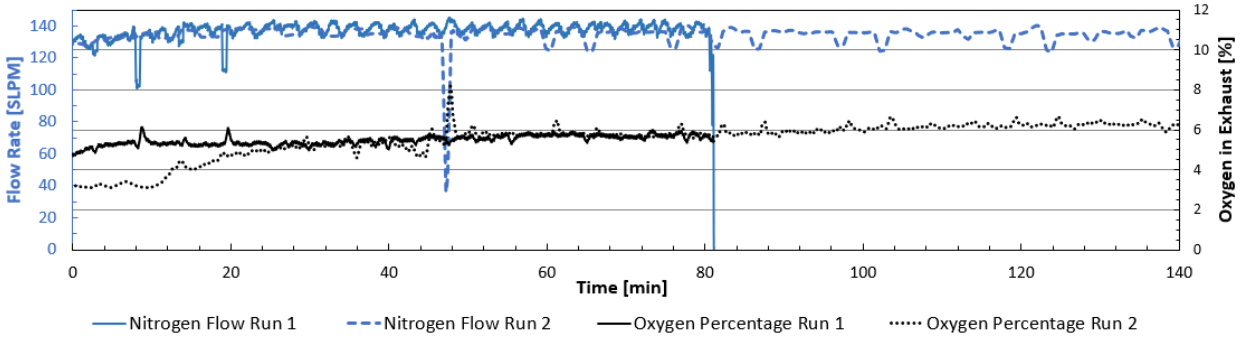

Figure 5.10 **Gas Analysis of 3 g/s Experiments** Nitrogen and Oxygen data collected from experimental setup. Particle flow rate was 3 g/s, reduction temperature was 1500 °C. The pulsing in the blue nitrogen flow is necessary to facilitate bed flow at these temperatures. Both experiments show the same nitrogen flow rate of approximately 139 SLPM and similar oxygen percentages of around 5.5-6.5 %.

5.6 Summary of the Residence Time Investigation

This chapter focused on facilitating a full reduction of the energy storage material. Analysis of the reaction kinetics suggested that the particles only need approximately one minute under ideal

reaction conditions for full conversion. A transient model revealed that low radial heat penetration restricted the particle temperature at the center of the bed. This resulted in slower reduction of the inner particles and an overall lower extend of reduction. Two different heated zone extensions were experimentally tested and showed a much higher extend of conversion which led to a maximum thermo-chemical energy flux of over 1.1 MW (peak for shorter periods of over 1.2 MW). This milestone shows the potential of this technology for large-scale energy storage use.

The following chapter identifies a major scale-up challenge caused by the energy penalty of separating the oxygen from the nitrogen recuperation gas and identifies alternatives.

CHAPTER 6

USING WATER VAPOR AS REDUCTION SWEEP GAS

A major milestone of the SoFuel project was to develop a techno-economic model that could be used to determine the levelized cost of energy storage (LCOS) . The goal was to include any cost related to building and running a grid-scale facility that uses a CSP tower to charge the fuel, a big oxidation reactor to discharge the material and a gas turbine to convert the heat energy released by the particles to electrical energy. The model takes a variety of inputs, from the ratio of long term and short term energy storage and the total power output of the plant to details like the wages in different locations. It can be used to find the optimal use case and to get an idea of the competitiveness of the SoFuel concept. The model predicted LCOS as low as 5ct/kWh-thermal. A manuscript explaining the model and its results was in development at the time of publishing of this work, spearheaded by Dr. Zaho. The idea for this chapter was inspired by that work and a similar model developed by Dr. Randhir, a co-author of the manuscript in the works.

6.1 Scale-Up Considerations

Figure 6.1 shows the results of a techno-economic study of the cost of a 100 MW energy storage system using CSP as energy source. The impact of the different components on the cost of operation and investment for a grid-scale SoFuel plant shows that a few components are significantly more expensive than others. This figure was created using quotes from Chinese websites for cheap nitrogen separation equipment. The cost comparison is a result of the techno-economic model.

Surprisingly, the oxygen separation equipment, which is necessary to maintain a low oxygen partial pressure in the bed, is among the most expensive components. This realization prompted an analytical and experimental campaign to research alternative sweep gasses other than oxygen depleted air to find a more economical alternative.

6.2 How Nitrogen Purification Works

Commercial or large-scale nitrogen generation is done using three different methods. Membrane separation, pressure swing adsorption (PSA) and cryogenic separation. All systems are designed to separate nitrogen from air, which includes approximately 78% nitrogen.

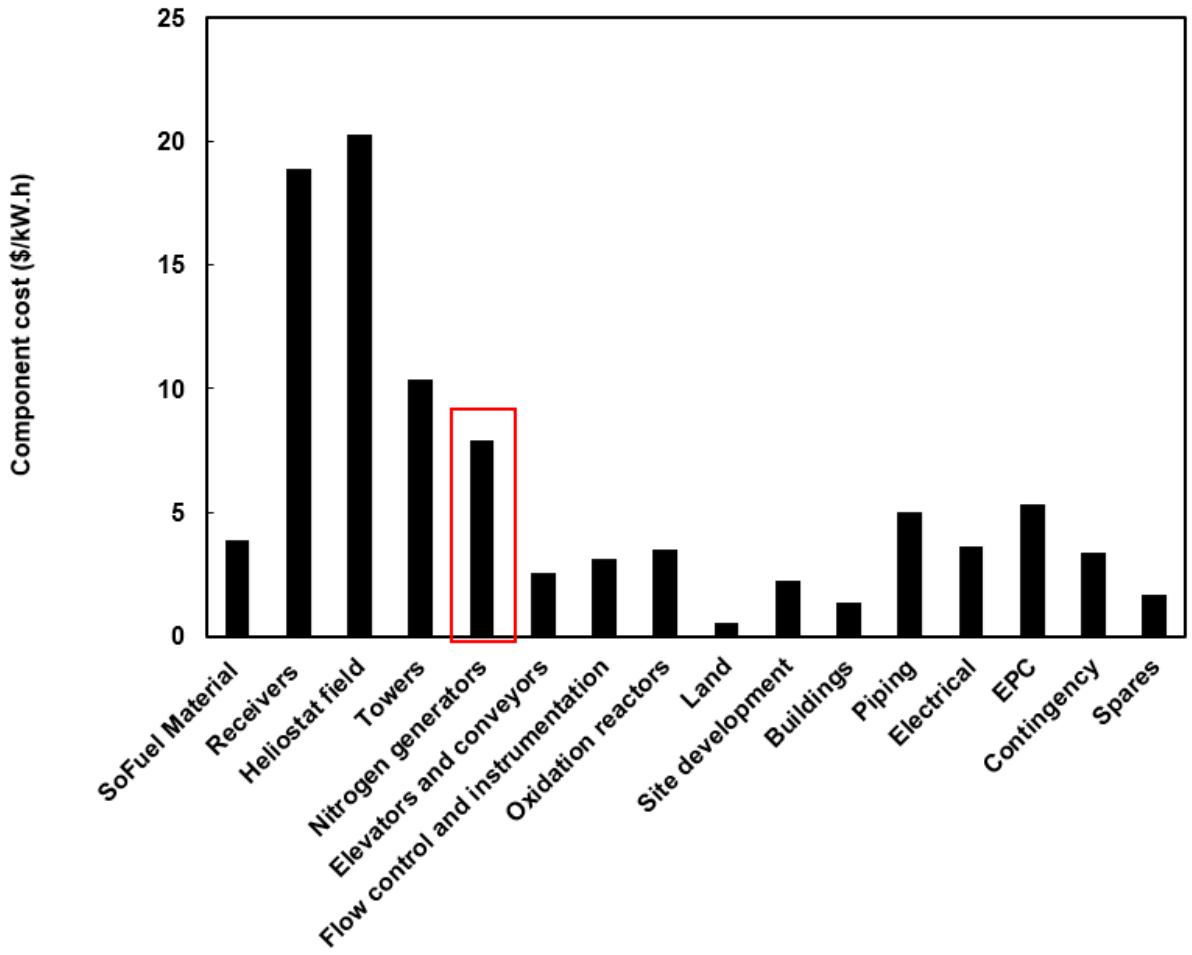

Figure 6.1 **SoFuel Techno-Economics** Results from a techno-economic model. The reduction setup is clearly the cost-driver due to the high initial cost for the heliostat field, the CSP tower, receivers, and the nitrogen generators.

Cryogenic separation involves pressurizing air to very high pressures, cleaning it and then cooling it below the boiling point of oxygen. The liquid oxygen that is produced can be expanded in a heat exchanger to achieve the low temperatures required. The different boiling points and densities of the liquid gasses allow for high purity separation at different pressures, often in dual tower distillation plants. The process provides high purity gasses at very large flow rates and is the most energy efficient among the three. Literature shows that a liquifier separation plant requires 0.15-0.25 kWh/m^3 nitrogen [65].

Membrane technology uses high pressure to force oxygen molecules in the air through fiber membrane bundles, leaving pure nitrogen gas behind. The process uses the most energy out of

the three due to the high pressure gradient and is not easily scaleable to produce high purity or high flow rates. Advantages are a quick start-up of the separation process compared to PSA and especially cryogenic separation. Reported energy consumption is in the range of 0.43 to 0.65 kWh/m^3 nitrogen. The nitrogen yield, which describes the ratio of purified nitrogen pumped out vs air pumped in varies with purity and lies between 0.22 and 0.64 [65].

Pressure Swing Adsorption for nitrogen production uses molecular sieves made predominantly from carbon. At high pressures of 5-12 bar, oxygen diffuses faster into the adsorbent molecular sieves than nitrogen. The name of the process comes from the concept of having two tanks filled with the adsorbent. While one is pressurized and used to purify the nitrogen, the other one is depressurized which causes the release of adsorbed oxygen, regenerating the adsorbent in that tank. The pressure swing takes place about once per minute and this process is able to provide high purity nitrogen at high pressures and high flow rates of up to 5000 m^3/h at 0.26 - 0.34 kW/m^3 nitrogen [65]. The factor of air input compared to nitrogen output is reported around 2.5-3 [66].

Due to the higher energy consumption and lower purity and nitrogen output of membrane systems, a PSA system was chosen for the nitrogen generation calculations for a scaled-up system. On top of the high initial equipment cost, the cost of energy for the separation process is generally much higher than the initial cost [65]. The energy consumption of any component of the storage system needs to be taken into account for the efficiency of the entire system. Any process that requires large amounts of energy needs to be investigated as the energy consumption is important for the goal of high efficiency.

6.3 Analysis of PSA Separation Energy Consumption

To calculate the energy use of the system, the compression of the gas needs to be accounted for as well as the separation work. Krenzke et al. developed an empirical formula to calculate the separation work for nitrogen from a fitted curve of reported separation values [67]. Bulfin et al. present the equation in generalized form [68]:

$$E_{PSA} = \frac{1000}{1 - x_{O_2,in}} * log\left(\frac{x_{O_2,in}}{x_{O_2,PSA}}\right) \tag{6.1}$$

The energy E_{PSA} is depended on the amount of nitrogen being purified and has the unit [J/mol$_{N_2}$]. To give an idea of the scale, a calculation of the separation work for the experimental reactor follows.

The nitrogen flow rate for a 2.5 g/s experiment is 120 SLPM, which is equal to 2 l/s or 0.089 mol/s using the ideal gas law. The oxygen concentration after PSA, is $x_{O_2,PSA} = 0.01$ while the input oxygen concentration is either 0.21 for air or 0.07 for recirculated nitrogen. Since the PSA process requires gas to regenerate the adsorbent and to demonstrate the worst case, $x_{O_2,in} = 0.21$ is chosen. The separation work computes to 150 W, which is equivalent to 7.5% of the stored chemical power. This would not be a big issue, especially since recycling the exhausted sweep gas would reduce the amount of oxygen that needs to be separated. However, the PSA and membrane systems work at high pressure, while the reduction reactor needs to operate at low pressures to decrease the oxygen partial pressure in the atmosphere of the reactor as well as to protect the reactor tube from bursting due to a high pressure gradient. This would require compression and expansion of large amounts of gas.

To estimate the work required for this, an isentropic ideal gas compression can be calculated and penalized with a compressor efficiency. Equation 6.2 can be used to calculate the specific entropy of the compressed ideal gas. With this, the enthalpy can be determined using tabled values for air [69].

$$s^o(T_2) = s^o(T_1) + Rln\left(\frac{p_2}{p_1}\right) \tag{6.2}$$

For the experimental reactor and an assumed pressure ratio of $p_1 = 1bar$ and $p_2 = 6bar$, the isentropic enthalpy difference between the ambient air and the compressed air fed into the PSA system is 638 kJ/kg. As mentioned above, both PSA and membrane systems require additional air at a factor of 2-3 times the desired nitrogen flow rate. With a compressor efficiency of $\eta_{comp} = 0.85$ and an air mass flow rate of $\dot{m}_{air} = 2 * \dot{m}_{N_2} = 4.6e^{-3}kg/s$. This results in 3.45 kW of pumping power to compress the air required for nitrogen separation. Clearly, this is a huge problem since the energy required for the process is greater than the energy that is being stored.

While this is just a simplified calculation, it shows the scale of energy required for the separation of oxygen from the sweeping gas. This poses a challenge to the idea of the heat recuperation system. The sensible heat that the particles carry out of the reactor is approximately calculated by

$$Q_{solid} = \dot{m}_{solids} * c_{p,solids}\Delta T = 0.0025\frac{kg}{s} * 0.95\frac{kJ}{kgK} * 1475K = 3.5kW \tag{6.3}$$

If the heat recuperation gas production requires the same or more power than it can recuperate, the system is redundant and adds unnecessary equipment cost and complexity to the system.

These considerations warranted the search for an alternative gas to recuperate the sensible heat and sweep the oxygen out of the reduction zone. The main requirement for the gas was low oxygen partial pressure, energy efficient production or oxygen separation and no reaction with the MgMnO energy storage material.

6.4 Water Vapor as Sweeping Gas Candidate

Water vapor was investigated as a candidate. The high heat capacity of steam results in lower volumetric flow rates through the reactor and the condensation temperature of 100 °C allows for easy separation via condensation of the oxygen and steam. A chemical equilibrium calculation using the FactSage thermochemical software online tool *Equilib Web* determined that water vapor in chemical equilibrium with the MgMnO material has very low oxygen partial pressure of 3.51×10^{-4} atm at reduction temperature.

The oxygen partial pressure is much lower than the oxygen partial pressure in "industrial-grade" nitrogen which has a p_{O_2} of around 0.01-0.001 atm as part of the gas mixture. Figure 6.2 shows the relation between temperature, oxygen partial pressure and the extent of reduction according to the thermodynamic model from Bo et al. [33]. While the figure is not showing the reduction conditions (bottom right corner) in great detail, it can be seen that low oxygen partial pressures reduce the temperature needed for any selected extent of reduction compared to a higher pressure. The figure suggests that in order to reach a low y_{eq} (darker purple region), the p_{O_2} needs to be as low as possible or the temperature needs to be increased to achieve the same equilibrium value for a higher p_{O_2}. The low oxygen partial pressure and lack of reaction with the energy storage material makes steam a desirable candidate. To calculate the energy needed to produce steam from water

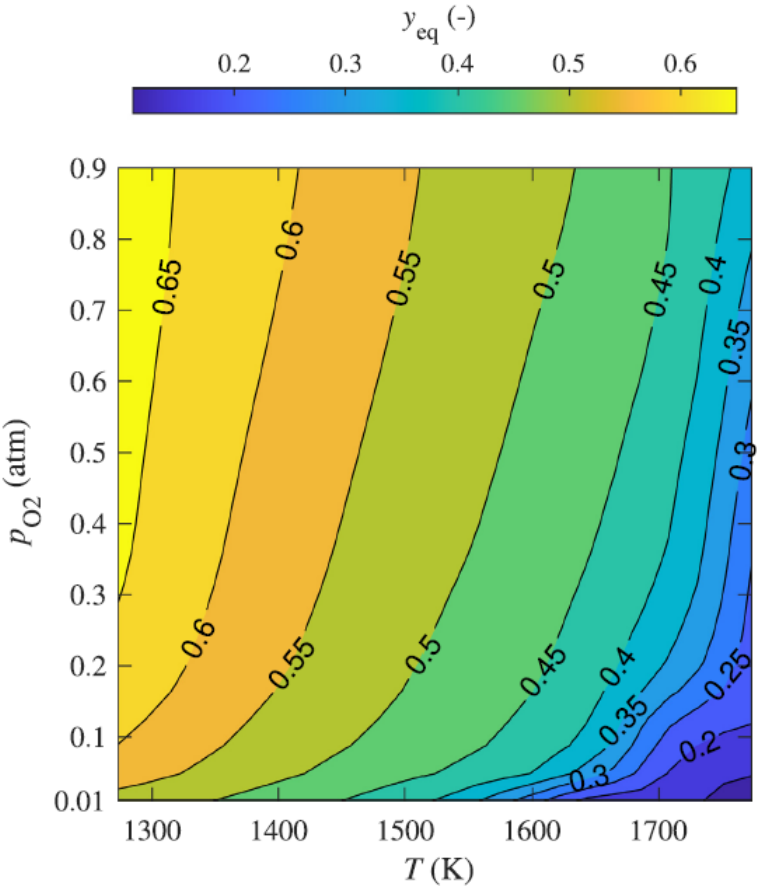

Figure 6.2 **Equilibrium Plot for MgMnO** MgMnO equilibrium plot depending on temperature and oxygen partial pressure. Smaller values for y_{eq} correspond to particles that are more fully charged. Reproduced with permission from [33]. Copyright 2022 Elsevier Science & Technology Journals.

for the reduction reaction, the heat capacity needs to be compared to that of MgMnO due to the heat recuperation criteria (Equation 3.5).

The heat capacity $c_{p,steam}$ changes drastically with temperature. Vasic et al. report values around 2.5 kJ/(kgK) at 1000 °C and 3.1 kJ/(kgK) at 1500 °C [70]. In 1936, Keyes et al. reported values around 1.9 kJ/(kgK) for steam at 100 °C [71]. Not much reliable data on the impact of temperature on MgMnO was found apart from what is reported in Chapter 2. The available data suggests that the heat capacity decreases slightly with temperature from 0.95 kJ/(kgK) (ambient to 1000 °C) to 0.89 kJ/(kgK) (1000 °C to 1500 °C).

To get an idea of the scale, it is sufficient to use the values of 2.5 kJ/(kgK) for steam and 0.95 kJ/(kgK) for MgMnO. Equation 3.5 shows that a ratio of 0.38 g/s steam per 1 g/s of energy

storage material is required to recuperate the sensible heat moving down out of the reduction zone. The specific energy needed to produce steam can be approximated from the evaporation enthalpy $h_{evap} = 2257kJ/kg$ [72] and the sensible heat required to heat the feed-water and superheat the steam.

$$e_{steam} = c_{p,water}(T_{boiling} - T_{feed}) + h_{evap} + c_{p,steam}(T_{out} - T_{boiling}) \tag{6.4}$$

Assuming a water feed temperature of 20 °C, a boiling point of 100 °C, a steam exit temperature of 150 °C, $c_{p,water} = 4.2kJ/(kgK)$, and $c_{p,steam} = 2.5kJ/(kgK)$, the specific energy is approximately 2688 kJ/kg. Using the same solid flow rate of 2.5 g/s as in the nitrogen example, we see that 2.5 kW are required to recuperate the sensible heat of a 2 kW reactor. This is less than the nitrogen, and later sections will consider ways to recuperate most of the energy in the steam via mechanical vapor recompression.

6.5 Experimental Validation of Steam Reduction Concept

An initial experimental setup was designed to investigate the hypothesis of using steam to reduce a small MgMnO sample. A concern for using water vapor was the possibility of water splitting at high temperatures which would cause a potentially explosive mixture of hydrogen and oxygen gas in the exhaust and use more energy. The goal for this first experiment was to ensure full reduction of the sample and no significant water splitting. Figure 6.3 shows the schematics of the setup.

A 20 g sample of MgMnO particles was loaded in a 40 mm alumina tube into a horizontal tube furnace. The alumina tube was sealed on both ends outside of the furnace using EQ-FL-40 sealing assembly from MTI. On the left side, the gases are connected to the tube and on the right side, a condenser and mass spectrometer are connected to analyze the exhaust gas composition. the setup was tested for leaks to ensure confidence in the results. The sample was fully oxidized by flowing a gas mixture of 0.9 atm oxygen and 0.1 atm nitrogen through the tube at 1000 °C for 10 hours. To prove the excellent reducing properties of steam, the sample was then heated up to 1500 °C and reduced under an atmosphere of 0.99 atm nitrogen and 0.01 atm oxygen. This mixture represents the industrial-grade nitrogen used for all previous reduction experiments as well as for the techno-economic model. As the sample reduces, the oxygen that is released is monitored by

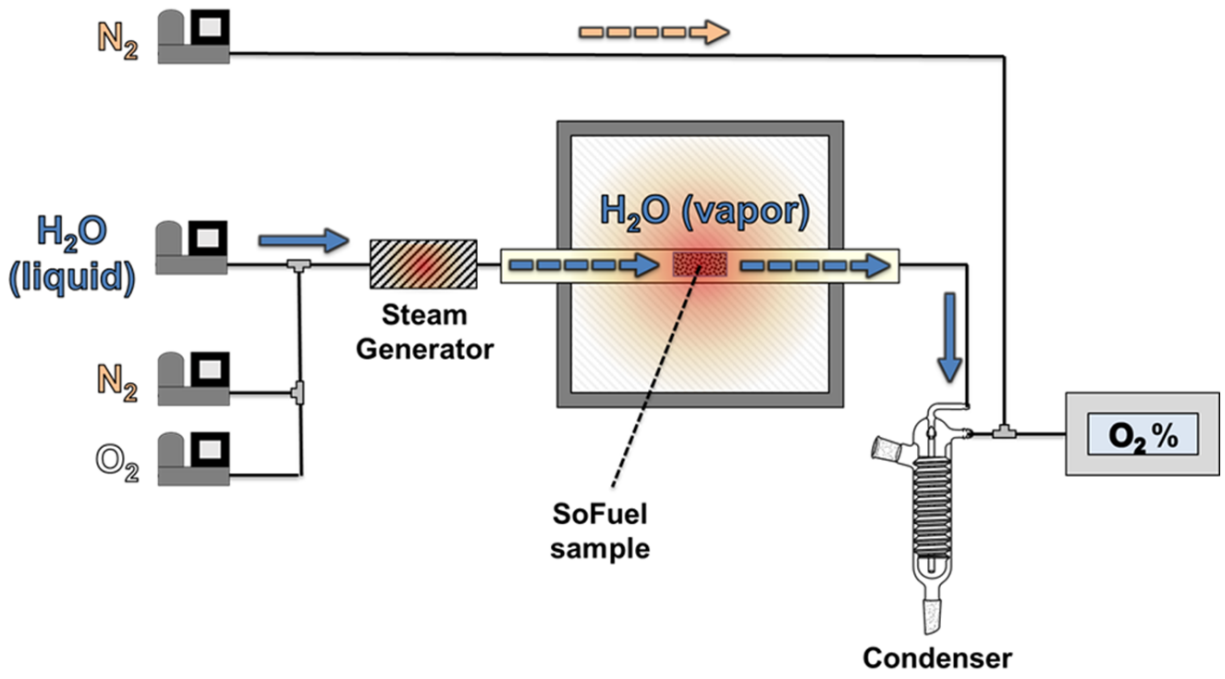

Figure 6.3 **Setup to Investigate Steam as Sweeping Gas** Experimental setup schematics to test effects of using steam as reducing agent. The schematics show the Alicat flow meters that control the gas and liquid flow rates, the steam generator, furnace, and sample as well as the condenser and mass spectrometer that was used to analyze the exhaust gasses.

the mass spectrometer. Once the sample reaches a reduction equilibrium, the mass spectrometer registered only the oxygen that is injected as part of the sweeping gas (1% of the total gas injected). At this point, 1 gram per second of liquid water is injected in the steam generator and enters the tube containing the sample. Due to the decrease in oxygen partial pressure in the tube, the sample reduces further, as expected from Figure 6.2.

The analysis of the exhaust gas (Figure 6.4) shows a spike of oxygen. The peak visualizes the further reduction of the sample under steam compared to industrial grade nitrogen, proving that at the same temperature, steam is a superior sweeping gas as the oxygen partial pressure is lower. Integrating the curve shows that approximately 190 ccm of oxygen were released which is about 20% of the total volume that can be released from a sample this size when it is cycled from fully oxidized to fully reduced. The values attained from the reduction experiment were validated with the thermodynamic model and match the expected increased extent of reduction.

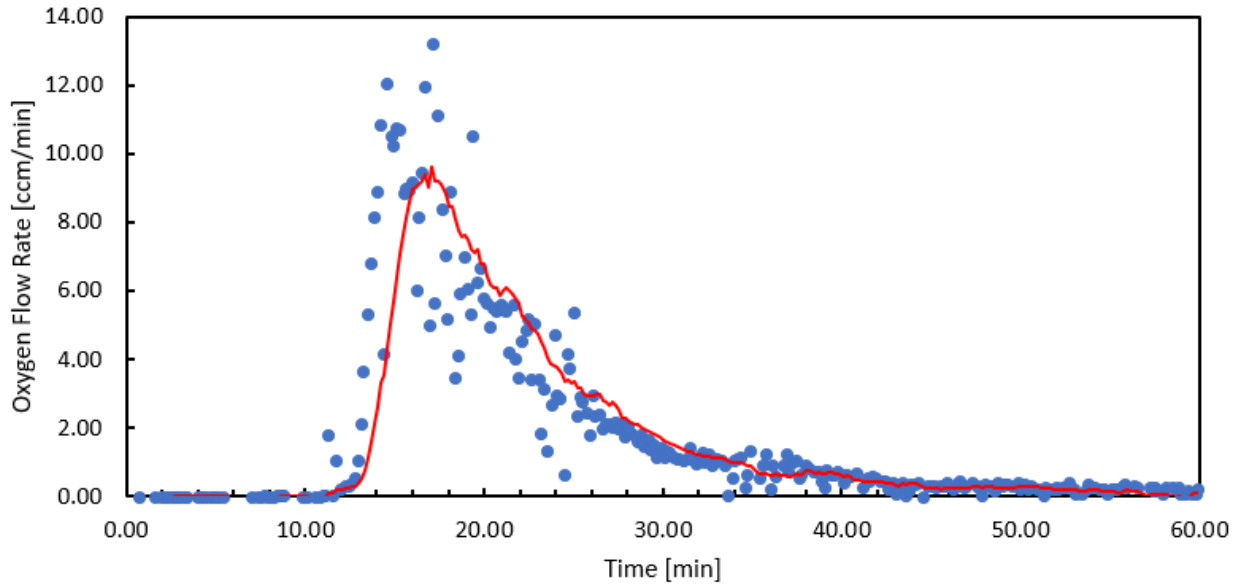

Figure 6.4 **Confirmation of Steam Reduction Hypothesis** The mass spectrometer registered oxygen released by the sample. The sample was fully reduced under industrial nitrogen before the steam was injected. Integration of the fitted curve (red) gives approximately 190 ccm of oxygen released.

6.6 Implementing Steam Reduction in Experimental Reactor

This encouraging result prompted the investigation of applying the steam reduction concept to the experimental reduction reactor. The first idea was to inject liquid water into the particle bed in the quenching zone and using the sensible heat of the particles to evaporate the water. The problem with that was that due to the high latent heat required to evaporate water, the mass flow rate of steam was low. Using the quenching as a heat source, Equation 6.4 can be used to calculate the mass flow rate of steam ($\dot{m}_s$). Here, $\dot{m}_{solids}$ denotes the particle mass flow, $c_{p,solid}$ and $c_{p,steam}$ are the specific heat of the particles and the steam and the temperature difference between the reduction zone and the particle outlet is $(T_{red} - T_{amb})$. h_{evap} is the latent heat of water which is approximately 2260 kJ/kg [72].

$$\dot{m}_{steam} = \frac{\dot{m}_{solid} c_{p,solid} (T_{red} - T_{amb})}{h_{evap} + c_{p,steam} (T_{red} - T_{amb})} \tag{6.5}$$

Equation 6.5 shows that the steam mass flow rate is 0.16 g/s for a particle flow rate of 2.5 g/s and reduction temperature of 1450 °C. However, for the same conditions, the required nitrogen flow rate would be 2.5 g/s. This poses a challenge for the function of sweeping the oxygen out of

the reduction zone. The oxygen released during reduction would amount to a much higher oxygen partial pressure in the low steam flow compared to the nitrogen. This is a step in the wrong direction of achieving a lower oxygen partial pressure with steam vs nitrogen.

Another disadvantage of the water injection is the difficulty of recuperating the latent heat of the steam into the particle bed. For full heat recuperation and sufficient preheating of the particles, the steam would need to be condensed in the particle bed which is challenging as it only happens at 100 °C and the sensible heat capacity of the particles going from ambient to 100 °C is much lower than the latent heat of the steam. Furthermore, due to the moving bed reactor, the condensed water would move down with the particles into the recuperation zone.

A better approach is to evaporate the water outside of the particle bed and introduce steam as the sweeping and recuperating gas. This allows for a higher steam flow rate which leads to lower oxygen partial pressures as well as sensible heat recuperation of the particles moving down.

The challenge with this approach is the sensible heat recuperation requirement. To ensure quenching and preheating of the particles, the gas flow needs to be precisely controlled as a lower flow would result in overheating of the particles below the reduction zone, damaging the collection tank seal. Also, insufficient preheating of the particles could lead to expansion clogging in the reduction zone. Likewise, an excess flow of steam would pull heat out of the reduction zone and overheat the incoming particles, damaging the particle feed system.

Most commercially available steam generators operate by submerging a heating element in a water reservoir and the amount of water evaporated is controlled by the power of the heater. A steam flow controller in combination with this conventional steam generator system is necessary to ensure the correct amount of steam enters the particle bed. This would add cost and a condensing point for the steam. Another issue with this design is that the conventional steam generator units are often not designed to operate under pressure and using a restriction to the steam flow entails the risk of pressure build up if more water is evaporated than is used.

A different approach is pursued here which consists of building a steam generator where the liquid water input is controlled so that the steam generator only evaporates the water that is added at

any given moment. This provides a constant flow of steam and can be easily controlled by a liquid flow controller at room temperature and doesn't require an expensive heated steam flow controller. Figure 6.5 shows the custom steam generator parts and finished product. The generator is built

Figure 6.5 **Steam Generator** The components of the steam generator (left), the assembled setup (center) and the insulated and wired assembly (right). This generator is capable of producing a controlled steam flow of up to 20 g/min.

using a 45 mm inner diameter stainless steel tube and threaded stainless steel end caps. The water is injected into the tube which is filled with stainless steel balls to increase the thermal capacity. The heat is provided by a 110 V 2000 W cartridge heater which is inserted into the generator. Two external 110 V 500 W rope heaters maintain a consistent temperature of the tubular steam generator. Three Omega Engineering CN9000N temperature controllers hold each heater at 150°C and a Alicat LC-series liquid flow controller injects a precise flow rate of water into the steam generator. The steam exits the generator through a stainless steel tube and enters the particle bed in the quenching zone.

The operating procedure of the experimental reactor had to be slightly changed to accommodate

the use of the steam instead of nitrogen as a sweeping gas. It is important to prevent the condensation of the steam in the quenching zone as this would cause insufficient gas flow for recuperation and also to moisture moving into the particle collection tank. To avoid this, the particle bed flow is started once the reduction zone reaches 1000 °C and a low nitrogen counter-flow is started. The nitrogen is too low for heat recuperation but used to maintain a reducing atmosphere. The furnace is maintained at 1000 °C as the particle bed moves down. The particles transport sensible heat down and preheat the quenching zone until the steam injection site reaches approximately 500 °C. At this point, the nitrogen flow is turned off and the steam injection is started. Then, the furnace temperature is ramped up to the target reduction temperature.

6.7 Steam Reduction Results

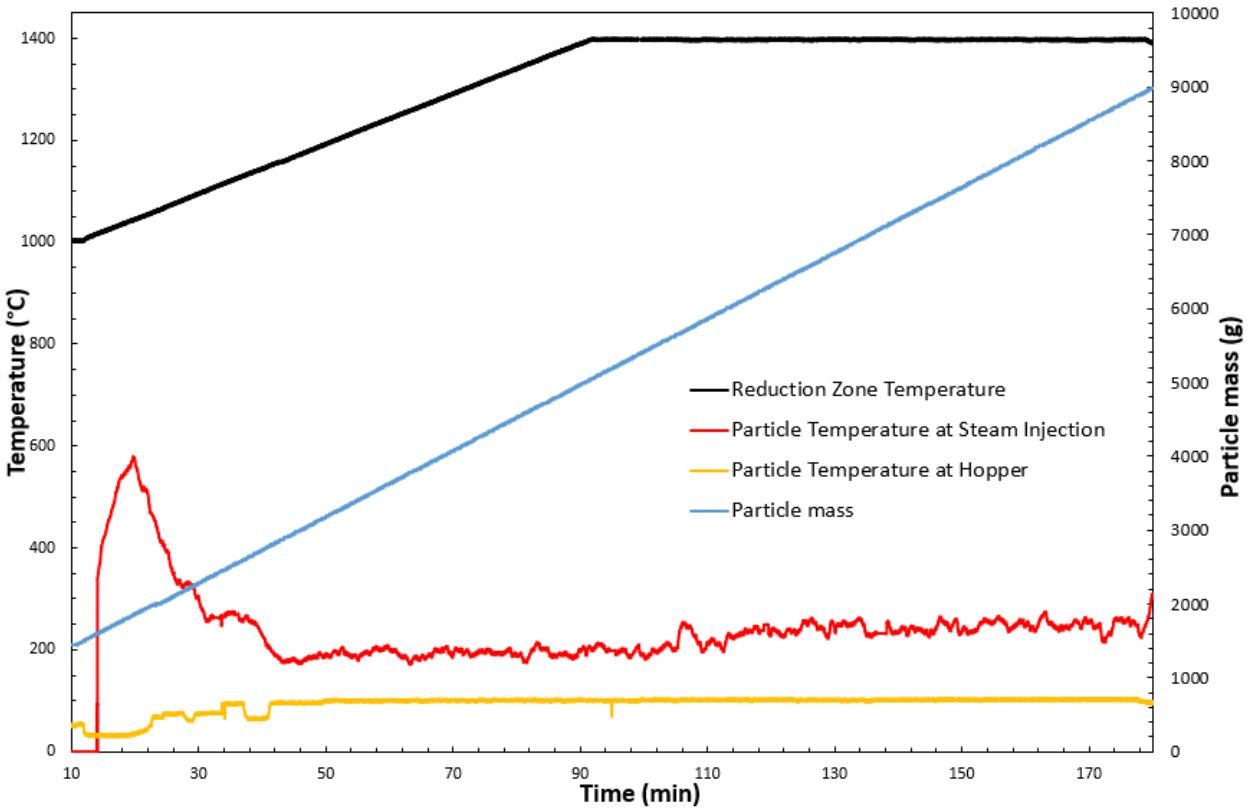

Figure 6.6 **Steam Reduction Data** Data from a reduction run using steam. The particle flow rate of 0.75 g/s was matched with a steam flow rate of 0.39 g/s.

Figure 6.6 shows data from a reduction run in the reactor using steam as counter-flow gas. The

black curve shows the furnace temperature which is increased from 1000 °C to 1400 °C. The blue line visualizes the particle mass in the collection tank which is a measure of the solid flow rate of 0.75 g/s. Those two parameters are the same as for a run with nitrogen and show no abnormalities. The red and yellow temperature profiles are unique to the steam experiment and worth further examination.

The red line shows the temperature of the particles at the steam injection port. As previously mentioned, the bed is started with a low nitrogen flow to preheat the quenching zone and prevent condensation of the steam. The sharp spike shows how effective the sensible heat preheating is as the temperature rises quickly. This also serves as a reminder of how important the recuperation flow is for protecting the steel collection tank and the silicone seal from the high temperatures of the particles exiting the reduction zone as the temperature quickly exceeds 400 °C. The steam injection is started around 20 minutes after the beginning of the data collection and cools the quenching zone to around 200 °C.

The yellow line visualizes the temperature at the particle inlet. The zone is at room temperature initially. One can observe that the temperature remains below 100 °C even after the steam injection is started. This indicates that the recuperation zone is colder due to the low nitrogen flow which was used to preheat the quenching zone. The steam condenses in the recuperation zone until the zone is heated up above 100 °C around minute 45 of the experiment. The steady temperature shows that the steam condenses close to the thermocouple which is situated in the particle hopper.

Both temperatures are mostly steady which indicates that steam is effective for heat recuperation. After the experiment, three samples of approximately 7 g of particles were analyzed in the TGA to determine the extent of reduction. The analysis shows that the steam, in addition to working as a heat recuperation gas, is very effective as a sweeping gas as the samples are fully reduced ($e_{p,TGA} = 0.95$) which cannot be achieved with nitrogen at 1400 °C.

An additional performance metric of interest was the flowability of the particle bed at high temperatures with a counter-flow of steam. Since the heat recuperation is the governing mechanism for the counter-flow gas, the mass flow rate of steam is lower than that of nitrogen due to the higher

heat capacity of steam compared to nitrogen [70].

Figure 6.7 shows a plot similar to Figure 3.10 where the fluidization limit is calculated for different solid flow rates and temperatures using Equations 3.10-3.12 and plotted as ratio of gas flow over solid flow. The figure shows much higher flowability limits compared to nitrogen. This

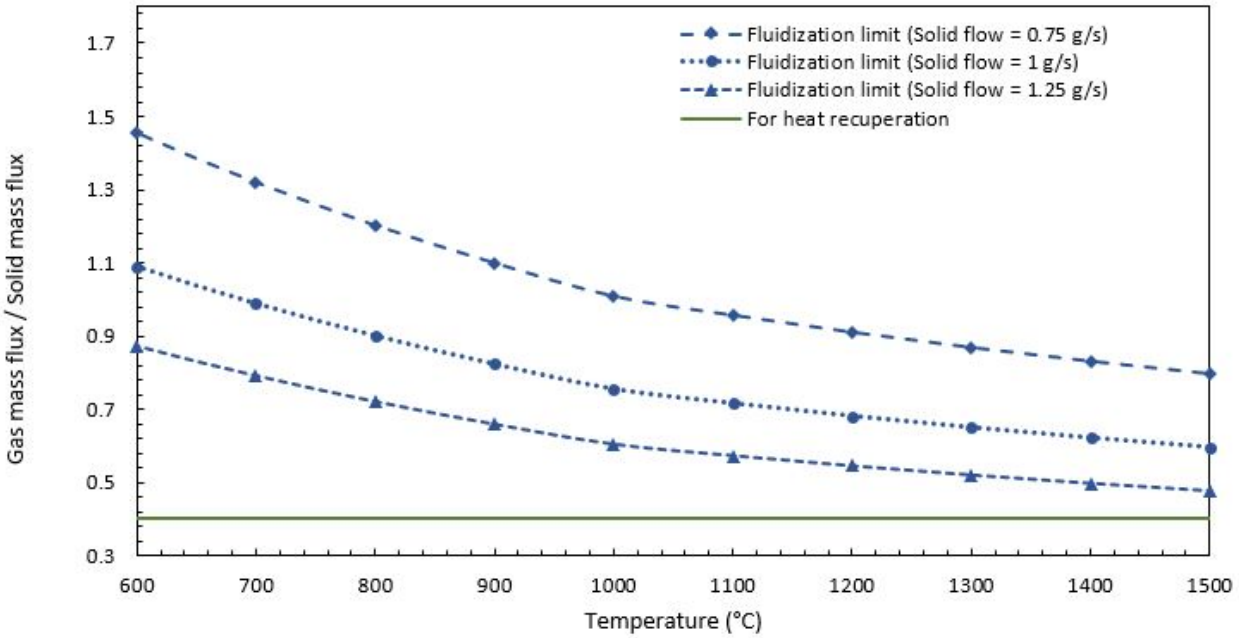

Figure 6.7 **Fluidization Limit Steam** Theoretical fluidization onset for different ratios of gas and particle flow rates at increasing temperature. It can be observed that the recuperation principle induces no fluidization at high temperatures when using steam and solid flow rates of up to 1.25 g/s. This is a big difference to the result of the nitrogen calculation which show fluidization above 1 g/s

calculation is supported by the successful omission of the gas pulsing during the steam experiment. As mentioned, the nitrogen reduction experiments were run with a pulsing nitrogen stream to give the bed a period no counter-low flow which enabled batch flow, preventing clogging due to bed lifting. The steam runs were conducted with a constant steam flow since the calculations suggested no fluidization issues and pulsation would require a flow controller between the steam generator and the reactor.

6.8 Latent Heat Recuperation

Section 6.4 introduces the energy calculation for evaporating water to produce clean steam as a sweeping gas. The high latent heat cost of the phase change from water to steam makes this system not economical. If the steam is vented to the atmosphere, the storage reactor would need to be scaled twice as large to offset the energy loss. The proposed solution to this issue is to recuperate as much of the latent heat in the steam as possible. Mechanical vapor recompression (MVR) systems (sometimes also referred to as mechanical vapor compression) have been shown to be effective at recovering substantial amounts of the latent heat of used steam in order to produce clean steam.

MVR systems are often used in industries where a feed of water mixed with a secondary substance needs to be concentrated by evaporation. The steam that is produced during the evaporation is compressed and then condensed in a heat exchanger which provides the heat for the evaporation of the water in the feed [73, 74]. Han et al. developed and tested an intermittent evaporator using MVR that provides 200 kg/h steam and shows 73% energy reduction compared to simple boiling [75]. Becker et al. report up to 90 % energy savings in their theoretical work [76].

MVR systems use the relationship between condensation temperature and pressure to recuperate latent heat of used steam. As the pressure of water vapor increases, the condensation temperature increases too. This enables condensation of the used steam in a heat exchanger that provides heat for the evaporation of the feed. As mentioned above, this process is used in industries where large amounts of water need to be evaporated in order to concentrate a feed. Using this system to produce clean steam sweep gas poses a novel idea due to some difference in the two processes: The ordinary MVR evaporates water with contaminants which usually leads to lower evaporation temperatures of 60-80 °C [73]. The proposed system would evaporate a feed of pure water at 2 bar with a boiling point of 120 °C.

Due to the low boiling point of the contaminated water, the ordinary MVR systems have low pressure ratio compression while this new system would require a multi-stage high pressure ratio compressor to increase the pressure and condensation temperature. This is necessary for adequate heat transfer between the condensing steam and the boiling feed in the heat exchanger.

The process schematics are shown in Figure 6.8. Saturated water is fed into a boiler at 2 bar. The boiler/heat exchanger produces pure steam that is introduced into the reactor. The steam recuperates the sensible heat of the particles and sweeps the oxygen released during reduction. The top of the reactor is sealed and the used steam is exhausted to the right. A multi-stage high pressure ratio compressor increases the pressure and enthalpy of the steam and feeds it into the condenser/boiler. Here, the steam condenses at a temperature of 150 °C and gives the latent heat off to the incoming saturated fresh water that is evaporated.

A simple thermodynamic investigation reveals the potential of the recompression system for latent heat recuperation in this case. Similar to the nitrogen compression calculations, an isentropic compression is assumed and penalized with a compressor efficiency. The steam tables [72] or a T-s diagram for water vapor is used to find the isentropic enthalpy of the compressed steam, $h_{4,s} = 3039\frac{kJ}{kg}$. The compressor power required for compression of the steam can be calculated using a projected compressor efficiency of 80% [77] and Equation 6.6. Figure 6.8 can be used to compare the temperatures and values at the different states of the process.

$$h_4 = h_3 + \frac{h_{4,s} - h_3}{\eta} = 2772.5\frac{kJ}{kg} + \frac{3039\frac{kJ}{kg} - 2772.5\frac{kJ}{kg}}{0.8} = 3105.6\frac{kJ}{kg} \tag{6.6}$$

At a pressure of 5 bar, the steam tables show an extrapolated temperature of approximately 320 °C for the compressed steam. The compression power can be calculated with

$$P_{comp} = \dot{m}_{steam} * \Delta h_{actual} = 0.00095\frac{kg}{s}\frac{1}{0.8}(3039/frackJkg - 2772.5\frac{kJ}{kg}) = 0.32kW \tag{6.7}$$

The compressor increases the enthalpy of the used steam to $3105.6\frac{kJ}{kg}$. This steam at 5 bar condenses at 150°C. The saturated water at 5 bar has and enthalpy of $h_{5,L} = 640\frac{kJ}{kg}$. The enthalpy difference in the condenser of $2465\frac{kJ}{kg}$ is used to evaporate incoming saturated water at 2 bar which requires an enthalpy difference of $2265\frac{kJ}{kg}$. The remaining enthalpy difference of the condensing steam is required to superheat the fresh steam from 120°C saturation point to 150°C injection temperature. This requires approximately $232\frac{kJ}{kg}$. It is likely that heat losses in the system require a heater in the evaporator to add energy to the fresh steam.

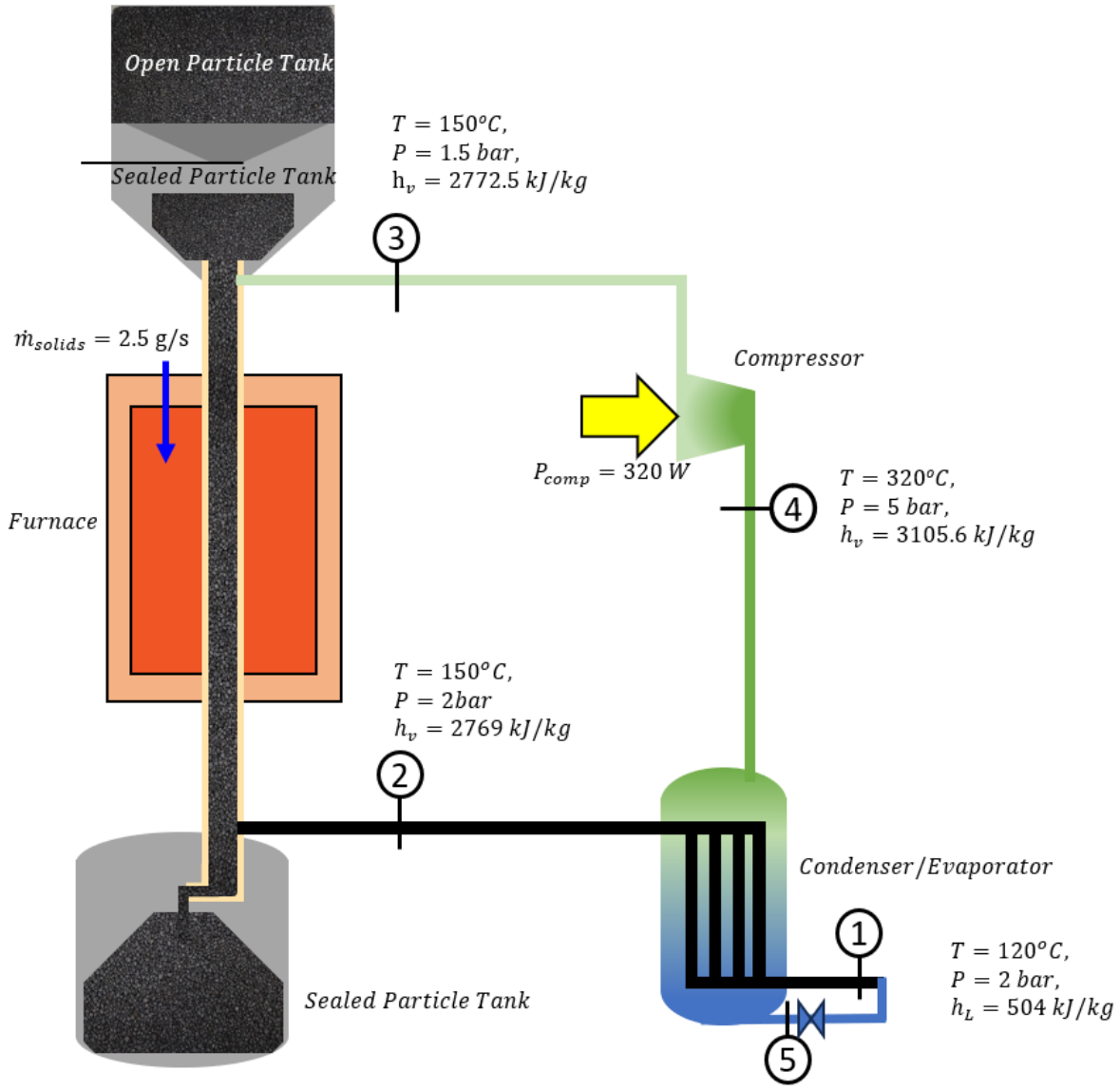

Figure 6.8 **Schematics for Recuperation of Latent Heat in Steam** Mechanical vapor recompression cycle proposed to save energy when using steam. Fresh steam (2) is produced from feed water coming in at (1). The steam flows counter-currently through the reduction reactor and pick up oxygen. A compressor sucks in and compresses the used steam from (3)-(4). The compressor power is calculated to around 540 W. The pressurized used steam is condensed in the heat exchanger, providing heat to evaporate the incoming feed water.

This means that, ignoring heat losses, the proposed MVR system is able to produce a flux of water vapor sufficient for the sensible heat recuperation of the solid mass flux of 2.5 g/s of the energy storage material at an energy cost of $0.32kW$ compared to the pure evaporation power of $2.5kW$ and the estimated nitrogen separation work of $3.4kW$.

For ease of calculating a scale up, the MVR system can be described based on the solid particle

flow rate. The compression has an enthalpy difference of

$$\Delta h_{comp} = 333 \frac{kJ}{kg_{steam}} * 0.38 \frac{kg_{steam}}{kg_{solid}} = 126.5 \frac{kJ}{kg_{solid}} \tag{6.8}$$

It is important to remember that this is an estimation using assumptions such as a compressor efficiency and a perfect heat exchanger as well as neglecting heat losses which will be present in the steam loop. However, this estimation is helpful in showing the potential energy savings of using water vapor as a heat recuperation and sweeping gas and producing the steam with a MVR cycle.

6.9 Summary of Water Vapor as Heat Recuperation Gas

This chapter analyzed the energy penalty associated with the separation of oxygen from the sweep gas. It was found that nitrogen purification has high energy demands due to the high gas flow rates and high pressures required for the separation. Investigating steam as alternative heat recuperation gas found superior reducing qualities of steam compared to nitrogen and a thermodynamic analysis of a MVR recuperation system promises much lower energy cost for using steam over nitrogen as the process gas.

CHAPTER 7

CONCLUSION

This work explained in detail the conception, design, operation, and continuous development of the high-temperature MgMnO energy storage material charging reactor. The storage material undergoes a reduction reaction as it releases oxygen at 1500 °C and an atmosphere with low oxygen partial pressure. This reaction charges the material with a chemical potential that can be released by oxidizing the material under air at temperatures around 1000 °C. The abundant availability of the materials and the high energy storage density of 1172 ± 110 MJm^{-3} as well as proven cyclic stability over many cycles and high reaction temperatures make this material a great candidate for short and long duration renewable energy storage.

The innovation of the reactor concept discussed here is a continuous moving bed with counter-currently flowing sweep gas. The continuous movement of energy storage material enables continuous storage of energy while it is available. The counter-flowing gas is controlled in a way that prevents sensible heat loss across the inlet and outlet of the reactor. This is achieved as the gas quenches the particles exiting the reactor and pre-heating the particle entering the reactor. Therefore, all streams enter and exit the reactor close to ambient conditions.

The development of the moving bed reactor concept began with the consideration of particle size. Analysis of the trade-offs between different particle diameters show an optimization problem where a smaller particle size favors faster chemical conversion due to smaller diffusion pathways in the particle while larger diameters improve the radiative heat transfer into the particle bed. First experiments were conducted with 1 mm particles and a sheet-metal collection tank using a scale, piston style particle flow controller and a 25 mm diameter alumina tube in a small tube furnace (Fig 3.6).

Due to bed sintering, bigger particles were produced and a bigger setup was built, now using a pressure vessel as particle collection tank and a pneumatic l-valve attached to a 50 mm alumina tube. With this setup we learned how to control the bed at high temperatures and where the bottlenecks for a better performance of the reactor were. The first version of the successful setup was capable

of producing a chemical energy flux $Q_{chem} = 455 kW/m^2$ with a solid flow rate of 1.25 g/s energy storage material.

Improvements such as the addition of a gas bypass system to the reactor and a further increase in particle size to 5.5 mm helped achieve a chemical energy flux of 675 kW/m^2 at a solid flow rate of 2.5 g/s. Simulation showed a problem with heat-transfer into the center of the particle bed caused by the shorter residence time. A longer heated zone was simulated and the modified experimental reactor produced a record 1.2 MW/m^2 at a solid flow rate of 3 g/s and a reduction temperature of 1500 °C.

The adaptation of a steam generator to the system proved the possibility of reducing the particles in a steam atmosphere instead of nitrogen. The higher extend of reduction of the particles reduced in steam vs nitrogen proves the lower oxygen partial pressure is elemental for full conversion of the particles. The high cost of nitrogen generation equipment and the high energetic cost of pressure swing adsorption (PSA) separation of nitrogen and oxygen makes steam reduction a competitive alternative to using nitrogen in a scaled-up reactor.

This setup and experimental campaign allowed us to conduct experiments under conditions never-before investigated in any published research. Flowing a packed particle bed at 1500 °C is without a doubt a world-record in itself but doing so with a reactive particle bed and being able to fine-tune the reactor to improve the reaction conditions is a major accomplishment.

7.1 Proposed Future Work

The previous chapters explained in detail the advantages of the MgMnO moving bed charging reactor for renewable energy storage. They explored challenges in building and running a lab-scale reactor as well as improvements to the original concept. The following section looks at ideas and potential challenges of future developments of this technology.

7.1.1 Scale-Up

MgMnO is a promising TCES material candidate. The continuous moving bed reactor with gas counterflow concept has been shown to work well and charge the material effectively and efficiently. A parallel oxidation reactor has proven that the recovery of high-temperature heat from

the energy storage material is possible. These advantages are reasons to investigate the potential of this material and concept on a larger scale. Zhao et al. developed a techno-economic model to study the scale-up (not yet published). The authors point out that many assumptions needed to be made because of a lack of comparable large-scale facilities due to the novelty of the concept. They used experimental data from the here presented reactor to validate their model and used early efficiencies of the system of 40%. A sensitivity analysis showed that accurate, improved efficiencies for the charging and especially the discharging reactor have a big impact on reducing the calculated levelized cost of storage, LCOS. Even with this conservative estimate of the potential of this technology, the authors found that a levelized cost of around 0.06$/kWh could be achieved in a 100 MW CSP plant.

Building and operating a larger experimental reactor set for the charging and discharging of the material is imperative to reduce the big uncertainties in the scale-up study and for future use cases. The main energy loss that keeps the efficiency of the lab-scale reactors low is heat loss. A larger reactor cavity is more easily insulated which would reduce the heat loss and improve the efficiency. As the volume of the cavity increases, the ratio of surface-area to volume decreases, limiting the heat loss potential. A look at Fourier's law of heat conduction (Equation 7.1) shows that the heat loss is proportional to the surface-area of the reactor.

$$\dot{Q}_x = -kA\frac{dT}{dx} \tag{7.1}$$

Future applications range from grid-scale renewable electricity storage to the decarbonization of industrial processes requiring high-grade heat such as steel, cement, glass and other processes. Another interesting application is the proposal of using the reactor on the lunar surface. The moon is covered with lunar regolith, a mixture of minerals which contains considerable amounts of titanium dioxide, iron oxide and magnesium oxide [78]. A solar-powered continuous moving bed reduction reactor could be used to produce oxygen and pure metals for a lunar base and future explorations.

7.1.2 Future Challenges

Scaling up the reduction reactor poses a number of forseeable and unforseeable challenges. Problems that need to be solved when one tries to build a bigger reactor depend on the intended scale. A grid-scale plant design warrants its own dissertation. For a larger proof of concept reactor on the scale of 10-20 kW, which would be an 5-10x increase in storage rate, the following issues need to be overcome:

- The sweeping gas needs to be accounted for. The recuperation criteria of the reactor is a key innovation that enables low sensitive heat loss and high efficiency operation. However, a large gas flow rate is required to recuperate the heat. This caused fluidization issues in the reaction zone which were solved by inserting a bypass tube into the particle bed and pulsing the gas flow to allow the bed to move. Refer to Chapter 4 for details on the problem and its solution.

  Another problem is the separation of the oxygen from the sweeping gas. Low oxygen partial pressure is required in the sweeping gas to support the release of oxygen from the material. However, oxygen separation equipment is expensive and the process requires energy. Chapter 6 shows that approximately 170% of the stored power is needed to produce the large amount of nitrogen gas needed to fulfill the heat recuperation criteria. This reduces the potential system efficiency below 40% and defeats the purpose of the sensible heat recuperation. A different method of nitrogen generation that is more efficient is cryogenic rectification. Equipment for this is not easily available which makes a cost analysis complicated. However, a study of this option is encouraged as a more energy-efficient solution for a scaled-up reactor is imperative.

  An alternative to using nitrogen, which is shown in Chapter 6, is to use steam as sweeping gas. This approach was tested successfully with the 2 kW reactor. However, the huge energy penalty of evaporating water requires a heat recuperation system of its own which needs to be evaluated in detail and tested. Simplified calculations show that the power required for the production of clean steam could be as low as 15% of the stored power.

- The reactor tube diameter restriction. Chapters 4 & 5 point out that the chemical storage flux, which is a performance metric of the reactor, is limited by different factors. The fluidization of the particle bed which is caused by the upwards flowing sweep gas, restricts the maximum flow rate of the energy storage material in the reactor. The residence time of the particles needs to be sufficient for full conversion, further limiting the throughput of material. The residence time is largely governed by the radial penetration of heat into the bed. The heat penetration restricts the reactor diameter to approximately 50 mm. The maximum chemical energy flux that has been demonstrated in the experimental reactor was 1.2 MW/m^2. Therefore, the reactor tube diameter of 50 mm results in a maximum chemical storage power of around 2.5 kW per tube. A scale-up to 10 kW would need 4 tubes instead of a single larger tube to feed the particles through the reactor. This means that a 10 MW scale reactor using this design would require 4000 tubes. The particle and gas flow control of multiple tubes is one of the challenges that needs to be explored and solved.

- The heat transfer into the particle bed. A study of the radial heat transfer mechanism is recommended to explore options of larger tube diameters. The reactor tube material alumina has a low heat conduction rate and low emissivity, possibly restricting the heat transfer into the tube [79, 80]. Finding the bottleneck of heat transfer in radial direction could enable a solution with the potential of increasing the tube diameter, improving bed flowability and scalability of the concept.

- Energy density of the material. The idea of reusing the material for many cycles implies transporting the material back and forth between the charging reactor, which would be most at home in a remote location with high solar radiation year-round to the discharge reactor. The discharge reactor must be in a location such that the costs of transport and the electrical transmission losses are optimized. To decrease the cost of transportation, possibilities to increase the energy density need to be investigated by simulating and experimenting with doping the material with different molecules to increase the energy storage capabilities.

These are some of the major challenges facing the next developmental stage of this technology. There will be many more issues to solve as they reveal themselves on the path of bringing this promising technology one step closer to solving the energy crisis of the current time.

BIBLIOGRAPHY

[1] O. Palizban and K. Kauhaniemi, "Energy storage systems in modern grids—matrix of technologies and applications," vol. 6, pp. 248–259. [Online]. Available: https://linkinghub.elsevier.com/retrieve/pii/S2352152X1630010X

[2] J. Yin, A. Molini, and A. Porporato, "Impacts of solar intermittency on future photovoltaic reliability," vol. 11, no. 1, p. 4781, publisher: Nature Publishing Group. [Online]. Available: https://www.nature.com/articles/s41467-020-18602-6

[3] California iso energy database. [Online]. Available: https://www.caiso.com/TodaysOutlook/Pages/supply.aspx

[4] M. A. Gonzalez-Salazar, T. Kirsten, and L. Prchlik, "Review of the operational flexibility and emissions of gas- and coal-fired power plants in a future with growing renewables," vol. 82, pp. 1497–1513. [Online]. Available: https://www.sciencedirect.com/science/article/pii/S1364032117309206

[5] Customer-sited renewable energy generation. EPUC Energy Division. [Online]. Available: https://www.cpuc.ca.gov/industries-and-topics/electrical-energy/demand-side-management/customer-generation

[6] H. B. Piotr Bojek. (2022) Concentrated solar power (csp), iea, paris, license: Cc by 4.0. [Online]. Available: https://www.iea.org/reports/concentrated-solar-power-csp

[7] S. R. Wenham, M. A. Green, M. E. Watt, R. Corkish, and A. Sproul, *Applied photovoltaics*. Routledge, 2013.

[8] H. Ibrahim, A. Ilinca, and J. Perron, "Energy storage systems—characteristics and comparisons," vol. 12, no. 5, pp. 1221–1250. [Online]. Available: https://linkinghub.elsevier.com/retrieve/pii/S1364032107000238

[9] K. Divya and J. Østergaard, "Battery energy storage technology for power systems—an overview," vol. 79, no. 4, pp. 511–520. [Online]. Available: https://linkinghub.elsevier.com/retrieve/pii/S0378779608002642

[10] S. Mekhilef, R. Saidur, and A. Safari, "Comparative study of different fuel cell technologies," vol. 16, no. 1, pp. 981–989. [Online]. Available: https://linkinghub.elsevier.com/retrieve/pii/S1364032111004709

[11] S. Rehman, L. M. Al-Hadhrami, and M. M. Alam, "Pumped hydro energy storage system: A technological review," vol. 44, pp. 586–598. [Online]. Available: https://linkinghub.elsevier.com/retrieve/pii/S1364032115000106

[12] G. Alva, Y. Lin, and G. Fang, "An overview of thermal energy storage systems,"

vol. 144, pp. 341–378. [Online]. Available: https://linkinghub.elsevier.com/retrieve/pii/S036054421732056X

[13] A. Palacios, C. Barreneche, M. Navarro, and Y. Ding, "Thermal energy storage technologies for concentrated solar power – a review from a materials perspective," vol. 156, pp. 1244–1265. [Online]. Available: https://linkinghub.elsevier.com/retrieve/pii/S0960148119316258

[14] G. P. Thiel and A. K. Stark, "To decarbonize industry, we must decarbonize heat," *Joule*, vol. 5, no. 3, pp. 531–550, 2021.

[15] M. Pisciotta, H. Pilorgé, J. Feldmann, R. Jacobson, J. Davids, S. Swett, Z. Sasso, and J. Wilcox, "Current state of industrial heating and opportunities for decarbonization," vol. 91, p. 100982. [Online]. Available: https://www.sciencedirect.com/science/article/pii/S0360128521000800

[16] C. Prieto, P. Cooper, A. I. Fernández, and L. F. Cabeza, "Review of technology: Thermochemical energy storage for concentrated solar power plants," vol. 60, pp. 909–929. [Online]. Available: https://linkinghub.elsevier.com/retrieve/pii/S1364032116001830

[17] X. Chen, Z. Zhang, C. Qi, X. Ling, and H. Peng, "State of the art on the high-temperature thermochemical energy storage systems," vol. 177, pp. 792–815. [Online]. Available: https://www.sciencedirect.com/science/article/pii/S0196890418311117

[18] J. Sunku Prasad, P. Muthukumar, F. Desai, D. N. Basu, and M. M. Rahman, "A critical review of high-temperature reversible thermochemical energy storage systems," vol. 254, p. 113733. [Online]. Available: https://linkinghub.elsevier.com/retrieve/pii/S0306261919314205

[19] G. Airò Farulla, M. Cellura, F. Guarino, and M. Ferraro, "A review of thermochemical energy storage systems for power grid support," vol. 10, no. 9, p. 3142. [Online]. Available: https://www.mdpi.com/2076-3417/10/9/3142

[20] M. Gambini, "Metal hydride energy systems performance evaluation. part a: Dynamic analysis model of heat and mass transfer," vol. 19, no. 1, pp. 67–80. [Online]. Available: https://www.sciencedirect.com/science/article/pii/0360319994901791

[21] M. Bhouri, I. Bürger, and M. Linder, "Feasibility analysis of a novel solid-state h2 storage reactor concept based on thermochemical heat storage: MgH2 and mg(OH)2 as reference materials," vol. 41, no. 45, pp. 20 549–20 561. [Online]. Available: https://www.sciencedirect.com/science/article/pii/S0360319916328233

[22] Y. A. Criado, M. Alonso, J. C. Abanades, and Z. Anxionnaz-Minvielle, "Conceptual process design of a CaO/Ca(OH)2 thermochemical energy storage system using fluidized bed reactors," *Applied Thermal Engineering*, vol. 73, no. 1, pp. 1087–1094, Dec. 2014. [Online]. Available: https://www.sciencedirect.com/science/article/pii/S1359431114007613

[23] J. M. Bergthorson, "Recyclable metal fuels for clean and compact zero-carbon power,"

vol. 68, pp. 169–196. [Online]. Available: https://www.sciencedirect.com/science/article/pii/S0360128518300327

[24] M. Baigmohammadi, W. Prasidha, N. C. Stevens, Y. L. Shoshyn, T. Spee, and P. de Goey, "Towards utilization of iron powders for heating and power," vol. 13, p. 100116. [Online]. Available: https://www.sciencedirect.com/science/article/pii/S2666352X23000055

[25] G. Karagiannakis, C. Pagkoura, E. Halevas, P. Baltzopoulou, and A. G. Konstandopoulos, "Cobalt/cobaltous oxide based honeycombs for thermochemical heat storage in future concentrated solar power installations: Multi-cyclic assessment and semi-quantitative heat effects estimations," *Solar Energy*, vol. 133, pp. 394–407, Aug. 2016. [Online]. Available: https://www.sciencedirect.com/science/article/pii/S0038092X16300652

[26] K. Randhir, K. King, N. Rhodes, L. Li, D. Hahn, R. Mei, N. AuYeung, and J. Klausner, "Magnesium-manganese oxides for high temperature thermochemical energy storage," vol. 21, pp. 599–610. [Online]. Available: https://linkinghub.elsevier.com/retrieve/pii/S2352152X18303281

[27] K. King, K. Randhir, and J. Klausner, "Calorimetric method for determining the thermochemical energy storage capacities of redox metal oxides," *Thermochimica Acta*, vol. 673, pp. 105–118, Mar. 2019. [Online]. Available: https://linkinghub.elsevier.com/retrieve/pii/S0040603118306014

[28] K. Hans Wedepohl, "The composition of the continental crust," vol. 59, no. 7, pp. 1217–1232. [Online]. Available: https://www.sciencedirect.com/science/article/pii/0016703795000382

[29] K. Randhir, M. Hayes, P. Schimmels, J. Petrasch, and J. Klausner, "Zero carbon solid-state rechargeable redox fuel for long duration and seasonal storage," *Joule*, vol. 6, no. 11, pp. 2513–2534, Nov. 2022. [Online]. Available: https://linkinghub.elsevier.com/retrieve/pii/S2542435122004846

[30] N. Rahmatian, A. Bo, K. Randhir, J. F. Klausner, and J. Petrasch, "Bench-scale demonstration of thermochemical energy storage using the magnesium-manganese-oxide redox system," vol. 45, p. 103682. [Online]. Available: https://www.sciencedirect.com/science/article/pii/S2352152X21013566

[31] J. Ortiz-Ulloa, L. Freiberg, F. Lei, O. Ramsey, D. Korba, M. Hayes, P. Schimmels, K. Randhir, L. Li, J. Petrasch, J. F. Klausner, and N. AuYeung, "Development and testing of a novel combined moving-fluidized bed oxidation reactor for efficient high-temperature discharge of thermochemical energy storage particles." AIChE. [Online]. Available: https://aiche.confex.com/aiche/2023/meetingapp.cgi/Paper/665125

[32] H. B. Dizaji and H. Hosseini, "A review of material screening in pure and mixed-metal oxide thermochemical energy storage (TCES) systems for concentrated solar power (CSP) applications," vol. 98, pp. 9–26. [Online]. Available: https:

//www.sciencedirect.com/science/article/pii/S136403211830652X

[33] A. Bo, K. Randhir, N. Rahmatian, J. Klausner, and J. Petrasch, "Chemical equilibrium of the magnesium manganese oxide redox system for thermochemical energy storage," vol. 259, p. 117750. [Online]. Available: https://linkinghub.elsevier.com/retrieve/pii/S0009250922003347

[34] M. Hayes, F. Masoomi, P. Schimmels, K. Randhir, J. Klausner, and J. Petrasch, "Ultra-high temperature thermal conductivity measurements of a reactive magnesium manganese oxide porous bed using a transient hot wire method," vol. 143, no. 10, p. 104502. [Online]. Available: https://asmedigitalcollection.asme.org/heattransfer/article/143/10/104502/1115650/Ultra-High-Temperature-Thermal-Conductivity

[35] PubChem. Manganese(II) oxide. [Online]. Available: https://pubchem.ncbi.nlm.nih.gov/compound/14940

[36] PubChem . Magnesium oxide. [Online]. Available: https://pubchem.ncbi.nlm.nih.gov/compound/14792

[37] J. Zhao, D. Korba, A. Mishra, J. Klausner, K. Randhir, N. AuYeung, and L. Li, "Particle-based high-temperature thermochemical energy storage reactors," vol. 102, p. 101143. [Online]. Available: https://www.sciencedirect.com/science/article/pii/S0360128524000017

[38] H. S. Cho, N. Gokon, T. Kodama, Y. H. Kang, and H. J. Lee, "Improved operation of solar reactor for two-step water-splitting h2 production by ceria-coated ceramic foam device," vol. 40, no. 1, pp. 114–124. [Online]. Available: https://www.sciencedirect.com/science/article/pii/S0360319914029243

[39] S. Abanades, P. Charvin, and G. Flamant, "Design and simulation of a solar chemical reactor for the thermal reduction of metal oxides: Case study of zinc oxide dissociation," vol. 62, no. 22, pp. 6323–6333. [Online]. Available: https://www.sciencedirect.com/science/article/pii/S0009250907005878

[40] W. R. Blevin and W. J. Brown, "A precise measurement of the stefan-boltzmann constant," vol. 7, no. 1, p. 15. [Online]. Available: https://dx.doi.org/10.1088/0026-1394/7/1/003

[41] I. Yasuda and T. Hikita, "Precise Determination of the Chemical Diffusion Coefficient of Calcium-Doped Lanthanum Chromites by Means of Electrical Conductivity Relaxation," *Journal of The Electrochemical Society*, vol. 141, no. 5, pp. 1268–1273, May 1994. [Online]. Available: https://iopscience.iop.org/article/10.1149/1.2054908

[42] C. K. Ho, J. M. Christian, J. Yellowhair, K. Armijo, W. J. Kolb, S. Jeter, M. Golob, and C. Nguyen, "Performance Evaluation of a High-Temperature Falling Particle Receiver," in *Proceedings of the ASME 2016 10th International Conference on Energy Sustainability*. Charlotte, North Carolina, USA: American Society of Mechanical Engineers, Jun. 2016, p.

V001T04A006. [Online]. Available: https://asmedigitalcollection.asme.org/ES/proceedings/ES2016/50220/Charlotte,%20North%20Carolina,%20USA/231237

[43] W. Wu, D. Trebing, L. Amsbeck, R. Buck, and R. Pitz-Paal, "Prototype Testing of a Centrifugal Particle Receiver for High-Temperature Concentrating Solar Applications," *Journal of Solar Energy Engineering*, vol. 137, no. 4, p. 041011, Aug. 2015. [Online]. Available: https://asmedigitalcollection.asme.org/solarenergyengineering/article/doi/10.1115/1.4030657/379211/Prototype-Testing-of-a-Centrifugal-Particle

[44] S. M. Olhero, P. M. C. Torres, J. Mesquita-Guimarães, J. Baltazar, J. Pinho-da Cruz, and S. Gouveia, "Conventional *versus* additive manufacturing in the structural performance of dense alumina-zirconia ceramics: 20 years of research, challenges and future perspectives," vol. 77, pp. 838–879. [Online]. Available: https://www.sciencedirect.com/science/article/pii/S1526612522001402

[45] R. T. Jacobsen and R. B. Stewart, "Thermodynamic properties of nitrogen including liquid and vapor phases from 63 k to 2000 k with pressures to 10,000 bar," vol. 2, no. 4, pp. 757–922. [Online]. Available: https://doi.org/10.1063/1.3253132

[46] U. Arena, C. B. Langeli, and A. Cammarota, "L-valve behaviour with solids of different size and density," vol. 98, no. 3, pp. 231–240. [Online]. Available: https://www.sciencedirect.com/science/article/pii/S0032591098000588

[47] H. M. Beakawi Al-Hashemi and O. S. Baghabra Al-Amoudi, "A review on the angle of repose of granular materials," *Powder Technology*, vol. 330, pp. 397–417, May 2018. [Online]. Available: https://www.sciencedirect.com/science/article/pii/S0032591018301153

[48] K. A. Kane, B. A. Pint, D. Mitchell, and J. A. Haynes, "Oxidation of ultrahigh temperature ceramics: kinetics, mechanisms, and applications," vol. 41, no. 13, pp. 6130–6150. [Online]. Available: https://www.sciencedirect.com/science/article/pii/S0955221921003939

[49] R. A. Dawe and E. B. Smith, "Viscosities of the inert gases at high temperatures," vol. 52, no. 2, pp. 693–703. [Online]. Available: http://aip.scitation.org/doi/10.1063/1.1673042

[50] C. Y. Wen and Y. H. Yu, "A generalized method for predicting the minimum fluidization velocity," vol. 12, no. 3, pp. 610–612. [Online]. Available: https://onlinelibrary.wiley.com/doi/10.1002/aic.690120343

[51] P. Schimmels, M. Hayes, K. Randhir, J. Petrasch, and J. F. Klausner, "Enhancing the chemical energy flux in a high-temperature tubular counterflow solid fuel synthesis reactor using a bypass," vol. 62, no. 36, pp. 14 671–14 678. [Online]. Available: https://pubs.acs.org/doi/10.1021/acs.iecr.3c01296

[52] W. Huang, D. Korba, K. Randhir, J. Petrasch, J. Klausner, N. AuYeung, and L. Li, "Thermochemical reduction modeling in a high-temperature moving-bed

reactor for energy storage: 1d model," vol. 306, p. 118009. [Online]. Available: https://linkinghub.elsevier.com/retrieve/pii/S0306261921013106

[53] I. M. Mándity, S. B. Ötvös, and F. Fülöp, "Strategic application of residence-time control in continuous-flow reactors," vol. 4, no. 3, pp. 212–223. [Online]. Available: https://onlinelibrary.wiley.com/doi/abs/10.1002/open.201500018

[54] E. Gross, J. H.-C. Liu, F. D. Toste, and G. A. Somorjai, "Control of selectivity in heterogeneous catalysis by tuning nanoparticle properties and reactor residence time," vol. 4, no. 11, pp. 947–952, number: 11 Publisher: Nature Publishing Group. [Online]. Available: https://www.nature.com/articles/nchem.1465

[55] S. Halder and R. Fruehan, "Reduction of iron-oxide-carbon composites: Part II. rates of reduction of composite pellets in a rotary hearth furnace simulator," vol. 39, no. 6, pp. 796–808. [Online]. Available: https://doi.org/10.1007/s11663-008-9203-1

[56] S. Abanades, P. Charvin, and G. Flamant, "Design and simulation of a solar chemical reactor for the thermal reduction of metal oxides: Case study of zinc oxide dissociation," vol. 62, no. 22, pp. 6323–6333. [Online]. Available: https://www.sciencedirect.com/science/article/pii/S0009250907005878

[57] H. P. Bonzel, "A surface diffusion mechanism at high temperature," vol. 21, no. 1, pp. 45–60. [Online]. Available: https://www.sciencedirect.com/science/article/pii/0039602870900622

[58] D. Rupasov, T. Makarenko, and A. J. Jacobson, "Oxygen diffusion in sr3yco4o10.5: An electrical conductivity relaxation and thermogravimetric analysis approach," vol. 265, pp. 68–72. [Online]. Available: https://linkinghub.elsevier.com/retrieve/pii/S0167273814003154

[59] B. T. Na, T. Yang, J. Liu, S. Lee, H. Abernathy, T. Kalapos, and G. Hackett, "Enhanced accuracy of electrochemical kinetic parameters determined by electrical conductivity relaxation," vol. 361, p. 115561. [Online]. Available: https://linkinghub.elsevier.com/retrieve/pii/S016727382100014X

[60] H. L. Weissberg, "Effective diffusion coefficient in porous media," vol. 34, no. 9, pp. 2636–2639. [Online]. Available: http://aip.scitation.org/doi/10.1063/1.1729783

[61] F. Morin, "A mathematical assessment of chemical diffusion measurements in transition metal oxides," vol. 128, no. 11, p. 2439, publisher: IOP Publishing. [Online]. Available: https://iopscience.iop.org/article/10.1149/1.2127267/meta

[62] P. E. Childs and J. B. Wagner Jr, "Chemical diffusion in wustite and chromium-doped manganous oxide in heterogeneous kinetics of elevated temperature," pp. 269–342.

[63] D. Korba, W. Huang, K. Randhir, J. Petrasch, J. Klausner, N. AuYeung, and L. Li, "A continuum model for heat and mass transfer in moving-bed reactors

for thermochemical energy storage," vol. 313, p. 118842. [Online]. Available: https://linkinghub.elsevier.com/retrieve/pii/S030626192200280X

[64] I. Macdonald, M. El-Sayed, K. Mow, and F. Dullien, "Flow through porous media-the ergun equation revisited," *Industrial & Engineering Chemistry Fundamentals*, vol. 18, no. 3, pp. 199–208, 1979.

[65] H.-W. Haering, *Industrial Gases Processing*, 1st ed. John Wiley & Sons, Ltd. [Online]. Available: https://onlinelibrary.wiley.com/doi/10.1002/9783527621248

[66] A. Marcinek, J. Guderian, and D. Bathen, "Performance determination of high-purity n2-PSA-plants," vol. 26, no. 7, pp. 1215–1226. [Online]. Available: https://doi.org/10.1007/s10450-020-00204-9

[67] P. T. Krenzke and J. H. Davidson, "On the efficiency of solar h2 and CO production via the thermochemical cerium oxide redox cycle: The option of inert-swept reduction," vol. 29, no. 2, pp. 1045–1054, publisher: American Chemical Society. [Online]. Available: https://doi.org/10.1021/ef502601f

[68] B. Bulfin, L. Buttsworth, A. Lidor, and A. Steinfeld, "High-purity nitrogen production from air by pressure swing adsorption combined with SrFeO3 redox chemical looping," vol. 421, p. 127734. [Online]. Available: https://www.sciencedirect.com/science/article/pii/S1385894720338547

[69] J. H. Keenan and J. Kaye, "A table of thermodynamic properties of air," vol. 10, no. 3, pp. A123–A130. [Online]. Available: https://doi.org/10.1115/1.4009281

[70] A. Vasić, S. C. Cheng, and D. C. Groeneveld, "A comparison of predictions of high-temperature steam properties," vol. 132, no. 3, pp. 367–379. [Online]. Available: https://www.sciencedirect.com/science/article/pii/002954939290231J

[71] F. G. Keyes, L. B. Smith, and H. T. Gerry, "The specific volume of steam in the saturated and superheated condition together with derived values of the enthalpy, entropy, heat capacity and joule thomson coefficients: Part IV. steam research program," vol. 70, no. 8, pp. 319–364, publisher: American Academy of Arts & Sciences. [Online]. Available: https://www.jstor.org/stable/20023142

[72] J. H. Keenan, "Steam tables : thermodynamic properties of water including vapor, liquid, and solid phases." [Online]. Available: https://cir.nii.ac.jp/crid/1130282270587985280

[73] R. Matz and Z. Zimerman, "Low-temperature vapour compression and multi-effect distillation of seawater. effects of design on operation and economics," vol. 52, no. 2, pp. 201–216. [Online]. Available: https://www.sciencedirect.com/science/article/pii/0011916485850098

[74] L. Liang, D. Han, R. Ma, and T. Peng, "Treatment of high-concentration wastewater using

double-effect mechanical vapor recompression," vol. 314, pp. 139–146. [Online]. Available: https://www.sciencedirect.com/science/article/pii/S0011916413000350

[75] D. Han, Z. Si, and J. Chen, "Analysis of an intermittent mechanical vapor recompression evaporation system," vol. 193, p. 116996. [Online]. Available: https://www.sciencedirect.com/science/article/pii/S1359431121004439

[76] F. E. Becker and A. I. Zakak, "Recovering energy by mechanical vapor recompression," *Chem. Eng. Prog.; (United States)*, no. 81:7, 7 1985. [Online]. Available: https://www.osti.gov/biblio/6412273

[77] B. F. Lachner Jr, G. F. Nellis, and D. T. Reindl, "The commercial feasibility of the use of water vapor as a refrigerant," *International journal of refrigeration*, vol. 30, no. 4, pp. 699–708, 2007.

[78] J. J. Papike, S. B. Simon, and J. C. Laul, "The lunar regolith: Chemistry, mineralogy, and petrology," vol. 20, no. 4, pp. 761–826. [Online]. Available: https://onlinelibrary.wiley.com/doi/abs/10.1029/RG020i004p00761

[79] D. S. Smith, S. Fayette, S. Grandjean, C. Martin, R. Telle, and T. Tonnessen, "Thermal resistance of grain boundaries in alumina ceramics and refractories," vol. 86, no. 1, pp. 105–111. [Online]. Available: https://onlinelibrary.wiley.com/doi/abs/10.1111/j.1151-2916.2003.tb03285.x

[80] B. Hao, G. Sun, J. Zhang, X. Li, F. Xu, and K. Liu, "Heat transfer mechanism and performance optimization scheme of refractory oxide solid heat storage materials." [Online]. Available: https://papers.ssrn.com/abstract=4561769